POLITECNICO
MILANO 1863

SCUOLA DI INGEGNERIA
INDUSTRIALE
E DELL'INFORMAZIONE

Laser cleaning of rhodium-coated mirrors from fusion-relevant boron and boron-tungsten contaminants

Tesi di Laurea Magistrale in
Nuclear Engineering - Ingegneria Nucleare

Author: **Roberta Micheli**

Student ID: 250799
Advisor: Prof. Alessandro Maffini
Co-advisors: Dott. Davide Orecchia
Academic Year: 2024-2025

Abstract

Magnetic confinement nuclear fusion energy represents a promising long-term solution for the production of clean electricity for future generations. In future tokamaks such as ITER and DEMO, optical diagnostic systems will be fundamental for acquiring information about the plasma. First Mirrors, which are the diagnostic components placed in the vacuum vessel facing the plasma, will therefore be subjected to extreme conditions, undergoing erosion and the redeposition of contaminants originating from the first wall materials. Following the recent revision of the ITER project, which now foresees a first wall entirely made of tungsten (W) and the use of boronization as a first wall conditioning technique, boron (B) and tungsten (W) are expected to be the main materials composing the redeposits on the mirrors.

This thesis work aimed to produce, on a laboratory scale, rhodium (Rh) mirror samples covered with boron and mixed boron-tungsten coatings, evaluating their impact on the reflectivity of the mirrors. Furthermore, the efficacy of the laser cleaning technique, aimed at restoring the original optical properties of the mirrors, was evaluated. The nanocrystalline rhodium samples and the contaminant layers were produced via Pulsed Laser Deposition (PLD). Morphology, atomic composition, and reflectance of the samples were evaluated using Scanning Electron Microscopy (SEM), EDXS spectroscopy, and spectrophotometry, respectively. The laser cleaning tests were carried out with the same laser used for the production of the samples. The cleaning results with two different wavelengths were compared: infrared (IR, 1064 nm) and green (532 nm).

The results of the optical analyses show that the presence of contaminants drastically modifies the optical properties of rhodium: the boron coatings exhibit a dielectric behavior characterized by interference fringes. Conversely, the presence of tungsten gives a more absorbing metallic behavior to the film, which suppresses the interference pattern. Regarding the boron deposits, the use of the green wavelength was extremely effective, ensuring a specular reflectivity recovery in the visible and near-infrared (vis-NIR) range up to 90%. The IR wavelength, on the other hand, led to worse results, leaving film residues on the sample. The cleaning of the mixed B/W film proved to be more complex with both wavelengths. The metallic behavior of the film hinders ablation, favoring

instead the melting of the film and the consequent heat transfer, causing damage to the underlying mirror. In this case, the use of the infrared wavelength yielded better results compared to the green one.

In conclusion, the study highlights how the presence of redeposits reduces the intrinsic damage threshold of the mirror. To optimize future *in-situ* operations in the reactors, cleaning cycles on thin deposits (less than 100 nm) are proposed, in order to maximize the laser cleaning efficiency and preserve the structural integrity of the mirror.

Keywords: Nuclear fusion, ITER, First Mirrors, Laser Cleaning, Pulsed Laser Deposition (PLD), Boron, Tungsten.

Abstract in lingua italiana

L'energia da fusione nucleare a confinamento magnetico rappresenta una soluzione a lungo termine promettente per la produzione di energia elettrica pulita per le future generazioni. Nei futuri tokamak come ITER e DEMO, i sistemi di diagnostica ottica saranno fondamentali per l'acquisizione di informazioni sul plasma. I primi specchi, ovvero i componenti diagnostici che saranno posti nella camera a vuoto affacciati sul plasma, saranno per questo sottoposti a condizioni estreme, subendo l'erosione e la rideposizione di contaminanti provenienti dai materiali della prima parete. A seguito della recente revisione del progetto di ITER, che ora prevede una prima parete interamente in tungsteno (W) e l'impiego della boronizzazione come tecnica di condizionamento della prima parete, ci si aspetta che il boro (B) e il tungsteno (W) costituiranno i materiali principali dei rideposiiti sugli specchi.

Questo lavoro di tesi si pone l'obiettivo di produrre su scala di laboratorio dei campioni di specchi di rodio (Rh) coperti da rivestimenti di boro e misti di boro-tungsteno, valutando il loro impatto sulla riflettività degli specchi. Inoltre, è stata valutata l'efficacia della tecnica di pulizia tramite laser finalizzata al ripristino delle proprietà ottiche originarie degli specchi. I campioni in rodio nanocristallino e gli strati di contaminanti sono stati prodotti mediante deposizione laser pulsata (PLD). La morfologia, la composizione atomica e la riflettanza dei campioni sono state valutate rispettivamente tramite microscopia elettronica a scansione (SEM), spettroscopia EDXS e spettrofotometria. Le prove di pulizia laser sono state effettuate con lo stesso laser impiegato per la produzione dei campioni. Sono stati confrontati i risultati della pulizia con due diverse lunghezze d'onda: infrarossa (IR, 1064 nm) e verde (532 nm).

I risultati delle analisi ottiche mostrano che la presenza dei contaminanti modifica drasticamente le proprietà ottiche del rodio: i rivestimenti di boro presentano un comportamento dielettrico caratterizzato da frange di interferenza. Al contrario, la presenza di tungsteno dà al film un comportamento metallico più assorbente, che sopprime il pattern di interferenza. Per quanto riguarda i depositi di boro, l'utilizzo della lunghezza d'onda verde è stato estremamente efficace, garantendo un recupero della riflettività speculare nel range visibile e vicino infrarosso (vis-NIR) fino al 90%. La lunghezza d'onda IR ha

invece portato a risultati peggiori, lasciando residui di film sul campione. La pulizia dei composti misti B/W si è dimostrata più complessa con entrambe le lunghezze d'onda. Il comportamento metallico del film rende difficile l'ablazione, favorendo invece la fusione del film e il conseguente trasferimento di calore, causando danni allo specchio sottostante. In questo caso l'impiego della lunghezza d'onda nell'infrarosso ha dato migliori risultati rispetto a quella nel verde.

In conclusione, lo studio evidenzia come la presenza di ridepositi riduca la soglia di danno intrinseca dello specchio. Per ottimizzare le future operazioni *in-situ* nei reattori, si propongono cicli di pulizia su depositi sottili (inferiori a 100 nm), al fine di massimizzare la resa della pulizia laser e preservare l'integrità strutturale dello specchio.

Parole chiave: Fusione nucleare, ITER, Primi Specchi, Pulizia laser, Deposizione Laser Pulsata (PLD), Boro, Tungsteno.

Contents

1 | Introduction to magnetic confinement fusion

1.1. Global electricity production

The improvement of living conditions for the global population as a whole requires large amounts of energy. For this reason, it is desirable that global energy demand continues to increase, as it has for decades [1] and is expected to do in the coming years. This scenario is shown in Figure 1.1, where global electricity production over the last 40 years is broken down by source.

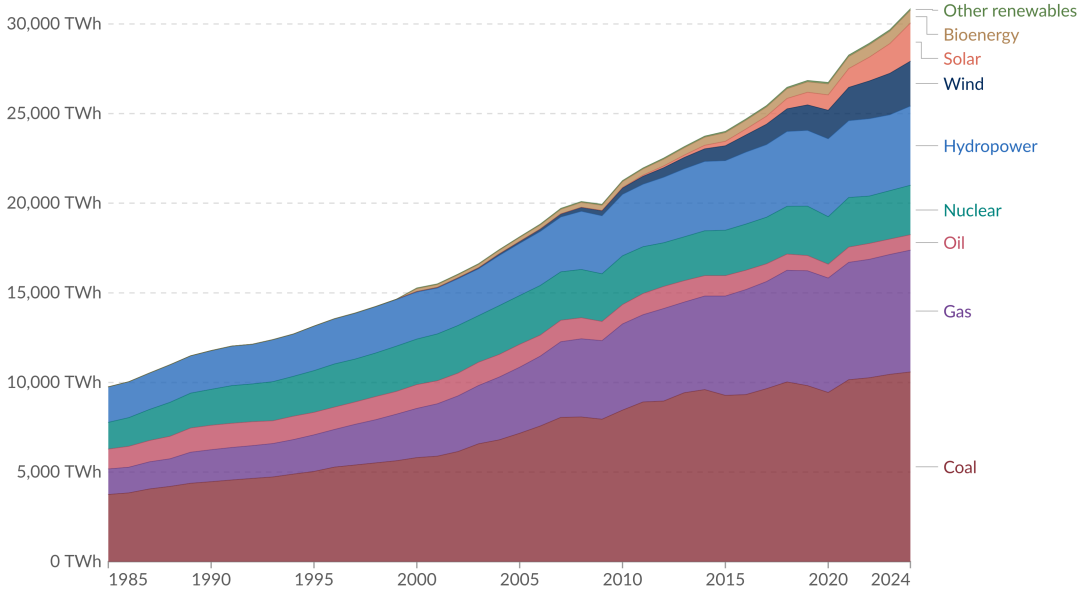

Figure 1.1: Global electricity production by source from 1985 to 2024, measured in terawatt-hours. One TWh corresponds to 3.6×10^{15} J. "Other renewables" include geothermal, wave and tidal [2].

In particular, the most recent Global Energy Review [3] published by the International Energy Agency (IEA) states that in 2024 global electricity demand increased by 4.3% and

the absolute increase was the largest ever observed, excluding the years following periods of global crisis and recession.

Another important point is that fossil fuels have always been, and still are, the primary source used to generate the majority of the world's electricity. Moreover, fossil fuels represent an even higher fraction of the energy mix if overall energy production is considered, including, for example, industry and the transport sector.
In 2024, 59% of global electricity was produced from fossil fuels, despite the fact that the cause-and-effect relationship between greenhouse gas emissions and global warming has been well established for years [4]. Furthermore, the consequences that this will have on our planet and on the most vulnerable populations, for instance in terms of sea-level rise, droughts, and desertification, are also well known [5].

One of the greatest and most challenging issues humanity faces in this century is producing increasing amounts of energy while minimizing the impact of such production on global warming by reducing greenhouse gas emissions. For this reason, it is of crucial importance that electricity generation shifts toward low emission energy souces, such as renewable energy sources and nuclear energy as well.

As can be seen in Figure 1.1, renewable energy sources have experienced significant growth in recent years, and the fraction of electricity generated from them has been steadily increasing. However, they present some drawbacks, such as intermittency due to weather conditions and inability to adjust power output on demand. This variability requires large scale energy storage capacity to manage peak power production, as well as a stable backup generation capacity to supply electricity during periods when renewable energy production is unable to meet demand [6].

Since the decarbonization of the electricity sector, and even more so of the whole energy sector, is an extremely ambitious goal, it is not possible to reach this objective with renewables alone. Instead, they need to be developed in parallel with other low-emission energy sources that can compensate for their major drawbacks. In this context, nuclear energy represents a clean, reliable, and sustainable solution that can continuously produce electricity following fluctuations in demand, without emitting greenhouse gases into the atmosphere.

Nowadays, electricity production in nuclear power plants is based on the fission of heavy nuclei, a technology characterized by a high fuel energy density and, as a consequence, low waste generation [7]. However, interest in nuclear fusion research is strong, as it represents a promising long-term solution with an energy density even higher than that of fission and with no generation of long-lived radioactive waste. Furthermore, the fuels required for this

process are easily accessible and widely distributed across the globe, offering independence from the geopolitical constraints associated with the supply of fuel for conventional fission reactors. Additionally, the technology is intrinsically safe by design: the reaction requires extremely specific conditions to occur, meaning that the fusion process would immediately stop in case of a system failure, preventing severe accidents. Thus, the development of this technology up to commercial distribution would provide a limitless, low-emission base-load energy supply, capable of sustainably satisfying the increasing global energy demand for future generations, in a complementary manner with renewable sources.

1.2. Nuclear reactions

The term *nuclide* was introduced by Truman P. Kohman in 1947 [8] to define a species of atom characterized by the constitution of its nucleus. The number of protons Z is called the *atomic number*, as it uniquely identifies the atomic species, while the number of neutrons is N. The sum of these two quantities defines the *mass number* $\mathrm{A} = \mathrm{Z} + \mathrm{N}$, which represents the total number of nucleons within the nucleus. However, the rest mass of a nucleus is lower than the sum of the masses of its constituents by an amount proportional to the *binding energy* ε_b of the nucleus itself. This quantity is known as the *mass defect* and increases with the strength of the strong nuclear force binding the nucleons together:

$$m_{nucleus} = Z m_{proton} + N m_{neutron} - \frac{|\varepsilon_b|}{c^2} \tag{1.1}$$

A general reaction between two nuclear species can be written as:

$$A + B \rightarrow C + D \tag{1.2}$$

The left-hand side represents the entrance channel, constituted by the two reactants, and the right-hand side represents the exit channel, constituted by the products of the reaction. Associated with this process is a quantity known as the *Q-value*, which is defined as the difference between the rest masses in the entrance channel and those in the exit channel. As a consequence of energy conservation, this quantity is also equal to the difference between the final and initial kinetic energies, or, equivalently, to the difference between the initial and final binding energies[1] of the species involved in the reaction:

$$Q \equiv (m_A + m_B)c^2 - (m_C + m_D)c^2 = K_f - K_i = |\varepsilon_b|_f - |\varepsilon_b|_i \tag{1.3}$$

[1]The binding energy is conventionally a negative quantity; thus, it is common practice to refer to it by its absolute value. The reason is that it is more intuitive to associate a higher value of binding energy with a more tightly bound nucleus.

If the Q-value is greater than zero the reaction is *exothermic*. It means that the products are more tightly bound than the reactants, and this excess energy is released as an increase in the kinetic energy of the products with respect to the reactants. This is the energy that can be exploited to produce electricity.

Figure 1.2 shows the absolute value of the binding energy per nucleon as a function of the mass number. It can be observed that the region of most stable nuclides is around A $\approx$ 60. Thus, exothermic reactions consist of either the nuclear fission of heavy nuclei such as ^{235}U and ^{239}Pu, which releases an average of 0.8 MeV per nucleon, or the nuclear fusion of light nuclei. One of the primary reasons why the latter is so attractive is that the energy released per single fusion event can reach 5–6 MeV per nucleon.

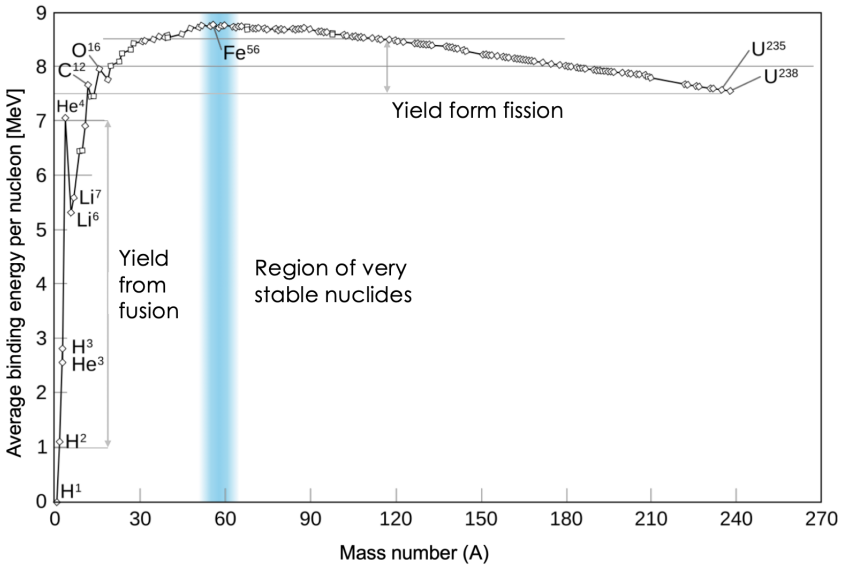

Figure 1.2: Absolute value of the binding energy per nucleon as a function of the mass number. Adapted from [9].

1.3. Nuclear fusion

Nuclear fusion reactions have been occurring in stars for billions of years and are responsible for the enormous amount of energy that makes them shine. The simplest of these reactions is the fusion of two protons, which is at the basis of the so called proton-proton chain reaction:

$$^{1}\mathrm{H} + {}^{1}\mathrm{H} \rightarrow \mathrm{D} + \mathrm{e}^{+} + \nu_e \tag{1.4}$$

$$^{1}\mathrm{H} + \mathrm{D} \rightarrow {}^{3}\mathrm{He} + \gamma \tag{1.5}$$

$$^{3}\mathrm{He} + {}^{3}\mathrm{He} \rightarrow {}^{4}\mathrm{He} + 2\,{}^{1}\mathrm{H} \tag{1.6}$$

The net result is the conversion of four protons into an α particle, two positrons and two neutrinos, with an energy release of 26.2 MeV [10]. However, the first of these reactions is mediated by the weak interaction, requiring the β-decay of a proton into a neutron. This process is highly improbable, making the timescale of the reaction extremely long. Thus, other fusion reactions have to be considered for energy production on Earth.

While no perfect reaction exists that is entirely free of drawbacks or engineering challenges, two key factors guide the selection of the most promising candidates: first, hydrogen (Z=1) nuclides are attractive reactants because the Coulomb barrier, which is the repulsive force between nuclei that must be overcome for the reaction to occur, is minimized, as hydrogen nuclei contain only a single proton.
Deuterium (D), consisting of one neutron and one proton, is a stable hydrogen isotope and naturally occurs with an isotopic abundance of 0.0156% [11]; as a consequence, it is easily obtainable and presents no supply chain issues. In contrast, Tritium (T) is the heaviest hydrogen isotope and is composed of two neutrons and one proton; since it is unstable and undergoes β^- decay, it necessitates artificial production to be used.
The second factor to be considered is the fact that, as illustrated in Figure 1.2, the ^{4}He nucleus exhibits high stability due to its *doubly magic*[2] nature [12]. The high binding energy of the α particle maximizes the Q-value of reactions that have this nucleus in the output channel, making such reactions particularly attractive. Some of the reactions that are currently of interest are:

$$\mathrm{D} + \mathrm{T} \rightarrow {}^4\mathrm{He} + \mathrm{n} \qquad Q = 17.6 \text{ MeV} \tag{1.7}$$

$$\mathrm{D} + {}^3\mathrm{He} \rightarrow {}^4\mathrm{He} + {}^1\mathrm{H} \qquad Q = 18.3 \text{ MeV} \tag{1.8}$$

$$\mathrm{D} + \mathrm{D} \rightarrow {}^3\mathrm{He} + \mathrm{n} \qquad Q = 3.27 \text{ MeV} \tag{1.9}$$

$$\mathrm{D} + \mathrm{D} \rightarrow \mathrm{T} + {}^1\mathrm{H} \qquad Q = 4.03 \text{ MeV} \tag{1.10}$$

$${}^1\mathrm{H} + {}^{11}\mathrm{B} \rightarrow 3\,{}^4\mathrm{He} \qquad Q = 8.7 \text{ MeV} \tag{1.11}$$

To evaluate the advantages and disadvantages of these reactions, specific parameters are introduced:

The *cross section* $\sigma(v)$ represents the probability of a reaction event per pair of nuclei and is a function of their relative velocity $v = |\vec{v}_1 - \vec{v}_2|$. Figure 1.3 shows the cross-sections of the previously introduced processes as a function of center-of-mass kinetic energy. The shape of these curves is characterized by an exponential decrease at low energies, as

[2] In nuclear physics, a *magic number* refers to a specific number of protons or neutrons (such as 2, 8, or 20) that completely fill a nuclear shell, providing greater stability. A doubly magic nucleus, like ^{4}He (2 protons and 2 neutrons), has magic numbers for both types of nucleons, making it exceptionally stable.

quantum tunneling is required for fusion to occur when the kinetic energy is lower than the Coulomb repulsion potential. It can be noted that the D-T reaction has the advantage of showing a higher cross section compared to other reactions; moreover, the cross section reaches its maximum value at a relatively low center-of-mass kinetic energy.

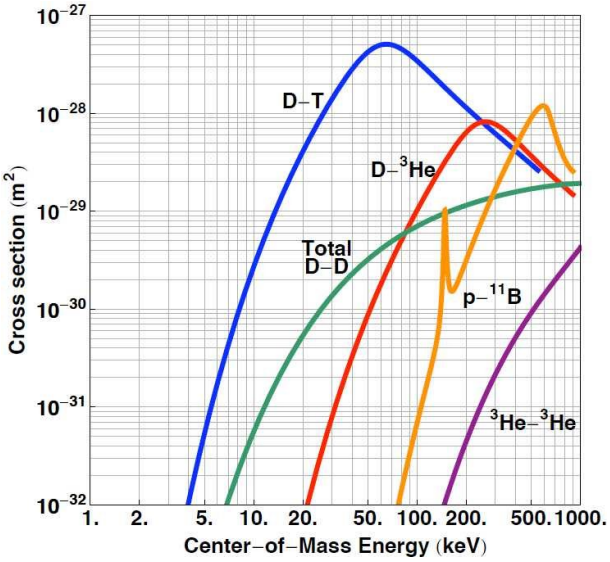

Figure 1.3: Fusion cross sections for various reactions versus center-of-mass kinetic energy [13].

The reaction frequency per pair of nuclei is obtained by averaging the cross section over the velocity distribution functions of the reacting species. This parameter is called *reactivity* and it is important because it provides a measure of the ease of occurrence of fusion reactions:

$$\langle \sigma v \rangle = \iint \sigma(v) v f_1(\vec{v}_1) f_2(\vec{v}_2)\, d^3v_1 d^3v_2 \tag{1.12}$$

While Equation 1.12 represents the general definition, in thermonuclear fusion the two interacting populations (characterized by number densities n_1 and n_2) are typically considered to be at thermal equilibrium. As a consequence, their corresponding particle velocity distribution functions, $f_1(v_1)$ and $f_2(v_2)$, are Maxwellian.
Therefore, the number of reactions per unit time and unit volume between the two populations and the corresponding power density associated with the fusion process can be computed as:

$$R = n_1 n_2 \langle \sigma v \rangle \tag{1.13}$$

$$P = n_1 n_2 \langle \sigma v \rangle Q \tag{1.14}$$

The reactivity of various fusion reactions is plotted in Figure 1.4 as a function of the temperature T of the Maxwellian distribution. The temperature is expressed in energy units because, in a system in thermal equilibrium, the temperature of an ideal gas is related to the mean kinetic energy of its constituents through the Boltzmann constant, $k_b = 1.38 \times 10^{-23}$ J/K, according to the relation $\varepsilon_k = \frac{3}{2} k_b T$.

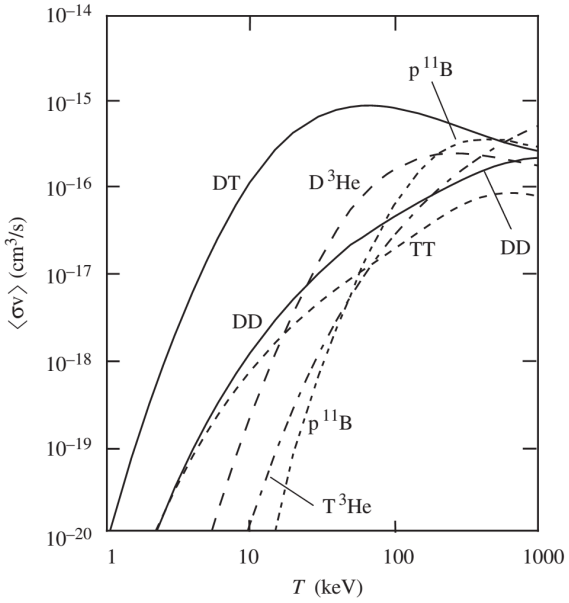

Figure 1.4: Reactivity of fusion reactions averaged over a Maxwell-Boltzmann distribution as a function of temperature [14].

D-D reactions (Eqs. 1.9 and 1.10) are interesting because they rely on a single reactant: a non-radioactive and far more easily obtainable hydrogen isotope compared to tritium. Nevertheless, both the cross section and the reactivity associated with these processes have low values, making them less attractive compared to other reactions.
The D-^{3}He (eq. 1.8) reaction has the advantage of an alpha particle in the exit channel, leading to a very high Q-value. Furthermore, it does not produce neutrons, thus limiting neutron irradiation damage to plant materials. Even in this case, however, the cross section and the reactivity do not have values high enough to justify the enormous engineering effort that would be required to produce all the ^{3}He needed, since this nuclide is extremely rare and expensive (isotopic abundance 0.00013% [11]).
Interest in the p-^{11}B (eq. 1.11) reaction is due to the fact that the reagents are stable, abundant, and easily accessible. Moreover, the reaction is aneutronic and in the exit channel there are only three alpha particles. Again, the main problem is that the reactivity reaches useful values only at extremely high energies, greater than 100 keV.

Currently, scientific interest is primarily focused on extracting energy by exploiting the

fusion reaction between deuterium and tritium (eq. 1.7). The reason is that this reaction exhibits the highest cross section and reactivity values, which are achieved at significantly lower temperatures compared to those required by other reactions to obtain the same result. As shown in Figure 1.4, at a temperature of 10 keV, the reactivity of the D-T reaction exceeds that of the D-D reaction by two orders of magnitude, thus leading to a much higher reaction rate (eq. 1.13). Furthermore, the Q-value of 17.6 MeV is among the highest, due to the fact that the reactants are hydrogen isotopes and the exit channel contains an alpha particle.
However, also this reaction presents several engineering challenges. The energy gain from a single reaction appears as the kinetic energy of the products. Since this is a two body process, the energy of each product is uniquely determined by momentum conservation, which distributes the Q-value between the products in inverse proportion to their masses: the alpha particle carries 3.5 MeV and the neutron 14.1 MeV. Such high-energy neutrons cause neutron irradiation damage and can induce activation in the structural materials of the plant.
As previously mentioned, another issue is tritium availability, which can be addressed by breeding it within the plant employing part of the neutrons generated by the fusion reaction itself. The reactions that can be exploited for this purpose are those involving neutron capture by lithium:

$$\mathrm{n} + {}^{6}\mathrm{Li} \rightarrow {}^{4}\mathrm{He} + \mathrm{T} \qquad Q = 4.8 \text{ MeV} \tag{1.15}$$

$$\mathrm{n} + {}^{7}\mathrm{Li} \rightarrow {}^{4}\mathrm{He} + \mathrm{T} \qquad Q = -2.5 \text{ MeV} \tag{1.16}$$

The first reaction is exothermic and is favored for thermal neutrons, while the second is endothermic and is more likely to occur with fast neutrons. By using a fraction of the neutrons originating from the D-T reaction for this purpose, it is possible in principle to establish a self-sustaining cycle, effectively making lithium, rather than tritium, the primary fuel together with deuterium. A schematic of a hypothetical nuclear fusion power plant based on these concepts is presented in Figure 1.5.

Such a plant represents a big engineering challenge because, to reach energies of the order of tens of keV, required for a sufficiently high reaction rate, thermal energy must be supplied to the reacting nuclides to reach temperatures of the order of hundreds of millions of Kelvin. At these temperatures, matter is in the *plasma* state: electrons are separated from nuclei and form distinct populations of charged particles, which interact collectively through long range Coulomb interactions and are subject to electromagnetic forces. When density and temperature conditions are such that nuclei overcome the

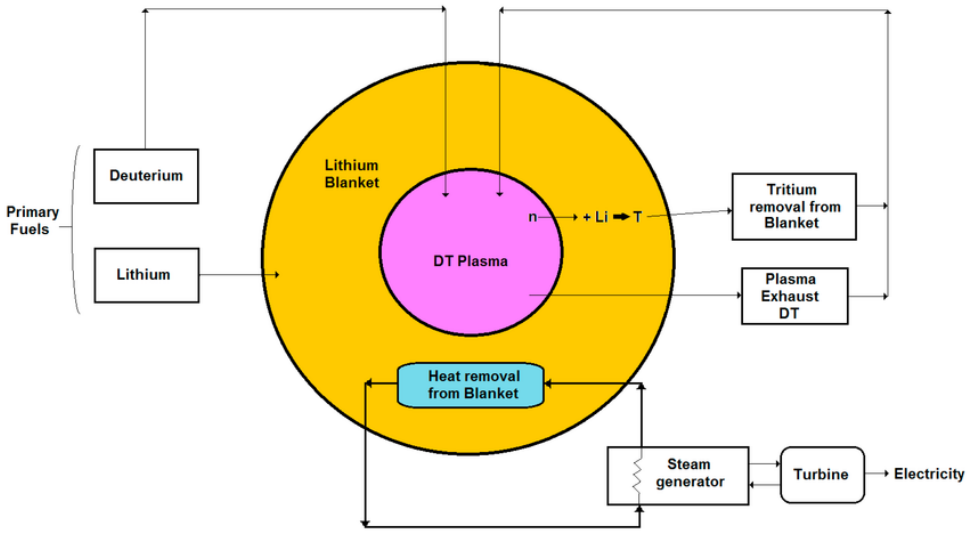

Figure 1.5: Schematic of a D-T based nuclear power plant [15].

electrostatic repulsion and fuse together with a macroscopically significant collision rate, the plasma is considered *thermonuclear*. The goal of a fusion power plant is to maintain the plasma in thermonuclear conditions for the time required to obtain a net energy gain and, subsequently, to convert this energy into electricity efficiently.

1.4. Energy balance and ignition

A plasma in a steady-state condition must satisfy a power balance that follows from conservation of internal energy density:

$$S_\alpha + S_{ext} = S_r + S_q \tag{1.17}$$

The terms on the left-hand side represent the power density inputs for the plasma: S_α is the source originating from the fusion reaction. Indeed, the alpha particles generated by fusion, carrying $E_\alpha = 3.5$ MeV of kinetic energy, are charged particles that interact with the plasma, depositing their energy to heat the plasma itself. Considering a D-T plasma in which the two populations are characterized by equal number density ($n_D = n_T = n/2$), under the assumption of quasi neutrality condition, for which the electron density equals the total ion density ($n_e = n_D + n_T = n$, and assuming thermal equilibrium between electrons and ions ($T_e = T_i = T$); the plasma pressure p and temperature T are related by $p = 2nT$ according to the kinetic definition of temperature [16]. Under these conditions,

S_α can be rewritten as:

$$S_\alpha = \frac{n^2}{4}\langle\sigma v\rangle E_\alpha = K_\alpha \frac{\langle\sigma v\rangle}{T^2} p^2 \tag{1.18}$$

where $K_\alpha = 1.37$, p is in bar, T in keV and the reactivity is in units of 10^{-22} $\frac{\mathrm{m}^3}{\mathrm{s}}$. In contrast, the neutron is assumed to leave the plasma because it is an uncharged particle. Thus, its 14.1 MeV of kinetic energy can be exploited to extract energy from the plasma, as it is deposited into the blanket in the form of heat following neutron thermalization. Based on this process, a conventional heat exchanger and steam generator are assumed to be placed outside the blanket to generate electricity (Figure 1.5).
S_{ext} is the term representing all external energy sources required to keep the plasma in thermonuclear conditions, including Neutral Beam Injection (NBI) and radio frequency heating, such as Electron or Ion Cyclotron Resonance Heating (ECRH and ICRH) [17].

The right-hand side of Eq. 1.17 contains the power loss terms: S_r includes the power density lost by emission of electromagnetic radiation, primarily due to the Bremsstrahlung effect [18]. These losses are directly proportional to the square of the plasma effective atomic number Z_{eff}, meaning that the presence of high atomic number impurities in the plasma accelerates its cooling. This dependence must be taken into account during the choice of plasma facing materials, giving preference to low Z elements. S_r can be expressed, considering only Bremsstrahlung losses, in terms of pressure and temperature as:

$$S_r = S_B = C_B Z_{\text{eff}}^2 n^2 T^{1/2} = K_B \frac{p^2}{T^{3/2}} \tag{1.19}$$

where $C_B = 5.34$ W m^3 keV$^{-1/2}$ is a constant [19] and $K_B = 0.0053$.
The last term S_q represents the thermal energy loss due to conduction. By defining the energy confinement time τ_E as the characteristic timescale for thermal energy to diffuse out of the system, S_q can be expressed in terms of plasma parameters as:

$$S_q = \frac{3nT}{2\tau_E} = K_q \frac{p}{\tau_E} \tag{1.20}$$

where $K_q = 0.15$.

A self-sustained reaction is achieved when the power deposited into the plasma by fusion alpha particles is sufficient to compensate for all energy losses. This condition is known as *ignition* and, starting from the energy balance in Eq. 1.17, it is derived as:

$$K_\alpha \frac{\langle\sigma v\rangle}{T^2} p^2 \geq K_B \frac{p^2}{T^{3/2}} + K_q \frac{p}{\tau_E} \tag{1.21}$$

It can be also be expressed as a condition for $p\tau_E = nT\tau_E$, known as the *triple product*, or equivalently for $n\tau_E$ called *Lawson parameter*, as a function of temperature:

$$p\tau_E \geq \frac{K_q T^2}{K_\alpha \langle \sigma v \rangle - K_B T^{1/2}} \tag{1.22}$$

This constitute the so called *Lawson criterion* [20]. Thus, for a given temperature and specific reaction, ignition can only be achieved if $p\tau_E$ exceeds a certain threshold determined by Eq. 1.22. The plot of the minimum triple product required for ignition as a function of temperature is shown in Figure 1.6. Consequently, to identify the most favorable condition for satisfying the $p\tau_E$ requirement, it is necessary to find the temperature that minimizes the lower limit required for ignition. This value is approximately $T_{\min} \approx 15$ KeV, which is equivalent to 150 million Kelvin. The corresponding values for the triple product and Lawson parameter are:

$$(p\tau_E)_{\min} \approx 8.3\,\mathrm{atm\,s} \tag{1.23}$$

$$(n\tau_E)_{\min} \approx 2 \times 10^{14}\,\mathrm{s\,cm^{-3}} \tag{1.24}$$

A further reason why the D-T reaction is of primary interest is that it exhibits the lowest triple product required for ignition compared to any other reaction. Furthermore, the temperature at which this minimum occurs is lower for this reaction than for others (Figure 1.6b).

If external power input is considered ($S_{ext} \neq 0$), the conditions for achieving ignition become more favorable. Consequently, the minimum required Lawson parameter decreases. Moreover, in a realistic scenario, the thermonuclear plasma operates as an energy amplifier with a gain expressed as the ratio between the fusion power density (S_f) and the externally supplied power density:

$$Q = \frac{S_f}{S_{ext}} \tag{1.25}$$

The equilibrium condition where the fusion power density fully compensates the input power is called *break-even* and corresponds to $Q = 1$. To achieve a net energy gain, $Q > 1$ is required, while the ignition condition represents the ideal case where $Q \to \infty$. An increasing external power input corresponds to a lower value of Q and, as illustrated in Figure 1.6a, this lower Q leads to a reduction in the minimum required Lawson parameter to achieve it, compared to the ignition condition.

Considering the nuclear fusion power plant as a whole, the net energy gain obtained by the conversion of external electric power P_{in} into a new and higher electric power output

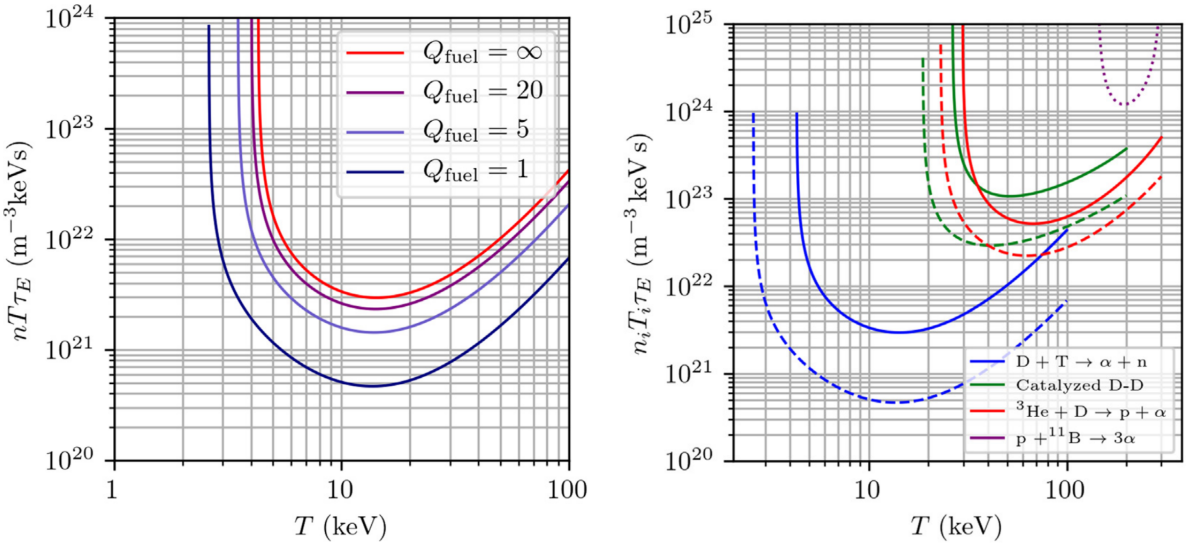

Figure 1.6: Minimum triple product as a function of temperature. Focusing (a) on D-T reaction to achieve different values of Q. Considering (b) different reactions to achieve $Q = \infty$ (solid lines), $Q = 1$ (dashed lines), and $Q = 0.5$ (dotted line, p-^{11}B only) [19].

P_{out} is expressed by the engineering Q:

$$Q_{eng} = \frac{P_{out} - P_{in}}{P_{in}} \tag{1.26}$$

This factor is related to the previously introduced Q (Eq. 1.25) by several intrinsic process efficiencies, such as the efficiency with which the input electric power is converted into useful power for the plasma and, subsequently, the fraction of that power that the plasma can actually absorb. Furthermore, the efficiency of the output thermodynamic cycle must be considered [19]. Nowadays, the goal for future fusion plants is to reach Q_{eng} values around 5–10.

1.5. Plasma confinement

To maintain the plasma in thermonuclear conditions, confinement is necessary to prevent its expansion driven by thermal energy, which would lead to energy dissipation. In stars, plasma confinement is provided by the gravitational field generated by their enormous mass. However, replicating such gravitational confinement on Earth is not feasible, as it would require astrophysical masses; therefore, fusion research relies on alternative approaches.

Since the Lawson criterion imposes a condition on the product of two quantities, $n\tau_E$, it can be satisfied either by short energy confinement times and high densities or, conversely, by long energy confinement times and low densities.
The former approach forms the basis of **Inertial Confinement Fusion** (ICF) research [21]. In this context, it is possible to achieve very high particle densities, exceeding 10^{24} cm^{-3}, by compressing a solid D-T pellet using extremely intense laser beams to deliver a sufficient amount of energy uniformly onto the target. The finite inertia of the particles prevents matter and energy from disassembling instantaneously, providing confinement for a duration τ_E on the order of nanoseconds. In April 2025, the National Ignition Facility (NIF) in the USA achieved a record value of $Q = 4.13$ with this approach [22].
On the other hand, the **Magnetic Confinement Fusion** (MCF) [23] approach has as a goal energy confinement time on the order of seconds, thus operating with very dilute plasma with densities on the order of 10^{14} cm^{-3}. In this case, confinement exploits the fact that, being composed of charged particles, the plasma interacts with electric and magnetic fields which, if properly applied from the outside, can be utilized to constrain the plasma within a specific spatial region.

Numerous experiments based on both MCF and ICF are presented in Figure 1.7, where the progress towards higher Q and higher plasma temperatures is shown. While both approaches represent major scientific achievements, MCF is currently considered the most promising candidate for the development of commercial power plants. The primary advantage of MCF lies in its potential for almost steady-state and continuous operation, which is highly desirable for electricity generation. In contrast, ICF requires a high repetition rate of micro-explosions that induce significant engineering challenges regarding continuous heat extraction and high-speed target injection. Furthermore, despite the larger energy gain Q achieved by ICF facilities, the overall efficiency of the driving lasers remains extremely low, making the goal of a fusion plant with $Q_{\text{eng}} > 1$ difficult to realize.

Since this thesis is situated within the framework of Magnetic Confinement Fusion research, the following sections will provide a more detailed description of the physics basis of this approach and of the most promising configuration investigated to exploit this technology in the future: the *tokamak*.

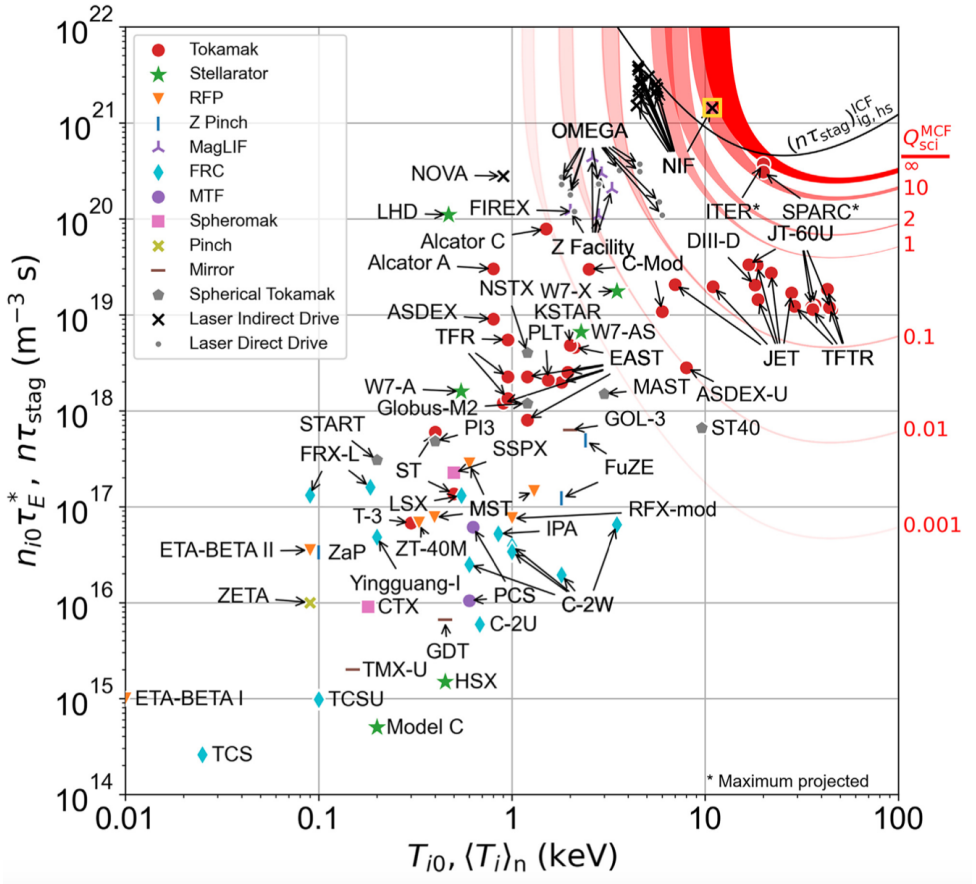

Figure 1.7: Experimentally inferred Lawson parameters of fusion experiments vs ion temperature. The red contours correspond to the Lawson parameters and ion temperatures required to achieve the indicated values of gain for MCF. The finite widths represent a range of assumed impurity levels. The black curve corresponds to the Lawson parameters and ion temperatures required to achieve ignition for ICF [24].

1.5.1. Magnetic confinement

A charged particle with mass m and charge q moving with velocity $\mathbf{v}$ in an uniform and constant magnetic field $\mathbf{B}$ is subjected to the magnetic part of the Lorentz force:

$$\mathbf{F} = \frac{q}{c}\mathbf{v} \times \mathbf{B} \tag{1.27}$$

According to guiding-center theory [25], the particle follows a helical path, known as *gyromotion*, winding around the magnetic field lines with characteristic cyclotron frequency Ω and Larmor radius ρ_L:

$$\Omega = \frac{qB}{mc} \qquad \rho_L = \frac{v_\perp}{|\Omega|} \tag{1.28}$$

where $v_\perp$ is the component of particle velocity perpendicular to the magnetic field. Thus, by applying an external uniform magnetic field, the plasma can be confined in the directions transverse to the field lines. However, particles remain free to move in the axial direction of the field itself as shown in Figure 1.8.

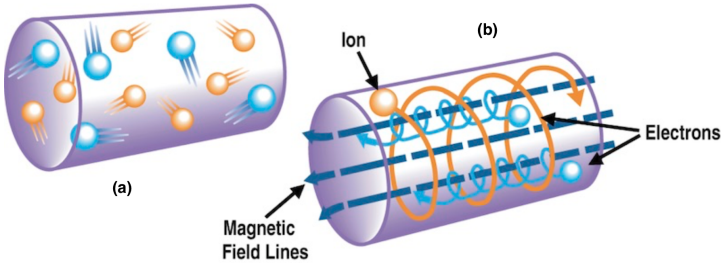

Figure 1.8: Particle motion (a) without external field and (b) in an uniform magnetic field [26].

Historically, longitudinal confinement in machines with cylindrical symmetry was investigated by exploiting the *magnetic mirror effect*. Indeed, the conservation of energy and of the magnetic dipole moment induces the reversal of the direction of motion of a particle moving from a region of lower magnetic field intensity to a region where the field lines are denser, causing the particle to be reflected, provided that the difference between the two intensities is sufficiently large. Based on this effect, linear mirror machines [27] were constructed by increasing the magnetic field intensity at the ends, as shown in Figure 1.9. However, due to high losses and instabilities, they proved to be unsuitable for fusion purposes.

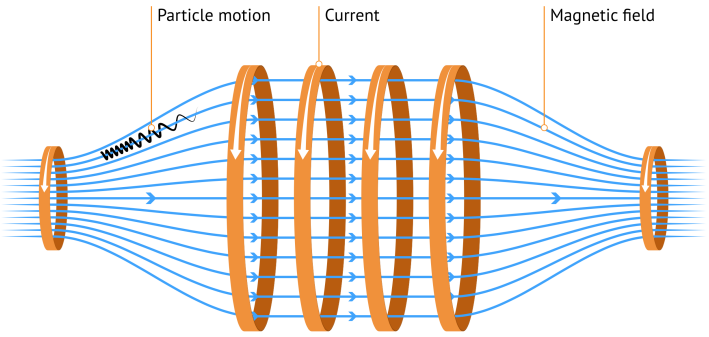

Figure 1.9: Linear mirror machine configuration [28].

Another possibility is to close the magnetic field lines upon themselves, thus moving from a cylindrical to a toroidal geometry, creating circular field lines that constitute the *toroidal* magnetic field (B_T). In this configuration, however, the spatial uniformity of the field lines is lost, as they become denser in the inner region of the torus. This condition

introduces drifts to the particle cyclotron motion: the curvature drift moves particles vertically towards the outer regions. Moreover, the $\nabla \mathbf{B}$ drift causes a vertical separation of charges with opposite signs, thus creating an electric field $\mathbf{E}$ that generates an $\mathbf{E} \times \mathbf{B}$ drift, which drives the particles radially outward from the torus. Overall, the plasma tends to expand, and not even a single particle could be confined solely with a toroidal magnetic field. For this reason, a *poloidal* magnetic field (B_P) must be added. This magnetic field component consists of field lines that form closed loops in any section orthogonal to the toroidal direction, known as poloidal sections. The superposition of toroidal and poloidal fields creates the helical magnetic field lines shown in Figure 1.10, through which magnetic confinement can be achieved.

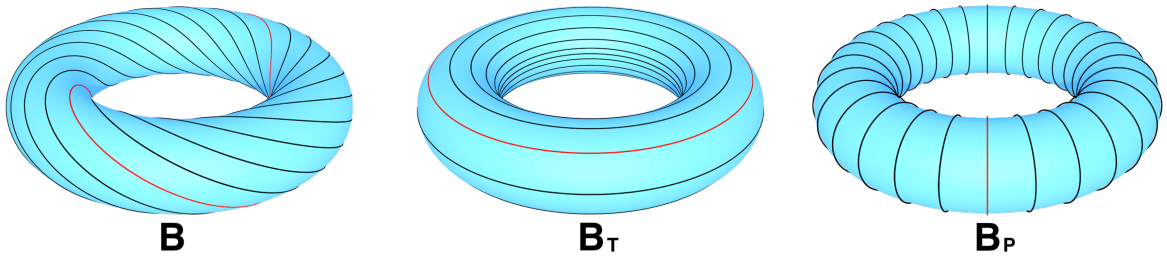

Figure 1.10: Helical field lines as a composition of toroidal and poloidal magnetic field lines, adapted from [29].

The required magnetic field configuration in toroidal systems can be achieved in two ways, both proposed in the early 50s. The poloidal component can be generated by driving a high toroidal current through the plasma itself, which acts as an excellent electrical conductor. Machines operating on this principle are called *tokamaks*; the name is a Russian acronym standing for "toroidal chamber with magnetic coils", as this concept was first proposed by the Russian physicists Sakharov and Tamm [30].
The second method to obtain the desired field line shape is to generate them entirely from the outside using coils with extremely complex shapes, thus breaking the toroidal symmetry. This concept was first developed in the USA by Spitzer [31] and forms the basis of the machine known as the *stellarator*. A comparison of the basic elements and shapes of these two machines is presented in Figure 1.11.

1.6. Tokamak configuration

At present, the majority of toroidal machines operating worldwide are tokamaks, as this design is considered the most promising technology for achieving future fusion goals. This preference is primarily due to their simpler, axisymmetric magnetic geometry, which makes them significantly easier to engineer and construct compared to stellarators.

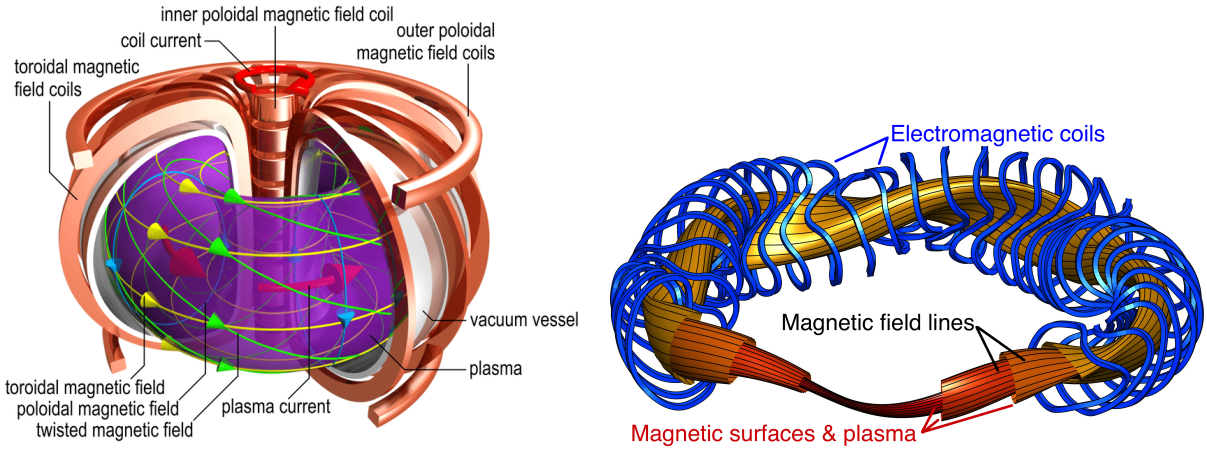

(a) (b)

Figure 1.11: Schematic of (a) Tokamak and (b) Stellarator machine.

Tokamaks are designed to confine the plasma inside a vacuum chamber characterized by toroidal symmetry, meaning that all poloidal sections of the chamber are equivalent.

The toroidal field is generated by induction via a current flowing through poloidal coils. The required toroidal field intensity can reach up to 11.8 T [32], implying that the necessary electric current intensity is enormous, on the order of several mega-amperes. To generate such currents, superconducting coils are therefore required; these must be cooled with liquid helium to temperatures of a few Kelvin to prevent excessive losses due to the Joule effect. The spatial proximity of such a cold region to the extremely hot thermonuclear plasma within the vacuum chamber requires enormous thermal insulation and constitutes, therefore, a major engineering challenge in tokamak design.

In this configuration, the poloidal magnetic field is generated by a toroidal current flowing through the plasma. This current is induced externally following a transformer principle: the vacuum chamber is magnetically coupled with a transformer primary winding, that is a central solenoid through which a current flows. Consequently, the plasma acts as the secondary circuit of the transformer, and a toroidal current is induced within it. This operating principle renders the plasma current intrinsically pulsed, representing one of the main drawbacks of a tokamak, since continuous energy production requires a steady-state condition rather than a pulsed one.
Another reason why the toroidal current in the plasma is beneficial is that it can be exploited to heat the plasma via the Joule effect. This heating mechanism is called *ohmic heating*, and the energy it can transfer is proportional to the plasma resistivity. Since resistivity scales as $T^{-\frac{3}{2}}$ [33], the hotter the plasma becomes, the more it behaves as an ideal conductor. For this reason, ohmic heating is effective primarily during the initial

heating phases.

An important parameter that indicates the relative intensity of poloidal and toroidal fields is the *safety factor* q:

$$q = \frac{aB_{\mathrm{T}}}{RB_{\mathrm{P}}} \tag{1.29}$$

where a and R are the minor radius (radius of the poloidal cross-section) and the major radius of the torus, respectively.
A purely toroidal field configuration represents a stable equilibrium, whereas a purely poloidal field corresponds to an unstable one, meaning that any small perturbation from equilibrium is amplified. However, as previously stated, the poloidal field is indispensable for confinement, which would be impossible with a toroidal field alone. Consequently, the condition $B_{\mathrm{P}} \ll B_{\mathrm{T}}$ is required to ensure the stability of the plasma equilibrium. Furthermore, since $a \ll R$ by design, a fundamental characteristic of the tokamak is a safety factor q on the order of unity.

The limitation on the poloidal field intensity due to stability criteria translates into an upper limit on the toroidal current flowing in the plasma, and consequently, into a maximum limit on the heat that can be delivered to the plasma via the Joule effect associated with this current. For this reason, additional plasma heating mechanisms are employed. The most important methods, which were already mentioned in Section 1.4, are the following:

- **Neutral Beam Injection (NBI)** involves the injection of neutral atoms of the same species as the plasma with sufficiently high kinetic energy. Through a charge exchange reaction, a high-energy neutral atom colliding with a plasma ion can transfer its electron to the ion. In this way, the high-energy atom becomes a high-energy ion that is confined within the plasma, while the less energetic ion becomes a neutral atom that leaves the plasma.
- **Radiofrequency Heating** is based on the collisionless absorption of electromagnetic waves propagating in the plasma. The most relevant absorption frequencies correspond to the characteristic cyclotron frequencies of the species composing the plasma, allowing the exploitation of resonance in systems such as Electron Cyclotron Resonance Heating (ECRH) and Ion Cyclotron Resonance Heating (ICRH).

1.6.1. First Wall and Plasma Facing Components

One of the most critical components of the tokamak is the inner surface of the vacuum chamber, as it directly faces the plasma. This is the so-called *First Wall* (FW), and it consists of *Plasma Facing Components* (PFC). The selection of materials for these

components is crucial, as they must maintain structural integrity under harsh conditions. These include extremely high temperatures and high particle fluxes, primarily high-energy neutrons, but also charged particles escaping confinement and electromagnetic radiation. The consequences of such conditions and the materials selected for the first wall to address these challenges will be discussed in detail in Chapter 2.

The most important Plasma Facing Components are those designed to delimit the *plasma core*, which is confined within closed magnetic field lines, from the region characterized by open magnetic field lines. The objective is to localize the Plasma-Wall Interaction (PWI) onto these specific components. The outermost closed magnetic field line delimiting the plasma core is known as the *Last Closed Flux Surface* (LCFS). The region between the LCFS and the first wall is called the *Scrape-Off Layer* (SOL), which is characterized by open magnetic field lines. If a particle crosses the LCFS, it enters the SOL and will inevitably encounter a PFC, such as the limiter or the divertor [34] shown in Figure 1.12.

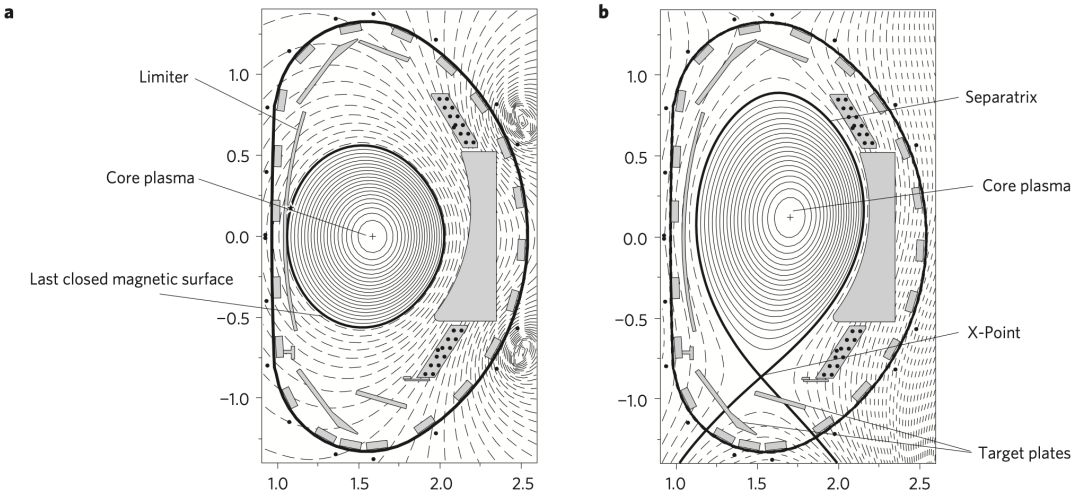

Figure 1.12: Different ways to shape plasma boundary. In the limiter configuration (a) the plasma touches the wall, while in the divertor configuration (b) the target plates recieve charged particles and heat excaping from the core plasma [35].

The limiter is a component that protrudes into the vacuum chamber and contacts the plasma directly, thereby geometrically defining the plasma boundary. The open field lines of the Scrape-Off Layer intersect the limiter, depositing charged particles and heat onto it. While this is the simplest method to manage the plasma boundary, it suffers from a major drawback: a significant contamination of the plasma by impurities resulting from the intense interaction with the limiter itself.
To address this issue, a higher-performance configuration was developed: the divertor. In

this case, the magnetic field lines are shaped such that the LCFS exhibits an X-point, characterized by a poloidal field $B_P = 0$. In this configuration, the LCFS is also referred to as the *separatrix*, as it separates the plasma core from the SOL. Furthermore, the Scrape-Off Layer assumes a specific shape that channels the heat and charged particle loads onto specific strike points located on the divertor targets, which are specifically designed to withstand these high loads. The primary advantage of this configuration is that the plasma core remains significantly less contaminated compared to the limiter configuration.

1.7. ITER and DEMO

"ITER was founded under the auspices of the IAEA[3] as a project of peaceful cooperation: seven members, more than 30 nations, uniting to achieve one of the most complex ambitions of humankind" [36]. The words of Pietro Barabaschi, ITER Director-General, encapsulate the ambition, expectations, and spirit of cooperation, even among politically distant nations such as China, the USA and the Russian Federation, that drive this project.

ITER (International Thermonuclear Experimental Reactor) is the world's largest tokamak experiment, currently under construction in Cadarache, southern France. The *Start of Research Operations* (SRO), including the first plasma discharge with hydrogen and deuterium, is scheduled for 2034, while the first discharge with D-T plasma is currently scheduled for 2039 [37], as shown in the operational plan in Figure 1.13.

ITER will operate as an experimental machine and will not produce electricity for the grid; its main goal is the operability of a fully integrated fusion engineering system for the demonstration of nuclear fusion as a viable energy source for mankind. According to the ITER Research Plan [38], the specific goals are:

- Generation of 500 MW of thermal fusion power with a gain of $Q \geq 10$.
- Sustainment of high-gain pulses for a duration between 300 and 500 seconds.
- Demonstration of long-pulse and non inductive steady-state scenarios with $Q \geq 5$, for durations of 1000 s and 3000 s, respectively.
- Implementation of a testing program for *Test Blanket Modules* (TBM) to demonstrate the tritium breeding capability necessary for fuel autonomy in future reactors, although ITER will not be equipped with a full lithium blanket or a closed fuel cycle.

[3]International Atomic Energy Agency

- Collection of key reference data to perform safety-related evaluations for D–T operations regarding radiation maps, tritium retention and removal, dust production, with subsequent validation of nuclear safety assumptions.

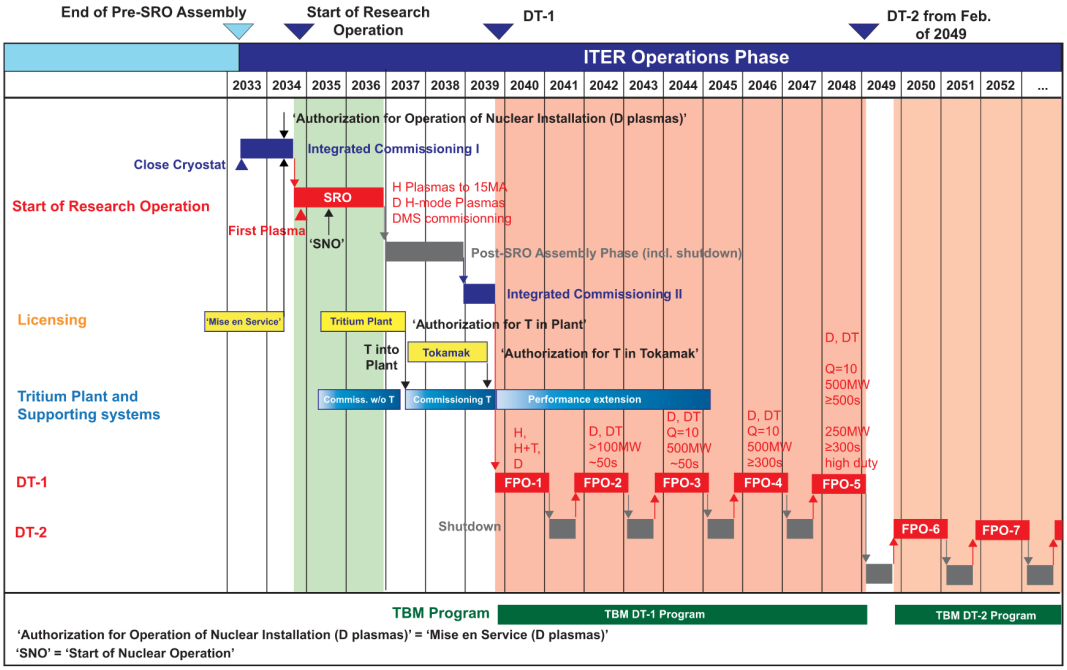

Figure 1.13: Operational plan for the execution of the new baseline ITER research plan [38].

The experiments that will be performed in ITER will be of primary importance for addressing physics, design, and operational issues in support of future demonstration reactors such as DEMO (Demonstration Power Plant). According to the *European Research Roadmap to the Realisation of Fusion Energy* [39], DEMO will be the step between ITER and a future commercial power plant. Its construction is expected to begin in the 2040s, with the aim of delivering fusion electricity in the second half of the century. The design phase is already in progress having as goals:

- Net electricity production of 300–500 MW power output to the grid.
- Self-sufficiency in fusion fuel via tritium production.
- Demonstration of safety and environmental sustainability, and sufficient technology maturity to allow a first commercial power plant to be constructed.

2 | Tokamak First Wall materials

2.1. Plasma-Wall Interaction

The selection of materials for the First Wall and Plasma Facing Components is a complex task, as these components must withstand extreme conditions for months or years of operation with minimal maintenance, without compromising plasma performance. For this reason, the physics governing Plasma-Wall Interaction (PWI) and its consequences is of primary interest.

First wall materials must sustain electromagnetic radiation and particle fluxes originating from the plasma, including charged particles escaping magnetic confinement and runaway electrons, but especially high-energy neutrons. In ITER, during normal operation, these fluxes are expected to be on the order of 10^{19} particles/m^{2}s [34] on the main wall, with energies of hundreds of eV. Furthermore, fluxes on the divertor are expected to reach 10^{24} particles/m^{2}s [40], with lower energies on the order of a few eV in the detachment[1] regime. However, during transient events like *Edge Localized Modes* (ELMs) and disruptions, particle fluxes can reach even higher levels.

The consequences for PFCs are numerous, and all must be carefully considered.
Very high **thermal loads** can have several damaging effects. They can cause material melting, but also cracking; since the working principle of a tokamak is intrinsically pulsed, based on startup and shutdown cycles, the resulting heating and cooling cycles induce thermal fatigue, which can lead to structural cracking. To address these challenges, tungsten has proven to be the most suitable material, being capable of withstanding thousands of thermal load cycles at 10 MW/m^2 and hundreds of cycles at 20 MW/m^2 [41]. Its failure mechanism under high thermal loads has been shown to be primarily due to *macro-cracking* and *self-castellation* [40].
Radiation damage is primarily caused by neutrons, as they are capable of inducing atomic modifications within the crystal lattice of metals by displacing atoms from their

[1] Detachment is a regime in which low Z impurities, such as argon and neon, are injected in the SOL to significantly reduce the energy of the particles impinging on the divertor. Operating in this regime is crucial to prevent the divertor from erosion and melting.

equilibrium positions. This process triggers a collision cascade, leading to the formation of vacancies and interstitials. Furthermore, the high energy of fusion neutrons can induce (n, α) reactions within the target materials. This phenomenon is the source of helium production inside the metal, which, over the long term, causes material swelling. The fact that the neutron energy in this context is 14.1 MeV makes these consequences significantly more severe compared to standard fission reactions, where the mean neutron energy is approximately 2 MeV.
Another consequence of neutron irradiation is **material activation**, which results in the production of radioactive isotopes. To address this issue, it is necessary to select materials that, upon irradiation, yield radionuclides with sufficiently short half-lives, on the order of hundreds of years. These materials are referred to as *Low Activation Materials* (LAM) [42].
If particles impinge on the wall with sufficiently high energy, they can be retained through a phenomenon called ion implantation. This issue is particularly critical regarding tritium, whose supply challenges have already been mentioned, since **tritium retention** removes fuel ions that are indispensable for the economy of the fusion reaction. For this reason, it is essential to select first wall materials that minimize this phenomenon.
Another issue to be taken into consideration is the **erosion** of the first layers of PFCs, which can be of both chemical and physical origin. Chemical erosion mainly concerns elements with high affinity with hydrogen, such as carbon [43], with which hydrogen forms volatile compounds, eroding the material itself. Materials that do not tend to form hydrogen compounds are subject to erosion as well, due to physical sputtering.

2.1.1. Physical sputtering

Physical sputtering is the phenomenon that causes the erosion of materials after the interaction with energetic ions. The basic principle that governs it is the fact that when an ion impinges on a solid target it can transfer its momentum to the atoms of the surface and, if the transferred energy is sufficiently high, the atom can be ejected from the surface. It is a threshold process because the energy needed to sputter the atom from the material needs to be higher than the binding energy of the atom itself.

The ratio of the number of sputtered atoms to the number of impinging ions per unit surface and unit time is the *sputtering yield*, the fundamental parameter to quantify material erosion. A complete theory to predict sputtering yield is still missing due to the high complexity of the phenomenon. However, there exists a formula for sputtering yield based on the theory of elastic scattering developed by Yamamura in 1996 [44], which is still valid for low energy of impinging ions, under the assumption of fresh material and

without considering the ion impinging angle.

The most important characteristics of sputtering yield emerging from this theory are useful to understand the efficiency of the process. In particular, the yield depends on the masses of both the impinging ion and of the target atom: if the masses are similar the energy transfer in an elastic collision is maximized, meaning that the yield is higher if the masses of the projectile and the target are comparable. Moreover, because energy transfer is more efficient in this condition, the threshold energy required for the impinging ion to cause sputtering is lower when masses are similar.
Thus, in a tokamak, where the majority of ions are hydrogen nuclides, low Z materials are subjected to a higher erosion rate due to the sputtering process than heavier materials.

The twofold consequence of sputtering on tokamak operation is, on one side, the already mentioned erosion of FW materials, on the other the contamination of the plasma with impurities that have a negative impact on its performance. Indeed, the plasma emits bremsstrahlung radiation, which is an undesirable phenomenon from an energetic point of view because it increases plasma cooling. Bremsstrahlung emission scales as the square of the effective atomic number of the plasma (Eq. 1.19), meaning that impurities entering the plasma from erosion are all detrimental, but high Z impurities have a much greater impact on acceleration of plasma cooling than low Z impurities. Figure 2.1 shows the radiative cooling loss coefficient, which is the radiated power normalized over the densities, as a function of the temperature for different species, highlighting the impact of high Z atoms.

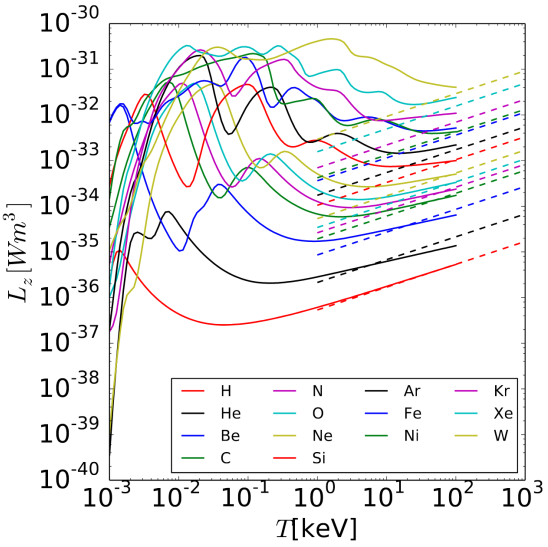

Figure 2.1: Radiative loss coefficient for different species. The higher lines are associated to heavier elements [45].

Impurities inside the plasma can also be redeposited in a location different from the original one, thus creating layers of undesired species on First Wall components, affecting their performance. This is the case of First Mirrors (FM) needed for optical diagnostics, for which a cleaning procedure to remove redeposits is essential, as will be discussed in detail in Chapter 3.
Several numerical simulations have been performed to evaluate erosion and deposition on FW materials, in particular with the 3D Monte-Carlo impurity transport code ERO2.0 [46]. The erosion-deposition maps shown in Figure 2.2 are the result of one of those simulations regarding tungsten in DEMO; it can be noted that there are areas more subjected to erosion and, conversely, others in which deposition is predominant.

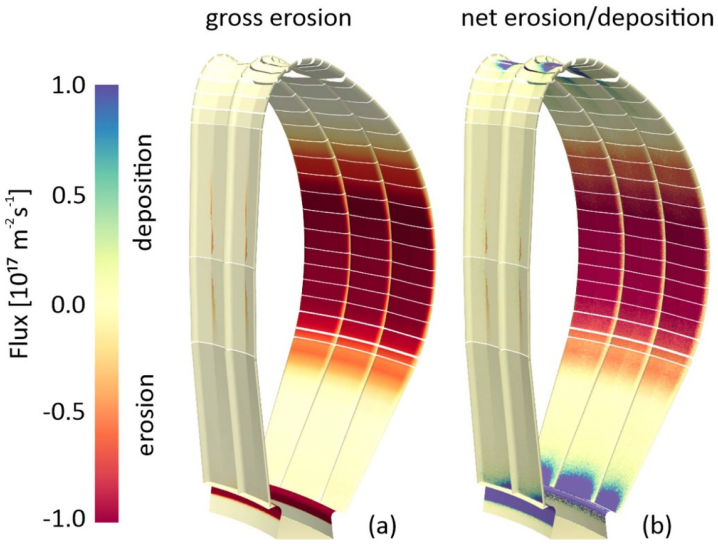

Figure 2.2: ERO2.0 simulation results for W gross erosion map (a) and W net erosion-deposition map (b) shown for one toroidal DEMO sector [47].

2.2. ITER's First Wall materials

Because of the variety and the complexity of problems that need to be faced in the framework of PWI, the choice on FW and PFC materials has undergone changes over the last 20 years, before reaching the one that is currently considered the best solution for ITER.

Tungsten has some favorable properties that have always made it one of the most promising materials for this purpose. However, it also has some drawbacks that necessitate coupling W with other materials to achieve optimal tokamak performance with minimum maintenance:

- It exhibits a low sputtering yield and a high sputtering threshold energy; moreover, it does not suffer chemical erosion from the DT plasma, thus erosion is minimized compared to other materials. Nevertheless, even if the amount of impurities in the plasma is low, their impact on bremsstrahlung losses is significant due to the fact that W is an high-Z atom.
- Tritium inventory is expected to be small due to its low chemical affinity with hydrogen.
- It has the highest melting point of all metals (3695 K), allowing for the resistance to high thermal loads, as already mentioned in Section 2.1.

In the first studies on the divertor [48] a **Carbon** Fibre Composite (CFC) armour was planned for high heat flux components, namely the strike points. CFC showed good thermal shock and thermal fatigue resistance with a low crack propagation; moreover, the neutron-induced swelling resistance was good as well. Figure 2.3a shows a schematic of such a divertor with carbon components.
However, the high tritium retention caused by the co-deposition of carbon with hydrogen isotopes was prohibitive for sustaining ITER operation and the chemical erosion rate was significant. Thus, in 2013 [49] a full tungsten divertor for ITER was approved, and the first cassette bodies are now expected to be delivered in early 2026 [50].

Beryllium has been a candidate material for the inner vessel wall as oxygen impurities getter. Indeed, its affinity for oxygen helps to remove it from the chamber, thereby obtaining good vacuum conditions to facilitate the plasma start-up. Furthermore, since it is a low-Z element, its impurities in the plasma are more tolerable from an energetic point of view. Tritium retention is also better for Be than for carbon.
From 2011 to 2016 three campaigns were conducted at the JET (Joint European Torus) tokamak at the Culham Centre for Fusion Energy in the United Kingdom, with the aim of testing the performance of the so-called ITER-like wall (ILW), which in those years consisted in a Be first wall and a W divertor [51]. These campaings were necessary to understand the behaviour of such a wall during its interaction with the plasma, in preparation for D–T operation and in support to ITER [52]. Figure 2.3b shows the JET-ILW configuration used for all three campaigns: ILW1, 2011-2012; ILW2, 2013-2014; and ILW3 2015-2016.

However, during these experiments some important drawbacks of Be and their consequences were better understood. In particular Be exhibits a high sputtering rate, thus needing frequent maintenance for the replacement of a significant number of eroded panels. This requirement conflits with the high toxicity of beryllium, which limits the accessibility

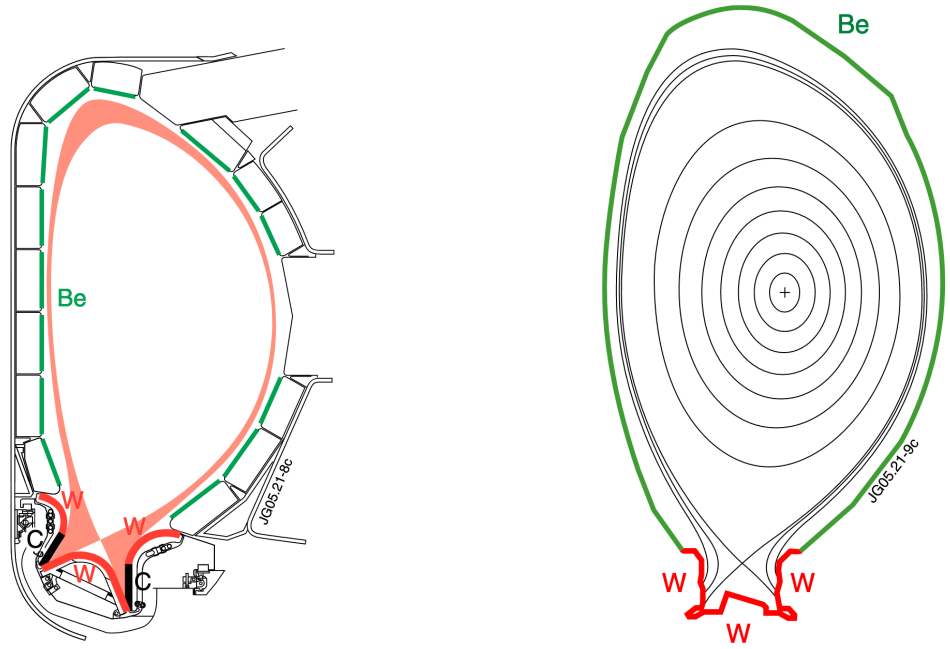

(a) (b)

Figure 2.3: Initial ITER material choices considering (a) CFC on strike points and (b) a full tungsten divertor [53].

to the first wall for workers during installation and repair operations. Furthermore, the melting temperature of Be is low (1560 K), and so is its resistance to thermal loads; as a result, Be melting and melt layer displacement could modify the induced current paths in the first wall, leading to mechanical failure of the panels in single events [54].

This, together with an improved understanding of the implications of the use of W as first wall material for plasma operation and performance, led to the decision to finally remove Be from the first wall and adopt a full tungsten wall [38]. This decision was proposed by the ITER Project in 2023 with a *New Baseline* [37] aiming to better allign with the fusion community's roadmap to fusion energy; indeed, all future fusion devices designed for a burning plasma plan to use tungsten as armour material [55].

With the transition from beryllium to a tungsten first wall, the risk of plasma radiative cooling by high-Z impurities becomes a critical concern. To address this, layers of **boron** will be deposited on the FW primarily to act as a powerful oxygen getter. By drastically reducing the oxygen content in the vacuum chamber, a role previously performed by beryllium, boron suppresses the oxygen-driven sputtering of tungsten, while its layer secondarily serves as a temporary low-Z physical barrier against direct erosion.

2.2.1. Boronization

Boronization is a plasma-enhanced Chemical Vapour Deposition (CVD) technique that will be employed in ITER to cover the first wall with a thin layer of boron, typically in the range 50-100 nm [54].

This wall conditioning technique was previously used and studied in other fusion devices, starting with the TEXTOR (Tokamak Experiment for Technology Oriented Research) tokamak in Germany [56].

The working principle of a glow discharge boronization system is based on the injection of a boron-containing gas, typically Helium mixed with diborane molecules B_2H_6. Anodes placed in the vacuum vessel initiate a plasma glow discharge that ionizes the gas molecules so that they are attracted to the wall, which acts as the cathode, thus forming an amorphous thin film of boron.

To add the boronization system to the new baseline of ITER, the *Glow Discharge System* has been modified, and a new set of gas lines to inject diborane has been introduced into the ITER design, as well as a system to destroy the diborane that does not decompose in the plasma; this system is needed due to the high toxicity of diborane [37].
The symmetry of the distribution of anodes and gas injection locations is essential to ensure the most homogeneous coverage of the entire first wall: The symmetry of the glow discharge plasma electrodes and the distribution of diborane gas injection lines are shown in Figure 2.4.

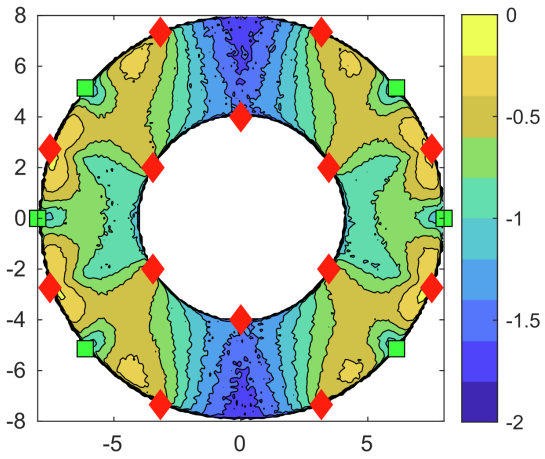

Figure 2.4: Spatial distribution of diborane reactions in the equatorial midplane for a 88 % He and 12 % H_2 carrier gas mixture at 0.3 Pa glow pressure. The colormap is in log scale normalized to the maximum reaction density. The symmetry of gas injection points (green) and anodes (red) is appreciable [57].

As previously mentioned, boron is essential as an oxygen getter, and its role is crucial in the plasma start-up phase to ensure good vacuum conditions characterized by low oxygen content. Moreover, boron is a low-Z element, which guarantees that physical sputtering and erosion of such a layer are less problematic than sputtering of tungsten from the point of view of plasma cooling.

The erosion rate of the boron thin film is high on strongly plasma wetted areas, but its lifetime can reach hundreds of plasma discharges on the less exposed areas, ensuring a sufficiently low level of oxygen content [54]. However, the high sputtering rate of boron remains an issue from the point of view of tritium retention, because the eroded atoms tend to co-deposit with tritium, forming dust that migrates and accumulates mainly in the divertor area, as shown in Figure 2.5.

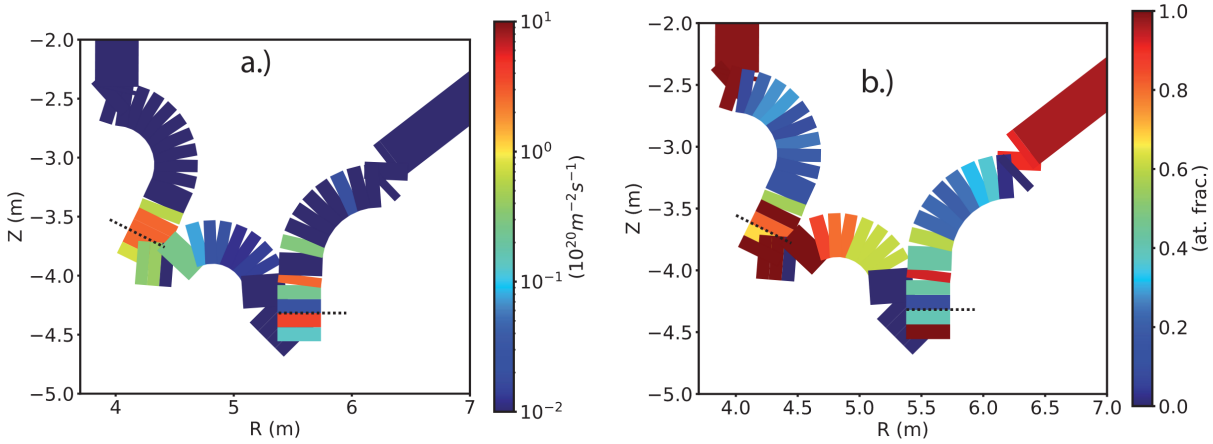

Figure 2.5: Equilibrium B deposition rates (a) and surface concentrations (b) in the divertor due to erosion from an infinite B source in the main chamber. The black dashed lines indicate the approximate strike line positions [58].

3 | First Mirrors for optical diagnostics

3.1. ITER diagnostics

The fact that ITER will be an experimental reactor means that a wide set of diagnostic instrumentation is needed to retrieve important plasma parameters, whose measurement and analysis are crucial to control plasma performance during operation and to obtain important information on plasma behavior to further understand the physics underlying all the processes that will happen in the vacuum chamber.

The variety of parameters that need to be measured requires about 60 individual instruments, divided into the following categories: magnetic diagnostics, neutron diagnostics, optical systems, bolometric systems, spectroscopic systems, microwave diagnostics, plasma-facing and operational diagnostics [59]. These systems are designed to be mounted around the entire vacuum vessel with access to it through *port plug assemblies*, which are primarily a boundary to protect the instrumentation from the harsh conditions present in the chamber; otherwise, it would be damaged and the measurements would not be precise. Figure 3.1 shows the distribution of diagnostic instruments around the vacuum chamber, with the corresponding port plug assemblies.

Among them, optical diagnostics are systems that retrieve information on plasma parameters from the light emitted by the plasma itself, in the spectral range from infrared to ultraviolet, depending on the specific instrument. In order to guarantee the proper functionality of such instruments, they need to be placed outside a bioshield that reduces neutron and gamma irradiation from the main chamber down to doses that are compatible with correct measurements. Thus, the light coming from the vacuum chamber is brought to optical diagnostics instruments via a labyrinthic optical path consisting of mirrors and windows, similar to the one showed in Figure 3.2.

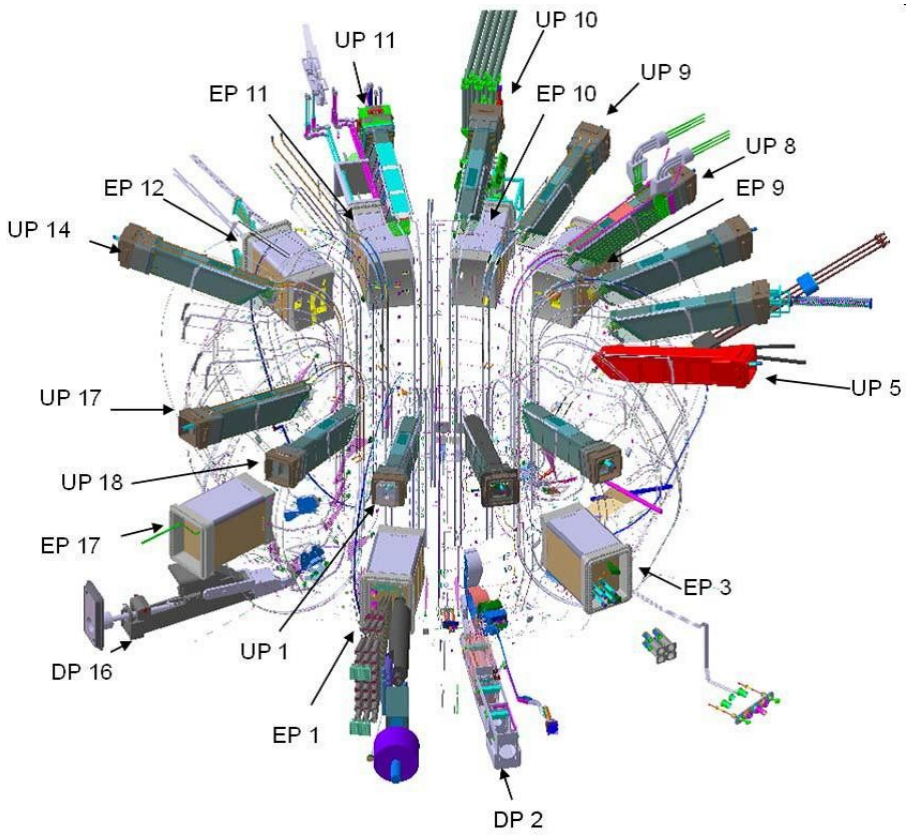

Figure 3.1: Spatial distribution of vacuum chamber access ports for diagnostics in ITER. UP stands for Upper Port, EP for Equatorial Port and DP for Divertor Port [60].

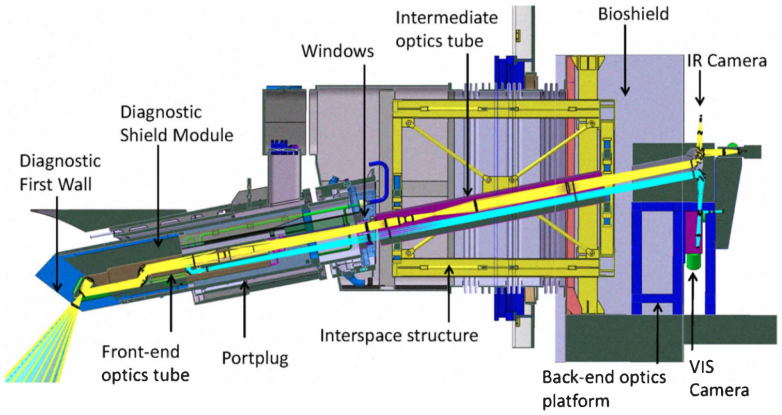

Figure 3.2: Mirror-based optical labyrinth relaying light from inside the machine to outside the bioshield to be collected by the camera systems [61].

The diagnostic first wall is constituted by *First Mirrors* (FM), which are the ones that directly face the plasma; thus, they are subjected to all the consequences presented in Chapter 2 that can degrade their performance. Indeed, particle fluxes on FMs are expected to reach 10^{18} particles/m^{2}s [62], causing both erosion of the mirror and deposition

of impurities from the plasma. In particular, redeposition is expected to dominate erosion and represents a major issue because layers of undesired materials significantly affect the reflectivity of the mirror. For this reason, rather than frequently replacing the contaminated components, implementing an *in-situ* mirror cleaning technique represents a more feasible approach to guarantee the correct measurement of plasma-emitted light during numerous plasma discharges.

3.2. First Mirrors

The choice of materials for first mirrors is guided by the requirement of maintaining optimal optical performances despite the critical conditions to which they are exposed. In particular, the characteristic that a FM material should satisfy are:

- **Specular reflectivity**: The total reflectivity of a surface is given by the sum of the specular and the diffuse one. For FMs a high specular reflectivity is required in the UV-VIS-NIR spectral range and, correspondingly, a low diffuse reflectivity in the same range to avoid loss of information. Furthermore, the specular reflectivity must remain high even at high temperatures and under thermal cycles, to guarantee the suitability of the mirror design for the demanding operational conditions. [62].
- **Sputtering resistance**: a low erosion rate induced by particle fluxes is needed to prolong the life of the mirror as much as possible. Erosion is also preferred to be uniform, because non-uniform erosion would increase the mirror surface roughness, with consequent increase of the diffuse reflectance [63]. The relation that expresses the specular reflectivity R_{spec} of a material as a function of the root-mean-square surface roughness R_{rms} and the wave incident light λ is given by the Bennett's formula [64]:

$$R_{\text{spec}} = R_0 \exp\left[-\left(\frac{4\pi R_{\text{rms}}}{\lambda}\right)^2\right] \tag{3.1}$$

  where R_0 is the reflectivity of the same material with an ideally smooth surface.
- **Thermal resistance**: A high melting temperature is required for proper functioning in an environment with high temperatures; moreover, a high thermal conductivity is needed to allow for the management of high thermal loads through rapid cooling of the mirror [62].

- **Oxidation resistance**: In case of accidents like *Vacuum Vessel Ingress of Coolant Event* (VVICE)[1], FMs are expected to be exposed to steam. If their resistance to oxidation is not sufficiently high, their reflectivity could be degraded due to the formation of oxides [63].
- **Behavior under neutron irradiation**: The high neutron flux to which FMs are subjected induces activation and transmutation of the material. A low transmutation rate is preferred because a high degree of mirror material transmutation can lead to a change in the mirror's reflectance due to the accumulation of the transmuted atoms in the lattice [62].
- **Crystal structure**: Polycrystalline (PC) materials are avoided due to strong dependence of sputtering yield on the crystallographic plane of each grain, that causes an increased roughness after plasma exposure and a consequent increase in diffuse reflectivity. On the other hand, single crystals (SC) are studied because they exhibit a uniform erosion rate, thus maintaining a smooth surface indispensable for high specular reflectance. Nanocrystalline (NC) mirrors, that are composed by crystals of nanometric dimension, are of high interest because they show a uniform sputtering resistance; moreover, the production of large-size NC mirrors is cheaper and presents less technical difficulties compared SC mirrors [63].

The most promising materials are rhodium and molybdenum, but in recent years, interest has also grown towards platinum, each of them exhibiting advantages and disadvantages.

Molybdenum has excellent resistance to sputtering, leading to a low and uniform erosion rate under particle flux. Moreover, SC-Mo mirrors have proven to withstand numerous plasma cleaning cycles with negligible surface degradation [66]. However, Mo reflectance is lower with respect to Rh, especially in the UV-VIS range; in addition, Mo is particularly vulnerable to VVICE, because it tends to form a layer of oxide (MoO_3) which causes a drastic decrease in total reflectance [65].

Rhodium exhibits high total reflectivity over the entire spectral range, in particular it is between 70% and 90% in the VIS-NIR range, but the highest reflectivity gain on Pt and Mo is obtained in the UV range. Moreover, Rh reflectivity remains high and almost entirely specular even at high temperatures, at least up to mirror temperature of 640 K [62], and it does not shows degradation after thermal cycles [67]. Even if its sputtering rate is higher than that of Mo, Rh reflectivity remains unchanged even after erosion and

[1]VVICE is an accidental event that could occur following a damage or rupture of the cooling pipes in the vacuum vessel. The steam from the leaked coolant can reach pressures up to 1.5 bar and temperatures up to 250 °C [65].

hundreds of cleaning cycles. For those reasons, Rh has been selected within this thesis work as the material composing the mirror samples.

Platinum has been the subject of interest in recent studies. In particular, it exhibits robust performance during steam ingress events due to the fact that Pt does not form stable oxides. Its behavior under neutron irradiation is also excellent, as it is expected that only 0.04% of Pt atoms would undergo transmutation during the entire ITER lifetime, compared to the 5.93% for Rh atoms. Furthermore, currently Pt is five times cheaper than Rh, and its price is less volatile. However, further studies on platinum are required, and its sputtering rate is higher than that of rhodium; whereas NC-Rh mirrors have already passed various tests regarding long-term plasma erosion, thermal resistance, and more than 100 cleaning cycles [63].

3.3. First mirror test campaigns in JET

Numerous experiments have been carried out over the last two decades to understand the effects of mirror exposure to the plasma in a real tokamak configuration. As part of the First Mirror Test (FMT) program for ITER, the campaigns carried out in the JET tokamak have been of primary importance to investigate whether erosion by the plasma dominates redeposition of impurities or vice versa, and to understand the nature and the thickness of redeposits and the consequences in terms of reflectivity degradation. These effects have been investigated as a function of the mirror's distance from the plasma, ranging from the most exposed mirrors to those in the most hidden and protected positions, by placing the mirrors in specifically designed pan-pipe shaped cassettes. Moreover, the analysis considered their specific location within the vacuum chamber, particularly at the outer mid-plane or under the divertor, as shown in Figure 3.3.

The first two JET campaigns (2005-2007 [68] and 2008-2009 [69]) were characterized by a carbon-based first wall of the tokamak; for this reason, the campaigns are called JET-C. The main result was the degradation of mirror reflectivity in the divertor by 80-90%, due to the formation of carbon-containing flaking co-deposits with a thickness grater than 20 µm on the surface. Deposits were also found on mirrors in the main chamber, mainly on those located deeper in the channel, while on the most exposed mirrors erosion partially compensated for deposition, thus reducing the reflectivity degradation.

Then, during the 2010s, the installation of the ITER-Like Wall (ILW), featuring a Be first wall and a full W divertor, enabled the execution of the JET-ILW campaigns (ILW1-3). Also in this campaigns, the reflectivity degradation on divertor mirrors was significant, ranging from 50% to 80% [70]; however, the composition of deposits was mainly Be and

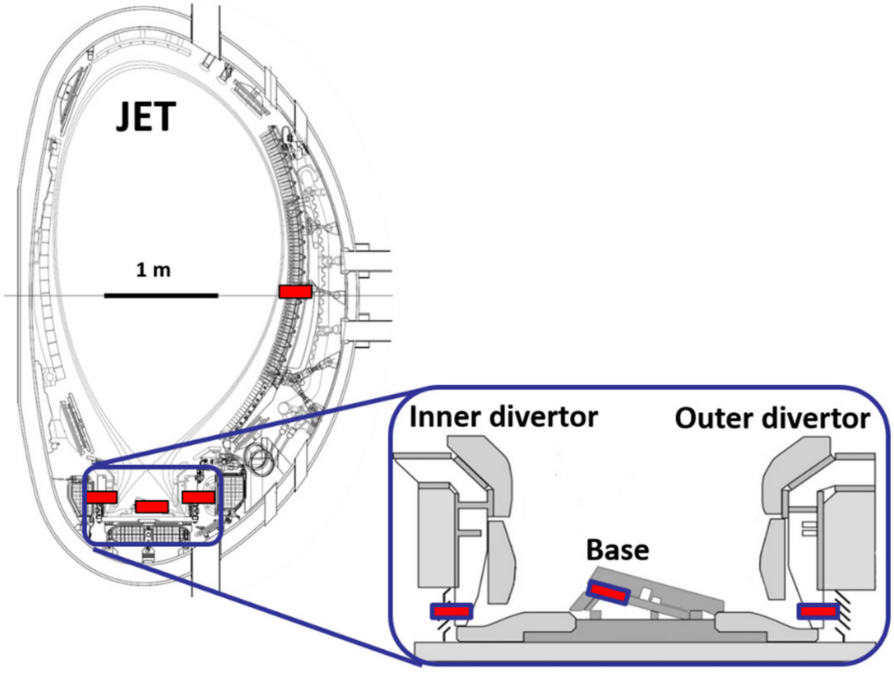

Figure 3.3: First Mirrors location during JET campaigns [66].

the thicknesses were significantly reduced compared to JET-C, reaching 850 nm [66] in the outer divertor after ILW1-3.
The mirrors retrieved from the main chamber did not exhibit a significant change in total reflectivity; however, the diffuse reflectivity increased by a factor of up to five in the UV and visible spectral range, and by a factor of two in NIR [71]. A notable result of the ILW-3 campaign was an eroded mirror in the outer divertor due to the particular position of the strike point. Figure 3.4 shows optical microscopy photos of mirrors after JET campaigns: inhomogeneous deposition, flaking layers and the eroded mirror can be seen.

In the third ILW campaign a particular experiment called *ITER-Like Mirror Test Assembly* (ILMTA) was carried out with the aim of reproducing more accurately the geometry of apertures in the ITER diagnostic first wall. The results in terms of reflectivity degradation were nearly identical to those of the typical cassettes of the First Mirror Test (FMT) program [72].

However, ILW-3 campaign concluded in 2016. Since the ITER new baseline, which includes the decision to adopt a full tungsten first wall with boronization, is recent (2023), large-scale experiments on FMs in tokamaks under similar conditions are still lacking.

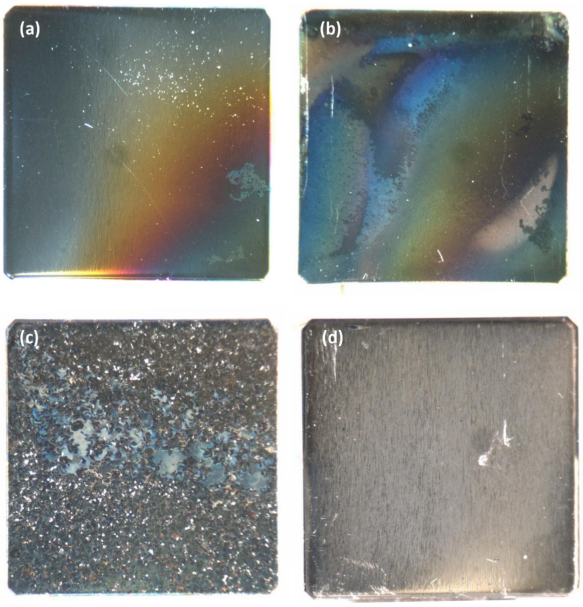

Figure 3.4: Different mirrors retrieved from: (a) divertor base after ILW-3, (b) divertor base after three campaigns (ILW1-3), (c) inner divertor after ILW1-3 with flaking layer, and (d) outer divertor after ILW-3 with eroded surface [71].

3.4. First Mirrors cleaning techniques

Experiments such as the JET campaigns have highlighted the necessity of equipping ITER and future tokamaks with in-situ cleaning techniques for first mirrors; otherwise, frequent replacement would be required, an economically disadvantageous solution that should be avoided.

The most used way to investigate the efficacy of possible FM cleaning techniques is to reproduce samples of mirror materials on a laboratory scale and cover them with layers that imitate the thickness, composition, and morphology of redeposits in tokamaks. This approach is significantly simpler and more flexible than large-scale experimental campaigns in tokamaks, allowing for broader and more thorough studies. Furthermore, due to the recent decision to change the ITER first wall materials, experimental data from operating tokamaks regarding these specific conditions are currently unavailable. Conversely, on a laboratory scale, various cleaning techniques can be employed on the produced surrogate samples to identify the most successful conditions for removing the deposited layer of contaminants.

The goal of these studies is to effectively remove contaminants to achieve the highest possible reflectivity recovery, while minimizing damage (ideally without damage) to the

underlying mirror in terms of erosion, surface melting, or creep. This is crucial because damage to the mirror can irreparably degrade reflectance and significantly reduce the mirror's lifetime.

Furthermore, this method can be also used to study reflectivity degradation due to contaminant species that have not yet been studied in large-scale experiments under real tokamak conditions. This is the case for the effects of FW boronization; since the boron layer is expected to be eroded by the plasma, boron or boron-tungsten deposits are expected to be found on FMs after plasma exposure. Figure 3.5 shows the results of the first ever study on reflectivity degradation due to boron contaminants. It is evident that the impact of even a few nanometers of B deposits has a strong impact on mirror reflectivity, which is much worse than that of a comparable W deposit, in the spectral range 300-1050 nm [73].

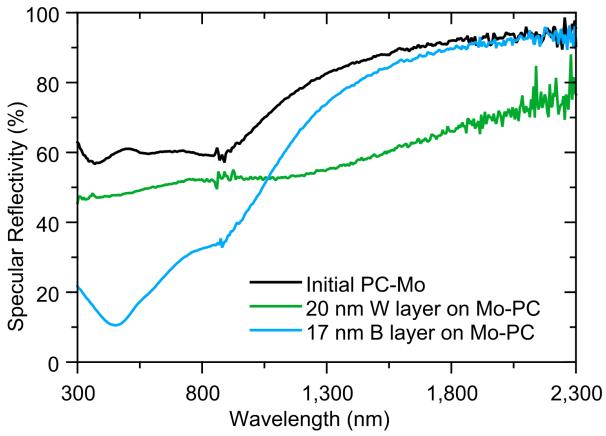

Figure 3.5: Specular reflectivity of a polycrystalline Mo mirror and of the same mirror with a 20 nm W coating and a 17 nm B coating [73].

The two most extensively investigated cleaning techniques are plasma cleaning and laser cleaning, whose working principles and main features are presented in the following sections.

3.4.1. Plasma Cleaning

A well established and widely studied technique to remove contaminants from first mirrors relies on plasma sputtering by energetic ions impinging on the mirror, which in this context acts as the cathode to attract them.

The typical configuration is a Capacitively Coupled Radio-Frequency (CCRF) discharge, in which an RF bias, usually at 13.56 MHz, is applied to the mirror or to its substrate. The lower inertia of electrons compared to ions and the asymmetry of the powered to

grounded areas allow for the formation of a negative DC voltage on the mirror, called *self-bias*, which accelerates ions towards the substrate with sufficiently high energy to remove the coating via sputtering [74].
The self-bias is directly related to the energy gained by the ions, which usually ranges between 150-350 eV to selectively remove redeposits while preserving mirror optical properties [75].
Another characteristic that can be selected for cleaning is the ion species that compose the plasma, usually chosen from Ar^+, He^+, Ne^+ H^+ or D^+ ions. However, the most common choice is Ar^+ because it is more effective in removing W deposits; this is due to the fact that Ar^+ is heavier than He^+, Ne^+, H^+ or D^+, thus enhancing momentum transfer in the sputtering process [76].

Numerous studies have been conducted on materials composing the previous ITER first wall design choices, i.e. C, W, O, Al, or mixed deposits, where Al was employed as a Be proxy due to Be toxicity. They proved that tuning the gas composition and plasma parameters, in particular ion energies, can selectively remove contaminants without damaging the mirror, thus effectively restoring its pristine properties.

Plasma cleaning has shown great efficacy on compact layers of contaminants, as shown in Figure 3.6; however, on porous layers, this technique is much less successful in recovering reflectance, since residues of contaminants tend to remain in some areas, whereas in other regions the mirror is damaged [76]. Moreover, with the presence of a mixture of lighter (B) and heavier (W) elements as contaminants, it is difficult to find a single ion species to employ in plasma cleaning that effectively sputters both.

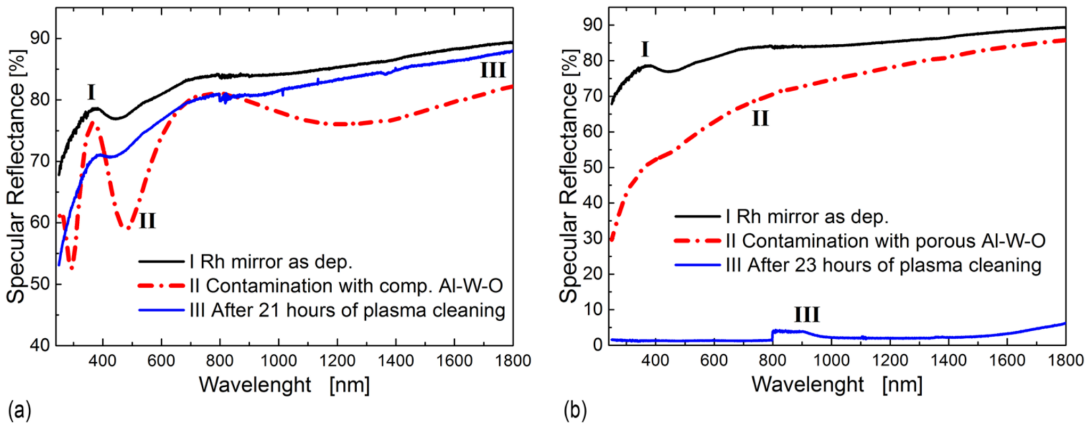

Figure 3.6: Specular reflectivity recovery of a Rh mirror contaminated with (a) compact and (b) porous Al/W/O after plasma cleaning [76].

3.4.2. Laser Cleaning

Laser cleaning is an alternative strategy that employs pulsed laser radiation to remove contaminants. This technique finds application in various sectors such as metal and manufacturing industry[2] [77], preservation of cultural heritage [78], semiconductor manufacturing[3] [79] and nuclear fission industry for decontamination [80]. Thanks to its precision, selectivity, efficiency, flexibility and controllability, laser cleaning is considered the cleaning technology with the highest potential in the 21st century [81].

The physical process underlying laser cleaning is complex because it is based on the competition between all the different phenomena that can happen during the interaction between laser and matter, such as physical decomposition, ionization, expansion, spallation, vaporization, and phase explosion. Both the laser parameters, like pulse duration, fluence and wavelength, and the properties of the material absorbing the pulse determine the *optical penetration depth* and the *thermal diffusion length*, which are crucial parameters that determine the relative importance of each interaction mechanism.

The main laser cleaning principles exploited for fusion applications are explained below, and a schematic of the whole process is presented in Figure 3.7:

- **Laser thermal ablation** starts with absorption of the laser pulse by electrons of the material: in metals absorption is mediated by free electrons, while materials with a band gap require that the energy of the photons composing the laser pulse is enough to excite electrons from the valence to the conduction band, to allow for laser absorption. Then, the absorbed energy causes a rapid increase of the contaminant layer temperature; the layer can be vaporized via ablation if the contaminant temperature exceeds its own gasification threshold.
- **Laser thermal stress** is induced by the fact that the short laser pulse (tipically ns) causes rapid heating and cooling of the irradiated area. This causes quick thermal expansion resulting in thermo-mechanical stresses and a lifting force that can overcome the van der Waals forces keeping the contaminant attached to the mirror. This mechanism can lead to fracture and detachment of the covering layer.

The tuning parameter that allows for selective removal of the contaminants is the laser fluence, which has to be higher than the ablation threshold of the covering layer while

[2]Examples of industrial applications of laser cleaning are the removal of oil films before welding, the removal of coatings and paints before recoating, and the elimination of oxide layers on metals caused by corrosion [77].

[3]Laser cleaning can effectively remove submicroscopic dust particles that compromise the functioning of electronic devices due to the continuous reduction of their characteristic size [79].

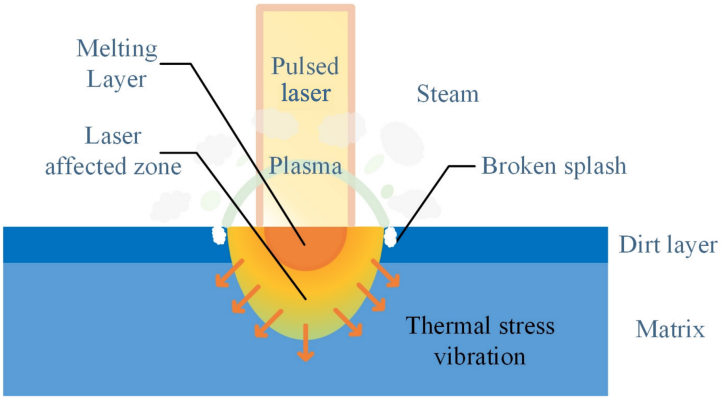

Figure 3.7: Schematic of laser cleaning mechanisms [81].

avoiding leaving melted residues or causing damage to the mirror. The necessity to prevent mirror damage limits the pulse energy and number of subsequent laser pulses that the mirror can withstand, setting an upper limit to the laser fluence that can be used, called the *laser damage threshold*, therefore influencing cleaning efficiency.
However, the laser cleaning of mirrors exposed in JET showed mirror damage despite the utilized fluence being below the measured threshold for stainless steel and molybdenum mirrors, suggesting that the interaction between the mirror surface and the redeposit layer has an impact on mirror resistance, reducing its damage threshold [82].

Previous studies conducted to evaluate the efficacy of this technique in removing tokamak-like contaminants were performed before the new ITER baseline, thus selecting the same materials as plasma cleaning studies: C, W, O and Al as a Be proxy.
Compact carbon deposits were effectively removed by a single scan with the IR wavelength (1064 nm), while to restore the reflectivity of mirrors with porous C deposits, the UV wavelength (266 nm) proved to be more effective [83].

Regarding W/O/Al deposits, IR wavelength proved to be useless due to the fact that tungsten oxides (WO_3) are semiconductors with a band gap of approximately 2.8 eV. Since the energy of each photon in a 1064 nm laser pulse is approximately 1.17 eV, pulses of shorter wavelengths and higher photon energies are needed to be absorbed by the contaminant layer. Indeed, UV scans gave better results than IR ones in terms of reflectivity recovery.
In general, the reflectivity was restored to over than 90% of its initial value in the IR region, while in the UV region the recovery remained lower [84].

Compared to plasma cleaning, laser cleaning proved to be effective in removing both compact and porous layers, with less mirror damage, as showed in Figure 3.8. Furthermore,

laser cleaning is also faster than plasma cleaning, as it requires times on the order of minutes rather than hours. For these reasons, a combined strategy has been proposed to exploit the advantages of both techniques: a laser scan to remove the majority of the contaminants regardless of their morphology, followed by plasma cleaning to remove the residual layer [76].

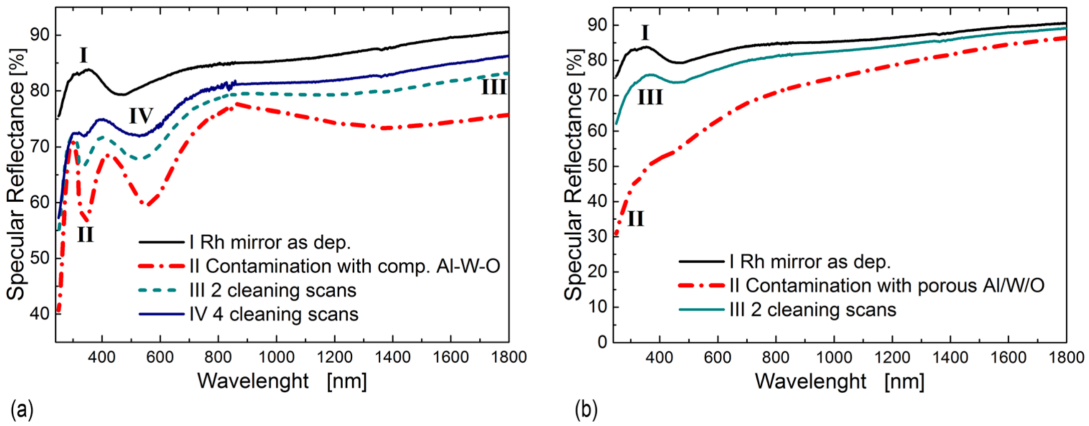

Figure 3.8: Specular reflectivity recovery of a Rh mirror contaminated with (a) compact and (b) porous Al/W/O after UV laser cleaning [76].

However, up to now detailed studies are still lacking on representative first mirror samples concerning boron and boron-tungsten contaminant layers, and their response to plasma and laser cleaning in terms of reflectivity recovery.

3.5. Summary and thesis objectives

At this point, all the necessary elements to understand the thesis objectives have been introduced. Chapter 1 provided a general overview of the motivations and goals guiding nuclear fusion research in the context of global electricity production. A particular focus was placed on the magnetic confinement fusion approach and the largest machines (ITER and DEMO) through which the European fusion community plans to achieve important results in this century.

Chapter 2 highlighted the harsh conditions that must be withstood by the tokamak first wall and plasma facing components during operation, together with the consequent engineering challenges underlying the choice of materials for those components to ensure the best plasma operating conditions. The history of various changes made regarding the FW and PFC material choices have been presented, together with the advantages and disadvantages of each material. Moreover, a description of the current new baseline was presented, which includes a full tungsten FW and boronization as a wall conditioning

treatment.

Chapter 3 introduced the role of diagnostic components in tokamaks, highlighting the peculiar role played by first mirrors in optical diagnostic systems and their characteristics. The plasma-related effects on these components were also presented, in particular the effect of plasma erosion and the redeposition of impurities that dramatically reduce the mirrors' specular reflectivity. Then, the characteristics and efficacy of the most studied cleaning techniques, plasma cleaning and laser cleaning, were described for both mirrors exposed in tokamaks during large experiments and representative mirror samples created at a laboratory scale. The main results obtained with these techniques were also reported, underlining the fact that these results have been derived from experiments on contaminants composed of atomic species that are no longer representative of the most recent decisions about FW materials in ITER.

For these reasons, the primary aim of this thesis is to investigate, at the laboratory scale, the impact of boron and boron-tungsten containing coatings on the reflectivity of rhodium samples. Furthermore, the study focuses on assessing the efficacy of laser cleaning in restoring the mirrors' pristine properties. Particular attention is given to the selection of laser fluences below the laser damage threshold to preserve substrate integrity, and to the comparative investigation of different laser wavelengths to optimize the cleaning process.

To summarize, the specific goals of this thesis are:

1. Production and characterization of B and B/W contaminant layers on Rh mirror samples, evaluating their chemical composition and morphology to ensure their relevance to the real tokamak environment.

2. Evaluation of laser cleaning effectiveness on contaminated samples, with a specific focus on comparing the performance of IR (1064 nm) and green (532 nm) wavelengths in the removal of the deposited layers.

3. Post-cleaning analysis of the samples through reflectivity measurements to quantify the recovery of the mirror's optical performance, combined with the characterization of any remaining residues to assess their impact on the final reflectance and to investigate the laser cleaning mechanism and its efficacy.

4. Assessment of mirror integrity after cleaning to detect any potential laser-induced damage, thus allowing for the identification of the optimal operating parameters for laser cleaning of tokamak-like contaminants.

4 | Experimental set-up and methodology

The majority of the work conducted for this thesis has been carried out at the NanoLab (Micro- and Nanostructured Materials Lab) at the Energy Department of Politecnico di Milano. A distinctive feature of this work is that it was possible to use the same laser device to perform Rh mirror sample production, contamination, and cleaning. The specific experimental apparatus will be described in details in the following sections.

Subsequently, the characterization of the samples has been mainly conducted via Scanning Electron Microscopy (SEM) to investigate the surface morphology and thickness of both mirrors and coatings, and to evaluate the mirror surface quality as well as the nature of the remaining residues after cleaning. Combined with SEM, Energy Dispersive X-ray Spectroscopy (EDXS) has been employed to evaluate the atomic composition and mass thicknesses of contaminant layers.

Reflectivity measurements have been carried out at the ThermALab (Thermal Analysis Lab), at the Energy Department of Politecnico di Milano, via spectrophotometry in the UV-VIS-NIR spectral range.

4.1. Pulsed Laser Deposition

Both the production of Rh mirror samples and the deposition of contaminant layers have been performed via Pulsed Laser Deposition (PLD), which is a well-known Physical Vapor Deposition (PVD) technique whose working principle is explained in the following section.

The high versatility of this technique allows for the production of materials with highly diverse characteristics [85], thanks to the wide variety of parameters that can be selected: laser wavelength, pulse duration, energy per pulse and spot size (which determine laser fluence), background gas pressure, and the distance between target and substrate.

4.1.1. Sample production and contamination

PLD is a widely used technique for the production of thin films based on the laser ablation of a solid target induced by the interaction with a high-intensity, short-pulse focused laser beam. The ablation process takes place if the laser fluence exceeds the ablation threshold of the target material, i.e., if the energy delivered by the laser is sufficient to induce vaporization of the material. The ablated species can include atoms, ions, nanoparticles, or clusters, potentially resulting in microscale droplets; together, these constitute the plasma plume that expands from the target towards the substrate placed in front of it, where the film grows. Figure 4.1 shows a schematic of the vacuum chamber in which the deposition process takes place, including all the main components of the experimental set-up.

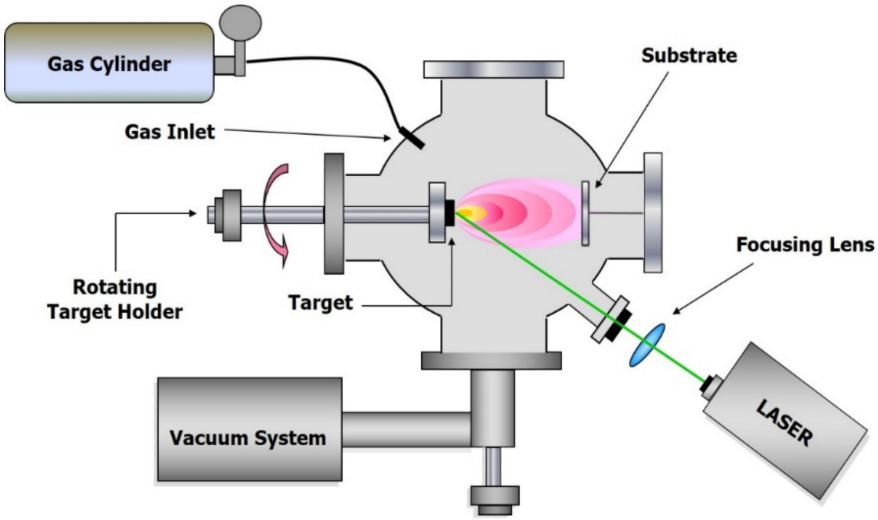

Figure 4.1: Schematic of a typical PLD experimental set-up [86].

As previously mentioned, the variety of parameters that can be tuned with this technique makes it extremely versatile, but can also lead to repeatability issues due to the strong dependence of the deposited film morphology on each specific process parameter, thus frequently requiring extensive parameter optimization [87].

The most important parameters influencing the morphology and the thickness of the deposited layer are explained in the following.

Pulse duration is the parameter that determines the physical basis of the ablation process. The conventional PLD apparatus exploits pulses on the order of a few nanoseconds (ns-PLD). In this regime, the energy absorbed by electrons has time to be transferred to the lattice and converted into heat. Thus, it is a heating mechanism that causes local

melting of the target and subsequent vaporization, generating the plasma plume; this corresponds to classical *thermal ablation* [88]. The long pulse duration, with respect to the ablation dynamics and plume evolution, also allows for intra-pulse interaction between the laser and the plasma plume, causing plasma shielding of the target because the plasma absorbs part of the laser energy. Furthermore, direct emission droplets from the melted material can happen as can be seen in Figure 4.2.
A less widespread technology involves the use of ultrashort laser pulses, on the order of femtoseconds (fs-PLD). This changes the physical mechanism, shifting from thermal ablation to *ultrafast ablation*. Indeed, the laser energy is absorbed only by the electrons, which do not have time to transfer significant heat to the lattice, making the ablation mechanism electronic in nature [89]. This condition avoids laser-plasma interaction and allows for the direct emission of nanoparticles, which drastically changes the morphology of the obtained layer. Figure 4.2 shows a comparison between the effects of long and short laser pulses.

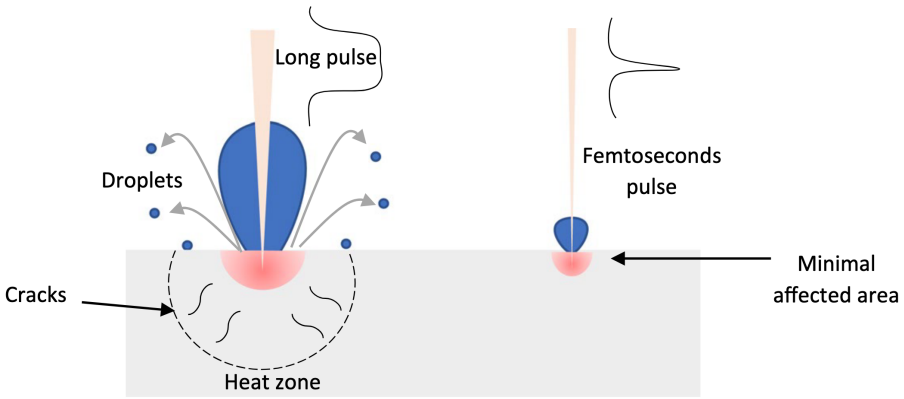

Figure 4.2: Effects of the different duration of the laser pulse on the target [85].

Laser fluence is one of the most important parameters because it has to exceed the ablation threshold of the target material. It is defined as the energy delivered per unit area in a single pulse; thus, it is intrinsically related to the pulse energy and to the spot size on the target, which can be changed through a focusing lens placed outside the vacuum chamber (Fig. 4.1). A higher fluence is associated with higher energy given to the ablated species, but an excessively high fluence leads to the formation of too many droplets, thus generating numerous defects on the deposited layer.

Repetition rate is also a laser parameter to be taken into account. It is necessary to keep it sufficiently low to avoid pulse overlapping on the target, since a second pulse impinging on a region that is still partially melted promotes particle ejection and reduces the reproducibility of the ablation process.

The **distance between the substrate and the target** has an influence on the growth rate, the presence of droplets on the substrate, and the uniformity of the deposition. In particular, a shorter distance results in a higher growth rate but a less uniform radial thickness of the deposited layer; this is due to the geometrical shape of the plume and the angular distribution of ablated species. This distribution generally follows a $cos^n\theta$ profile [90], where θ is the angle with respect to the plume axis, which typically coincides with the normal direction to the target. Moreover, with a shorter substrate-target distance, more droplets are found on the substrate.

The background **pressure** also has a strong impact on the morphology of the deposited layer. Under high vacuum, ablated species travel ballistically and deposit as a compact film on the substrate. Conversely, at elevated background pressures, scattering by gas molecules cools down and confines the plume, promoting the formation of aggregates that assemble to produce porous, foam-like morphologies.

In this work a ns-PLD system has been exploited to produce both Rh mirror samples and boron containing contaminants on them. The whole system is presented in Figure 4.3, where the main components are highlighted.

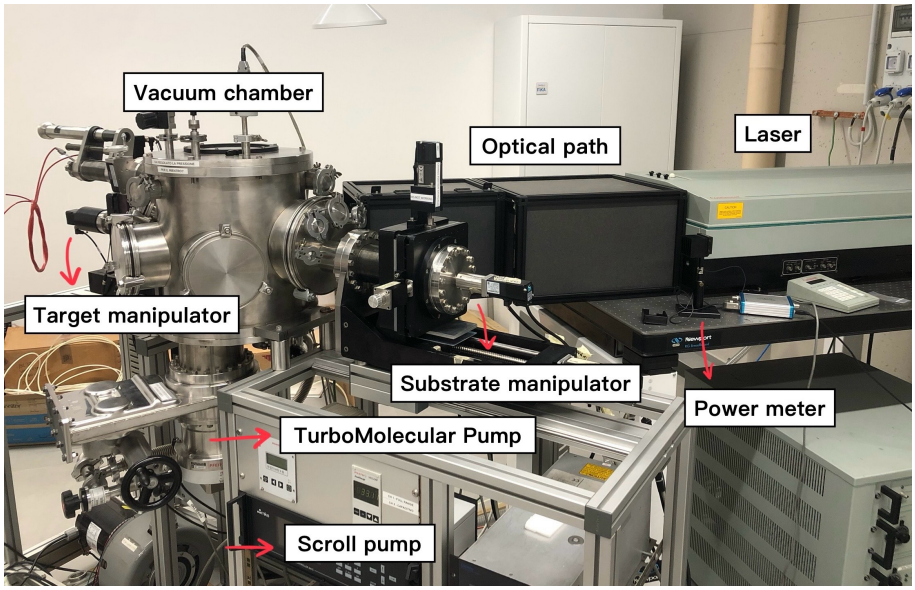

Figure 4.3: Photograph of the PLD system employed in the frame of this thesis.

The laser source is a solid-state Q-switched Nd:YAG (neodymium-doped Yttrium Aluminum Garnet) Continuum Powerlite II 8010 laser, which produces pulses with a duration of approximately 7 $\sim$ 10 ns. Pulses at the fundamental IR wavelength (λ = 1064 nm) are emitted with an energy ranging from 350 mJ to 1600 mJ, as measured by an external power meter. The repetition rate ranges from a minimum of 1 Hz to a maximum of 10

Hz. A non-linear crystal can be used for Second Harmonic Generation (SHG), yielding a green wavelength ($\lambda = 532$ nm); however, the conversion efficiency limits the energy per pulse to a range between 100 mJ and 650 mJ.

The beam spot has a top-hat circular shape with a diameter of approximately 8 mm; it is directed towards the vacuum chamber through an optical path consisting of mirrors and a focusing lens, used to adjust the beam spot size on the target. Inside the vacuum chamber, the laser is incident on the target at an angle of 45° to limit laser-plume interaction.

The deposition chamber is a cylindrical stainless steel high-vacuum chamber with a radius and height of 40 cm. It features numerous access ports to allow laser entry through a window, target and substrate holders, a pumping system, a gas inlet and pressure gauges.

Both the target and the substrate holders are mounted on motors that ensure remote control of their position and movement; the substrate position remains fixed during operation at a location that guarantees the correct distance from the target and the correct alignment with respect to the plume axis, while rotating to maximize deposition uniformity. Target motion is essential during deposition; it is programmed to make the laser follow a helical path on the target to ensure the most uniform ablation possible.

A scroll pump and a TurboMolecular Pump (TMP) constitute the pumping system. The scroll pump depressurizes the chamber to ~ 10 Pa working under viscous flow conditions. Then, with the TMP a pressure of 10^{-3} can be reached working under molecular flow conditions.

A suitable flow-meter system allows for the injection of gasses such as Ar, He, O_2 and N_2 into the chamber. The gas flow can be regulated with an accuracy of 0.1 sccm (standard cubic centimeter per minute). The combination of this system with the action of the TMP enables the desired deposition pressure to be achieved and maintained.

For mirror production, the target employed was a Rh disc with a radius of 25.4 mm, while the substrates were monocrystalline (100) silicon wafers. Subsequently, a Boron target of the same dimensions was used for the deposition of contaminant layers onto the previously produced Rh mirrors. For the deposition of mixed boron-tungsten contaminants, a piece of tungsten with an area of 115 mm^2 was added to the boron target.

4.1.2. Laser Cleaning

The cleaning procedures were performed using the same laser system used for PLD, but with the key difference that the mirrors were placed at the target position to allow the laser to irradiate them, as shown in Figure 4.4.

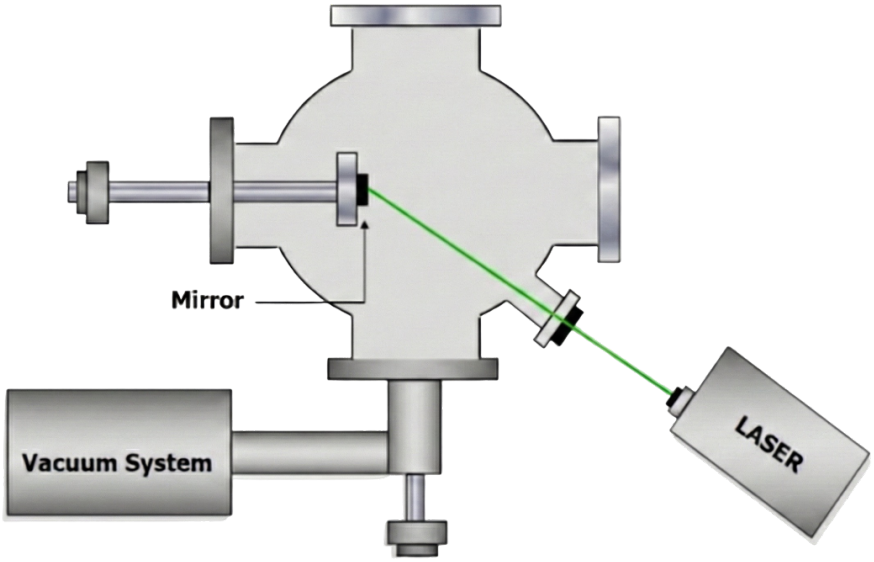

Figure 4.4: Laser cleaning setup, adapted from [85].

A fundamental difference compared to the PLD setup is the absence of the focusing lens. This is crucial because a focused laser spot on the mirror would result in excessive fluence, which would severely damage the mirror. Furthermore, achieving uniform ablation would be extremely challenging, and the selectivity of the cleaning process would be lost. Thus, the laser spot on the mirror had the shape of an ellipse with the semi-major axis of 5 mm and the semi-minor axis of 3 mm.

During mirror damage tests, the irradiated samples were pristine Rh mirrors, which had never been contaminated with boron-containing coatings. Conversely, during cleaning experiments, contaminated mirrors were exposed to the 1064 nm or 532 nm laser beam, with the aim of comparing the results.

4.2. Characterization

Following sample production, characterization extending beyond visual inspection is essential to evaluate key physical properties of both mirrors and coatings, such as morphology, thickness, atomic composition, and reflectivity, which are crucial to this study.

4.2.1. Scanning Electron Microscopy

Scanning electron microscopy is a technique that enables the acquisition of high-resolution images of sample surfaces and cross-sections, allowing for the visualization of micrometric and nanometric features of the materials.

A conventional optical microscope employs visible light as probe on the sample, but its wavelengths in the range of hudreds of nm cause an intrinsic limit to the resolution of the instrument due to the diffraction limit. This limit can be overcome using electrons as probes, whose De Broglie length depends on the accelerating voltage and can reach much lower values compared to visible light, thus shifting down the minimum dimension that can be resolved due to diffraction limit [91].

The instrument that exploits this principle is the Scanning Electron Microscope (SEM) whose schematic representation is given in Figure 4.5.

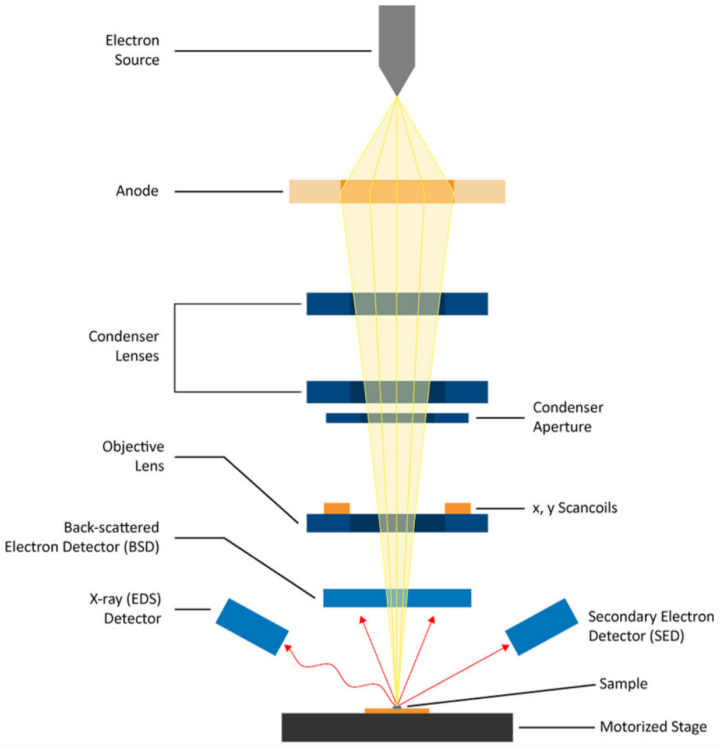

Figure 4.5: Schematic of the path that electrons follow in a SEM [92].

The electrons are extracted via the thermionic effect from a heated tungsten filament, and are then collimated and accelerated towards the sample, placed in a vacuum chamber, with an accelerating voltage generally between 0.3 and 30 kV. Upon interaction with the sample, several processes may occur: the electrons can undergo elastic or inelastic scattering, or induce the emission of secondary electrons and characteristic X-rays from the surface atoms. Secondary electrons are generated by the collision of impinging electrons with atomic electrons within the material, while X-rays originate from the radiative de-excitation of atoms following inelastic scattering events.

SEM is able to collect different signals and reconstruct detailed images from them. Backscat-

tered electrons (BSE) are those from the primary electron beam that undergo elastic collisions; due to their higher energy, they can escape from deeper within the material, meaning that the signal originates from a larger interaction volume. The weak dependence of the BSE signal on the local surface slope generates 2D images more sensitive to the contrast between different Z elements. Conversely, secondary electrons (SE) have lower energy and can only escape from the first few nanometers of the surface; thus, their signal is affected by shadowing effects, giving the reconstructed images a 3D appearance.

In this thesis a Zeiss SEM supra 40 at Politecnico di Milano was exploited to produce sample images with electron energy ranging from 5 keV to 10 keV.

4.2.2. Energy Dispersive X-ray Spectroscopy

During the interaction of probe electrons with the sample during a SEM measurement, the atoms of the material undergo ionization and excitation via the ejection of inner shell electrons. The subsequent de-excitation, if radiative, involves an outer shell electron that takes the place of the ejected electron, thus reducing its energy[1] and releasing the energy difference in the form of X-ray photons. They are a characteristic footprint of each atom because they are emitted exactly at energies corresponding to the difference between electronic levels, which in each atom are uniquely identified and known.

For this reason the amount and the energy of those characteristic X-rays is important to be collected and can give information on the atomic composition of the material, through a technique called Energy Dispersive X-ray Spectroscopy (EDXS) [93], which is usually integrated within the SEM instrument. This system shows as output energy spectra with peaks corresponding to the different atomic species composing the film.

During this work, EDXS data were collected to evaluate the atomic composition of the mirror contaminants and subsequently analyzed with the EDDIE software, which is specifically designed to retrieve information from EDXS data.

EDDIE

The comparison of EDXS data of multi-elemental films with a database of homogeneous reference sample data with known composition is a well-established procedure in Electron Probe Microanalysis (EPMA), which allows obtaining information such as the mass thickness of the analyzed film. This technique relies on known reference standards for the analyzed films. Since these reference standards are not always available, as in this study,

[1]The electron in the inner shell is more tightly bound, meaning that its binding energy is higher in absolute value (more negative) than the one in an outer shell.

due to the a priori unknown composition of the produced films, a reference-free method to extract atomic composition and mass thicknesses of unknown films was needed. For this reason, Pazzaglia et al. [94] developed the EDDIE software.

This software computes the ratio of the X-ray intensity signal obtained from the EDXS measurement originating from the film material to that of the substrate, thereby creating the K-ratios. Based on a model that relates these K-ratios to the atomic composition and the mass thickness of the analyzed film through an iterative procedure, it is possible to obtain these film properties without the need for a standard reference sample.

The model accounts for the physics of the process through various parameters such as the detector efficiency, which is different for each X-ray energy, the attenuation coefficient of the substrate depending on the angle of the detector with respect to the sample surface. The depth distribution of X-ray generation is not trivial since it depends on the physics behind electron multiple scattering and geometrical properties of the film. In this model it is computed analitically through an electron transport kinetic model.

Overall, this software allows the calculation of mass thicknesses and atomic composition of unknown films with uncertainties of about 15%. It requires as input parameters the K-ratios obtained from EDXS data and initial guesses regarding film mass thickness and atomic composition. At each iteration, the software computes the depth distribution of X-ray generation and adjusts the input parameters to find the values that best fit the experimental K-ratios, within an acceptable error.

The selection of the working electron energy has been crucial in this study during the analysis of coated mirrors. The reason is that an excessively low electron energy does not penetrate to a sufficient depth to yield sufficient signal intensity from the underlying Rh mirror, thereby preventing the calculation of an experimentally valid K-ratio. On the other hand, an excessively high electron energy would penetrate to a depth sufficient to reach the silicon under the Rh mirror. The signal from silicon in an EDXS spectrum is undesired in this work, because it induces errors in the EDDIE software, which assumes the thickness of the underlying layer is infinite. The optimal compromise to have a sufficiently high signal intensity from Rh while minimizing the signal from Si has been found in this work to be 7.5 keV.

4.2.3. Reflectance measurements

The macroscopic optical properties of a material are related to its behaviour with respect to the interaction of light, which can be either absorbed, transmitted, or reflected by the

material itself. These optical properties are encapsulated in the *refractive index*:

$$\tilde{n} = n' + \mathrm{i}n'' \tag{4.1}$$

It is a complex quantity whose real part is related to the phase velocity with which light propagates, and the imaginary part describes the absorption of light inside the material.

Reflection of light by a material happens due to the discontinuity of the refractive index at the interface between two different media. This discrepancy imposes boundary conditions on the electric and magnetic fields composing the incident light that cannot be satisfied by solely the transmitted part. Thus, the generation of a reflected wave is necessary to guarantee energy and momentum conservation at the interface [95].

The amount of reflected light is expressed through Fresnel equations. In the simplified case of normal incidence on an ideal perfectly flat interface between two media, characterized by $\tilde{n}_1$ and $\tilde{n}_2$, the reflectivity, which is entirely specular, can be expressed as:

$$R_{\mathrm{spec}} = \left| \frac{\tilde{n}_1 - \tilde{n}_2}{\tilde{n}_1 + \tilde{n}_2} \right|^2 \tag{4.2}$$

Since in a realistic case the interface is never perfectly flat, there exists a diffuse component of the reflectivity (R_{diff}) which is caused by the scattering of light in random directions due to the presence of surface defects or roughness. The hemispherical reflectivity, commonly referred to as total reflectivity (R_{tot}), is defined by the intensity ratio of the reflected light to the incident light and is composed of both the specular and the diffuse reflectivity:

$$R_{\mathrm{tot}} = R_{\mathrm{spec}} + R_{\mathrm{diff}} \tag{4.3}$$

where all of them depend on the considered incident wavelength.

In the specific case of the thin films employed in this work, the interference phenomenon plays a crucial role in the optical properties of the samples. Since the contaminant film thicknesses are of the same order of magnitude as the light wavelength, the light waves reflected by the air-coating interface superimpose on the ones reflected by the coating-mirror interface. If the the difference in the optical path traveled by the two waves is an integer multiple of the wavelength, the interference is constructive and reflectivity shows a maximum. On the other hand, if the optical path difference is a half-integer multiple of the wavelength, the interference is destructive and the reflectivity shows a minimum. In the case of a thin layer on a thick substrate, the spectral position of the maxima and

the minima depends on the real part of the refractive index (n'), which determines the velocity at which the light travels through the thickness (t) of the thin film. Thus, for normal incidence, the interference extrema can be expressed by the condition:

$$\lambda_{\max,m} = 2t\frac{n'}{m} \qquad \lambda_{\min,m} = \frac{2tn'}{m+\frac{1}{2}} \tag{4.4}$$

where m is an integer number representing the interference order.

Since the imaginary part of the refractive index (n'') is related to absorption, it determines the amplitude of the interferences fringes. The intensity $I(z)$ of the wave propagating inside the thin film for a distance z undergoes exponential attenuation following Lambert-Beer law:

$$I(z) = I_0 e^{-\alpha z} = I_0 e^{-\frac{4\pi n''}{\lambda}z} \tag{4.5}$$

where $\alpha = \frac{4\pi n''}{\lambda}$ is the attenuation coefficient. It means that a higher value of n'' dampens the intensity of light that undergoes reflection at the film-substrate interface and makes the interference pattern less pronounced.

Spectrophotometer

For the reflectance measurements of this thesis, a PerkinElmer UV-vis-NIR spectrophotometer Lambda 950 has been employed. The configuration included a 150 mm integrating sphere with a double detector, including an InGaAs detector for the NIR spectral region.

This instrument is based on a double-beam configuration for ratio recording, as shown in Figure 4.6. During the measurement, the incident light is sent alternatively along the sample path and the reference path, and the measured signal is the ratio $I_{\text{sample}}/I_{\text{ref}}$. This approach is crucial for the accuracy of the measurement because it compensates for possible instabilities, allowing for reproducible measurements [96].

The integrating sphere is made of Spectralon, a material composed of sintered polytetrafluoroethylene (PTFE), which is characterized by a reflectivity close to 100%, almost entirely diffuse, over the whole spectral range. This configuration allows for the measurement of hemispherical reflectivity by integrating the light reflected by the sample over the angular distribution inside the sphere. It is also possible to measure only the diffuse reflectivity by opening the specular port (Fig. 4.6), thus excluding the specular component from the measurement. Finally, the specular reflectivity can be obtained from the hemispherical and the diffuse ones by subtraction according to Eq. 4.3.

The reflectance sample port of the employed spectrophotometer has a diameter of 1 in.

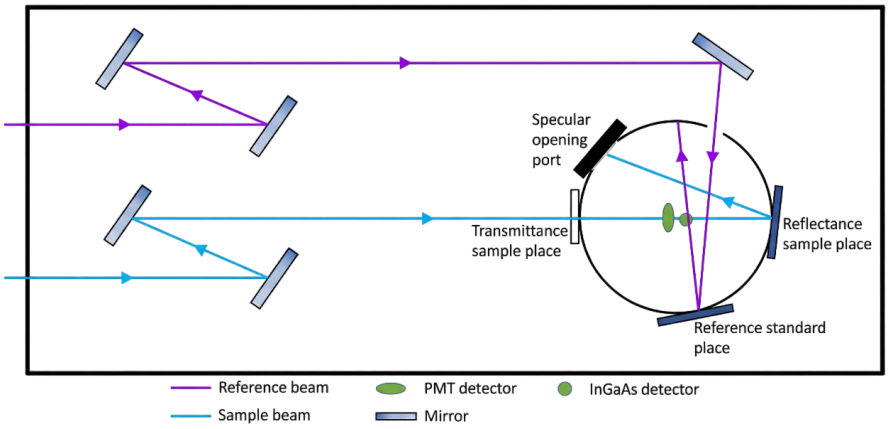

Figure 4.6: Schematic of a dual-beam configuration spectrophotometer with integrating sphere [97].

This feature sets a lower limit to the dimensions of the samples that can be measured. Thus, in this work, square mirrors with a side length of 26 mm were produced to allow for subsequent reflectance measurements.

5 | Production of mirrors and contaminants

5.1. Rh mirrors

The use of PLD technique to produce rhodium mirror samples is consolidated within the NanoLab group at Politecnico di Milano [98, 99]. In particular, in this work the desired morphology of the Rh film was a highly oriented nanocrystalline structure with a preferential growth direction (100), due to the fact that it shows a higher adhesion to the substrate compared to the amorphous morphology, thus guaranteeing a higher damage threshold [100]. The operating condition to ensure the optimal film were: high vacuum (corresponding to background pressure of about 10^{-3} Pa), IR laser wavelength ($\lambda = 1064$ nm), repetition rate of 10 Hz, energy per pulse of 1.4 J corresponding to a fluence on the target of 16 J/cm^2, distance between substrate and target of 6 cm. The silicon substrates were placed on the substrate holder as shown in Figure 5.1.

The mirrors were produced in two different sizes for different purposes. The larger mirror in the center of the substrate holder has a side length of 26 mm, which was necessary for subsequent reflectivity measurements with the spectrophotometer described in Section 4.2.3; thus, mirrors of that size have been subsequently coated with the coating morphology of interest for the following laser cleaning procedure. The smaller samples have a side length of 11 mm and have been subsequently used to perform laser damage tests if left as deposited, to perform trials of cleaning to find the best cleaning conditions on contaminated mirrors to be repeated on the larger mirrors, and to perform SEM and EDXS characterization of the produced contaminants layer.

The central position of the larger sample allowed reaching a thickness of the rhodium mirror of 390 nm in the center and 320 nm at the center of the square side in 30 minutes of deposition. Since the smaller samples were placed at a larger angular position with respect to the axis of the plasma plume during the deposition, the deposition rate was lower. Thus, to ensure a uniform mirror thickness, two depositions of 30 minutes each

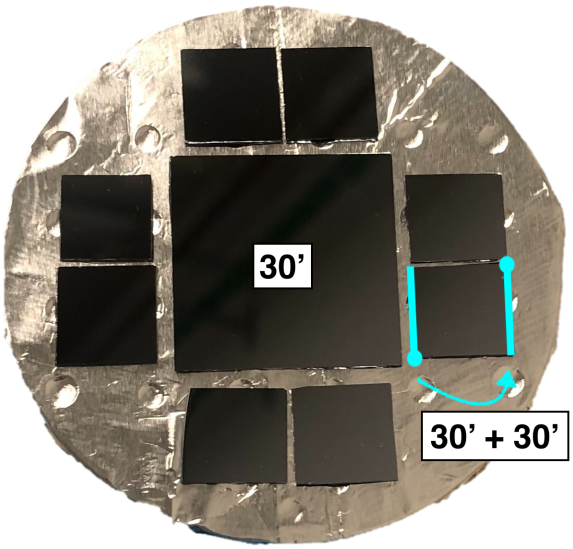

Figure 5.1: Configuration of silicon substrates on the substrate holder. Deposition times are written on the samples.

were necessary: after the first 30 minutes, the samples were rotated by 180° with respect to the axis passing perpendicularly through the center of the square, such that the side oriented towards the larger sample took the place of the side placed in the outer radial position with respect to the center of the sample-holder. This methodology is graphically explained in Figure 5.1 and allowed reaching a thickness of almost 300 nm in 60 minutes.

Figure 5.2 shows SEM top-view images of the produced Rh mirrors at different magnifications, while Figure 5.3 shows a cross-section image of the same sample. The characteristic nanometer-sized grains of the nanocrystalline structure are clearly visible both in the top-view (Fig. 5.2(b)) and in the cross-section (Fig. 5.3). The low-magnification top-view (Fig. 5.2(a)) shows some droplets, which are typical defects associated with ns-PLD.

Figure 5.4 shows the reflectivity of the produced coatings. All the reflectivity measurements in this work have been performed with the spectrophotometer described in Section 4.2.3 in the spectral range from 250 nm to 2500 nm.

In particular, Figure 5.4(a) presents three lines, all associated with hemispherical reflectances: the Spectralon reflectivity (yellow line), the Rh reflectance as measured by the instrument (red line), and the effective Rh reflectance (blue line), obtained as the ratio of the measured Rh reflectance to the Spectralon reflectance. This procedure was necessary to obtain the true hemispherical reflectance measurement of all the samples measured in this work, since all the hemispherical reflectance spectra recorded by the instrument intrinsically contained some artifacts associated with the Spectralon, such as the peak and

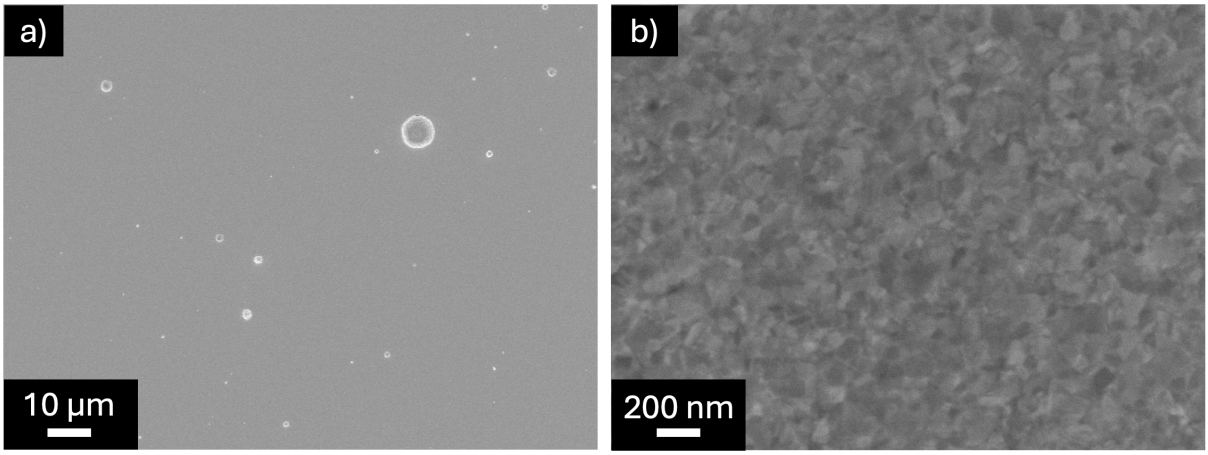

Figure 5.2: SEM top-view images of the Rh mirror acquired at (a) 2,000× and (b) 100,000× magnification.

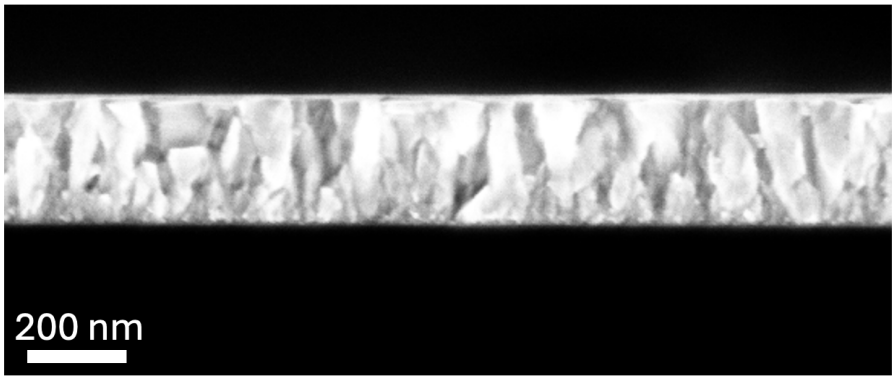

Figure 5.3: SEM cross-section image of the Rh mirror.

valley visible in the IR region around λ=2200 nm. The reason for this correction is the fact that the reflectance of all the measured samples has a high specular component: this feature leads to the fact that, during a total reflectance measurement, when the sample beam impinges on the sample (Fig. 4.6), it is almost entirely directed towards the specular port plug, which is made of Spectralon and diffuses the beam throughout the integrating sphere. This mechanism results in the measurement output being $R_{\text{sample}} \times R_{\text{Spectralon}}$ in the case of samples with high specular reflectance. Thus, simply dividing the measured sample reflectance by the Spectralon reflectance allows obtaining a spectrum which is more representative of the total reflectance of the sample.

The total reflectance shown in Figure 5.4(a) as the blue line exhibits values between 65% and 78% in the UV-vis range, together with a dip around 500 nm which is typical of Rh due to the fact that photons at those energies induce interband absorption in the metal [101]. Moreover, the reflectance increases monotonically in the IR spectral region,

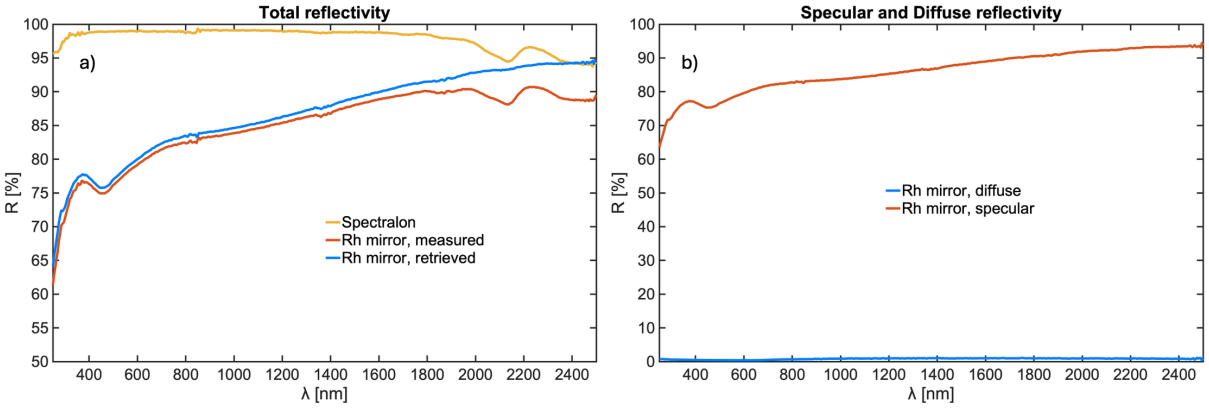

Figure 5.4: Total (a), specular and diffuse (b) reflectivity of Rh films deposited via PLD.

reaching up to 95%.

The specular (red line) and diffuse (blue line) reflectance spectra are presented in Figure 5.4 (b). The specular reflectance follows the profile of the total reflectance almost perfectly, consistent with the fact that the diffuse reflectance is close to zero over the whole spectral range. This suggests that the sample surface exhibits a high optical quality as a mirror, with no surface defects that could scatter light away from the specular direction, and possesses a negligible roughness compared to the incident wavelengths.

5.2. Production of contaminants

The selection of the main material composing the contaminants of the mirror samples was made in order to reproduce, at a laboratory scale, conditions relevant to a tokamak environment. For this reason, the main material on which all the contaminant films produced in this work are based is boron. Indeed, since boronization will be employed as a first wall conditioning technique in ITER, as explained in Section 2.2.1, the boron layer will be the first element exposed to plasma erosion during operation; thus, boron is expected to be the main component of redeposits affecting the reflectivity of first mirrors.

However, in the regions of the first wall that are more exposed to erosion, the lifetime of the boron layer is short, and the underlying tungsten becomes exposed to plasma sputtering. Thus, it is also necessary to study the impact of contaminant layers containing a small percentage of tungsten mixed with boron on the reflectivity of first mirrors.

The production of boron films via Pulsed Laser Deposition, which allows achieving various film morphologies at a much higher deposition rate compared to other deposition techniques such as magnetron sputtering [102], has been exploited in the NanoLab group for different applications, including novel experiments regarding cross-section investigations

of the p-^{11}B (Eq. 1.11) fusion reaction [103].

In this work the mirror samples were coated with two different kind of contaminant coatings: the first containing boron and the second containing both boron and tungsten. In both cases a small atomic percentage of oxygen, in the order of few percent, is found in the coatings.

Before reaching the desired coating to be reproduced on mirrors, numerous trials have been made on silicon samples with the goal of analyzing, via SEM and EDXS characterization, the impact of different PLD parameters on coating properties, morphology, and atomic composition. The selection of optimal PLD parameters for the production of the desired coatings was made with the goal of obtaining coatings that do not change over time, specifically due to oxidation upon exposure to ambient air, thus ensuring experimental repeatability. Indeed, a boron coating whose optical properties do not remain the same upon contact with air is not of interest in this context, since in a real tokamak environment air exposure is not foreseen.

After the required analysis of the characteristics of the trial silicon samples, the deposition on Rh mirrors was performed with the green laser wavelength ($\lambda = 532$ nm), under high vacuum conditions (P$\sim 10^{-3}$ Pa), with a repetition rate of 10 Hz, an energy per pulse of about 650 mJ corresponding to a fluence on the target of 7.4 J/cm^2 (considering a laser spot size of 8.8 mm^2 on the target), a distance of 9 cm between the target and the substrate, and a deposition time of 13 minutes.

The substrate holder for the depositions on Rh was equipped in a similar way to the one shown in Figure 5.1, but with Rh mirrors previously deposited on silicon rather than bare silicon substrates. The larger mirror was placed at the center, while two or three smaller mirrors were placed at the outer radial positions and were subsequently used for laser cleaning trials. In each deposition cycle, an additional silicon sample (15 mm $\times$ 15 mm) was placed radially to provide a reference sample allowing the full characterization of the boron-containing coating keeping intact[1] the mirror samples.

5.2.1. B contaminants

The deposited boron contaminant layer showed a compact structure due to the high vacuum condition during deposition. Figure 5.5 show the SEM top-view images at two different magnifications of the produced coating on the mirror sample. The surface appears flat with an amorphous morphology and some sporadic surface defects in the form

[1]To analyze the cross-section morphology and thickness of the sample via SEM, it is necessary to cut the sample.

of droplets, whose number is minimized thanks to the 9 cm target-substrate distance. The cross-section image of such a B coating on the Rh mirror is shown in Figure 5.6.

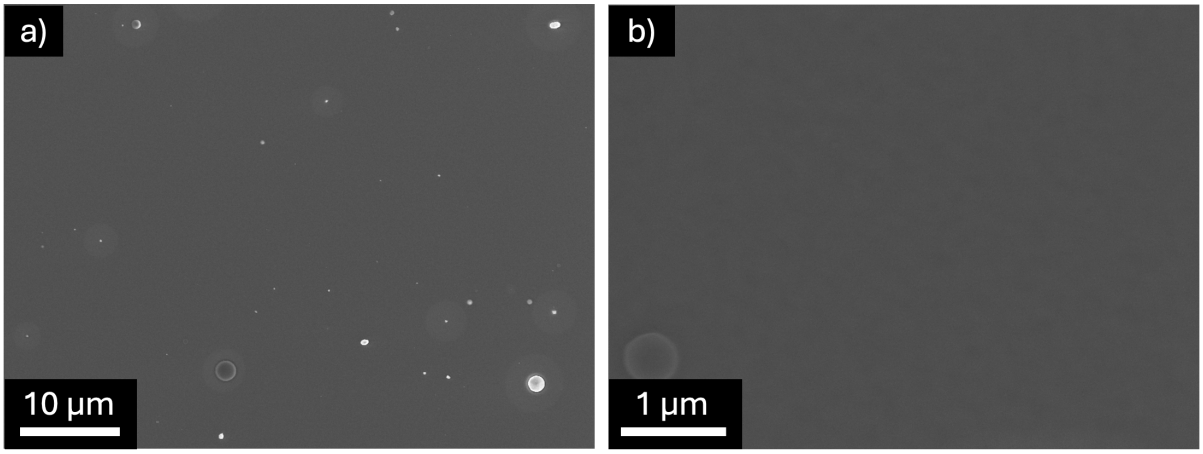

Figure 5.5: SEM top-view images of the B coating on the Rh mirror acquired at (a) 5,000× and (b) 50,000× magnification.

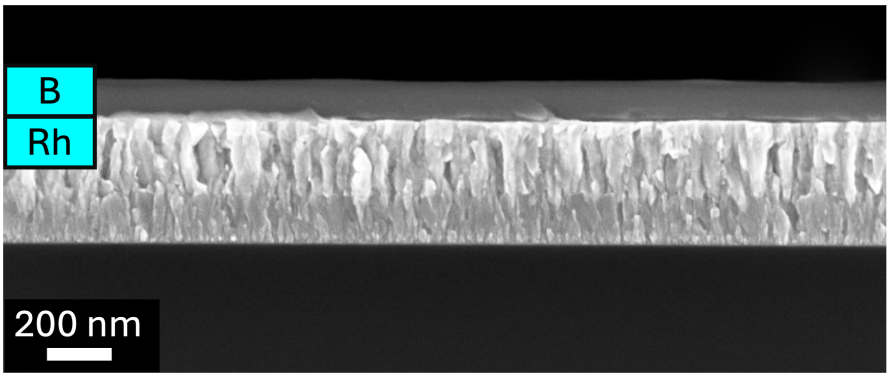

Figure 5.6: SEM cross-section image of the B coating on the Rh mirror.

Figure 5.7 shows a picture of one of the larger mirrors coated with the boron contaminant layer. The visual appearance shows a color gradient that is compatible with the fact that the intrinsic geometry of the plasma plume, which directs the ablated species mainly towards the center of the substrate, creates a layer whose thickness decreases with increasing radial position. Thus, the film thickness varies from about 200 nm at the center to about 160 nm at the edge, as determined through SEM cross-section images. This thickness variation has an impact on the optical properties of the sample; in particular, the wavelengths corresponding to interference maxima and minima are determined by the interference condition (Eq. 4.4), in which the thickness of the sample plays a crucial role.

Figure 5.8 shows the EDXS spectrum measured at the center of the sample. The boron and oxygen peaks originating from the film are clearly visible, as well as the rhodium peak

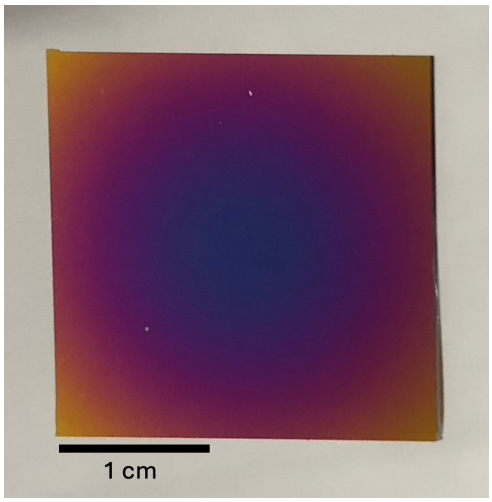

Figure 5.7: Photograph of Rh mirror with boron contaminant film.

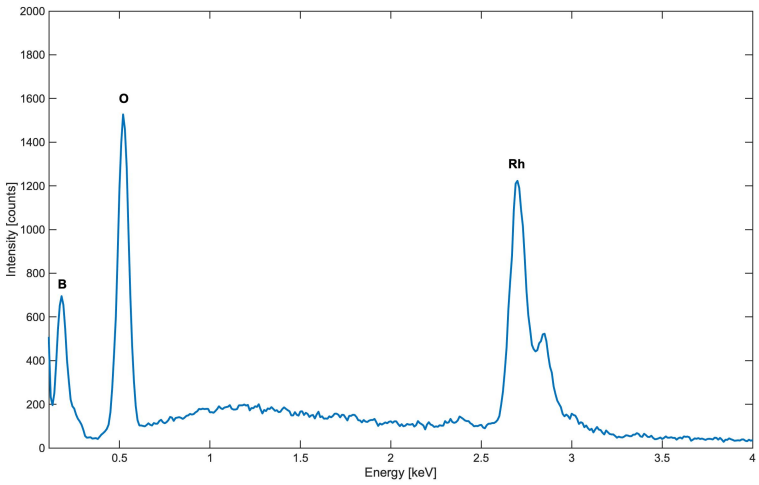

Figure 5.8: EDXS spectrum of the B coating on the Rh mirror.

corresponding to the underlying mirror. Using the data obtained from this spectrum and two additional spectra measured in the same area to improve measurement statistics, the EDDIE software was employed to retrieve the mass thickness and atomic composition of the film. The obtained values are a mass thickness of 34.967 µg/cm^2, corresponding to a density of 1.748 g/cm^3, with an atomic composition of 85.745% boron and 14.255% oxygen.

The reflectance of the sample presented in Figure 5.7 has been measured, and its behavior compared to the as-deposited Rh mirror is shown in Figure 5.9. Overall, the optical properties of the pristine mirror are significantly affected by the presence of the contaminant layer.

The total reflectance (Fig. 5.9(a)) of the boron film (purple line) shows wide oscillations which are typical of the thin-film interference phenomenon already described in section 4.2.3, with clearly visible interference maxima and minima. In particular, it is interesting to note the deep interference minimum around 585 nm (in the orange-yellow region), where the reflectance drops below 10%, and the maximum in the blue-violet region around 450 nm. The suppression of longer visible wavelengths and the preferential reflection of shorter wavelengths in the visible range clearly explain the purple color of the sample, which is evident from visual inspection in Figure 5.7. The maximum reflectance is found at wavelengths around 955 nm; in the IR region, the interference continues with large oscillations, but the mean reflectance remains lower than that of rhodium, ranging between 60% and 80%.

Figure 5.9(b) shows the behavior of the diffuse component of the reflectance. It remains low with values below 2.5%, thus maintaining the dominance of the specular component, although the diffuse one shows a slight increase compared to the pristine mirror.
The presence of oscillations in the diffuse reflectance with the same periodicity as the oscillations in the total reflectance suggests that the surface roughness of the boron film could reproduce that of the rhodium mirror. As a consequence, the waves scattered by the two interfaces maintain a fixed phase difference determined by the film thickness, thus leading to constructive and destructive interference phenomena which are analogous to those observed in the specular reflectance.

The specular component is not shown in the graph because it is almost equal to the total reflectance, due to the low values associated with the diffuse component.

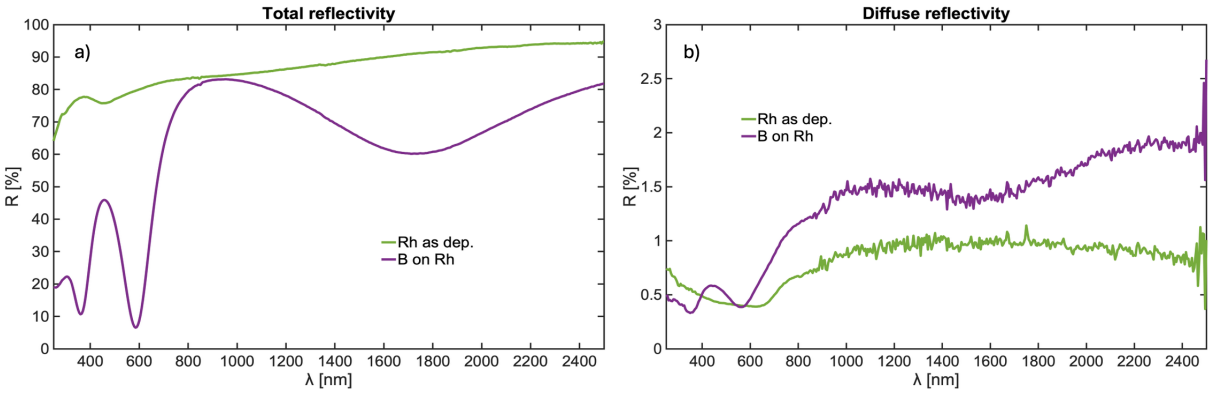

Figure 5.9: Total (a) and diffuse (b) reflectance of the boron film (purple line) deposited on the rhodium sample (green line).

Attempts at the synthesis of porous B coatings

The PLD setup is known to be very versatile and also suitable for the production of porous films [104], by taking advantage of injecting gases into the deposition chamber, which allows working with a controlled pressure. As already described in Section 4.1, the interaction of the plasma plume with the injected gas atoms slows down the ablated species and leads to the formation of porous structures on the substrate.

Thus, with the aim of investigating the behavior in terms of reflectance loss and cleaning response of films with morphological characteristics different from the already presented compact ones, further depositions of trial boron contaminant coatings have been carried out. In particular, two depositions have been performed keeping almost all the deposition parameters fixed and equal to those used during the depositions for the production of compact coatings: repetition rate of 10 Hz, laser fluence on the target of 7.4 J/cm^2, target-substrate distance of 9 cm. The only parameter changed with respect to the previous depositions was the background pressure in the chamber; specifically, argon gas was injected to perform two depositions with pressures of 5 Pa and 10 Pa, respectively.

However, the obtained coatings were not considered satisfactory because air exposure after deposition induced chemical modifications to the produced coating, likely caused by oxidation and the subsequent formation of boric acid [105]. The structures that grew on the coating after deposition are shown in Figure 5.10. Furthermore, the visual appearance of the coating changes over a period of days, due to the growth and modification of the various structures that start to form right after the exposure of the sample to the air.

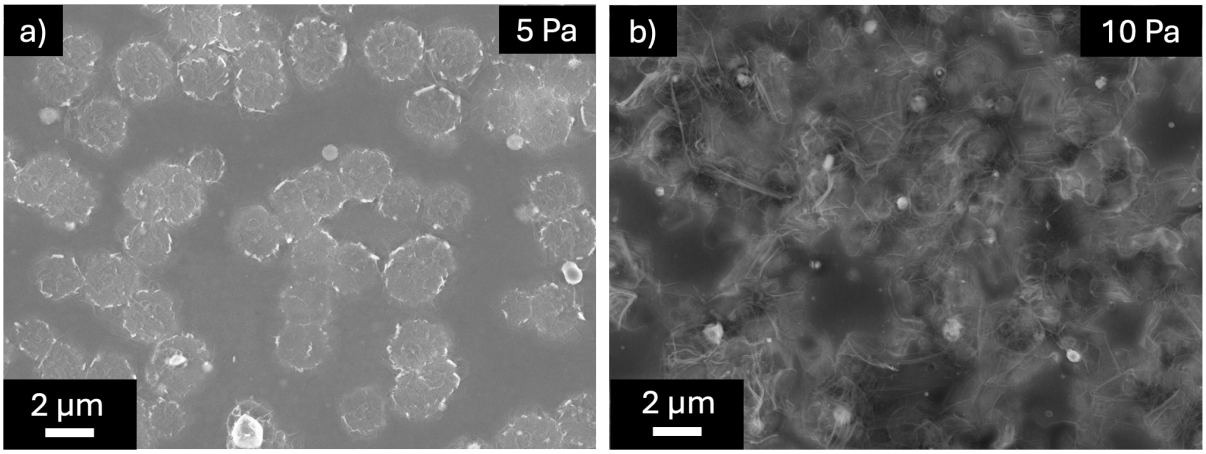

Figure 5.10: SEM images of the B coatings deposited with a background Ar pressure of (a) 5 Pa and (b) 10 Pa.

The fact that the coating surface is not stable under air exposure made these coatings

unrepresentative of real tokamak conditions, since in the vacuum chamber the presence of air is not expected. Furthermore, the temporal instability of the samples is incompatible with a meaningful analysis, as it compromises experimental repeatability. Thus, the evaluation of reflectance degradation of a large-size rhodium mirror sample and the subsequent behavior after laser cleaning procedures was not considered of interest within the scope of this study.

5.2.2. B/W contaminants

For the deposition of mixed boron and tungsten coatings, the boron target was modified, as shown in Figure 5.11, by the addition of a tungsten piece with an area of 115 mm^2, covering 0.09% of the ablated area of the target. The shape of the laser spot, left after deposition, is faintly visible on the tungsten piece.

Figure 5.11: Photograph of the boron target with a tungsten piece employed for the production of B/W films. One of the laser spot traces is circled in pink.

All the deposition parameters were kept equal to those used for the deposition of B contaminants, already presented in Section 5.2, with the goal of achieving a coating that differs from the B one only by the presence of a certain atomic percentage of tungsten. The morphology and thickness of the two coatings were intended to be similar to allow for a robust subsequent comparison in terms of laser cleaning performance, ensuring that any differences in the cleaning results are due solely to the different atomic composition of the two coatings, so that information on the different response of these two species to laser cleaning can be assessed.

SEM top-view images of the produced coatings are shown in Figure 5.12 at two different magnifications. In this case as well, a compact, flat morphology with sporadic droplets was achieved, closely resembling the boron morphology presented in Figure 5.5. The cross-section of the B/W film deposited on the Rh sample is shown in Figure 5.13, revealing that the deposition of B and W was uniform, without stratification of the two atomic species, a phenomenon that can occur during co-deposition with mixed targets [106]. SEM analysis was also used to determine the thickness of the coating, which varies between 130 nm and 150 nm on the larger mirror sample shown in Figure 5.14; thus, the presence of tungsten slightly reduced the total deposition rate compared to the pure B film.

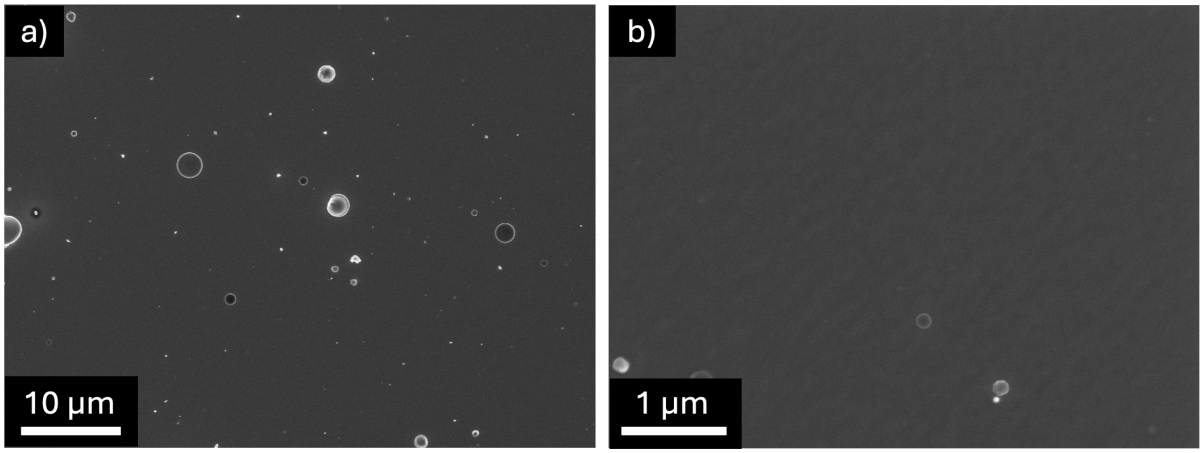

Figure 5.12: SEM top-view images of the B/W coating on the Rh mirror acquired at (a) 5,000× and (b) 50,000× magnification.

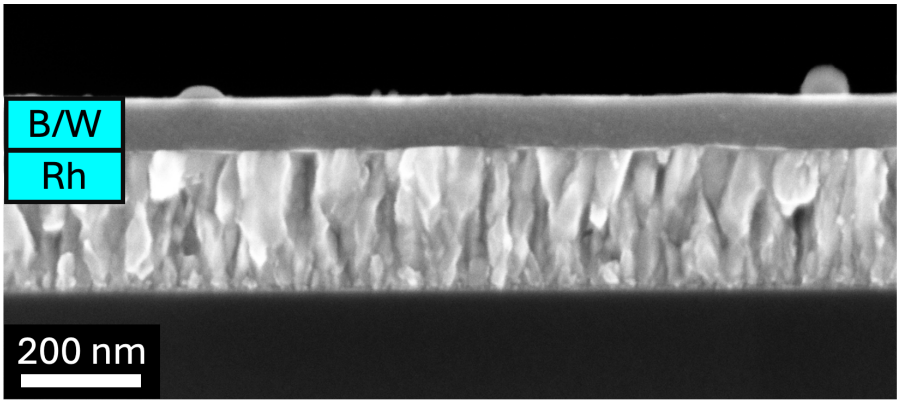

Figure 5.13: SEM cross-section image of the B/W coating on the Rh mirror.

The visual appearance of the Rh mirror contaminated with the B/W coating is presented in Figure 5.14. The presence of tungsten gives the sample a dark appearance, without a dominant color dependent on the thickness of the sample, as was observed in the case of

the boron coating. The reason is that tungsten is a heavy metal that strongly enhances the absorption properties of the coating, reducing the optical skin depth of light inside the layer.

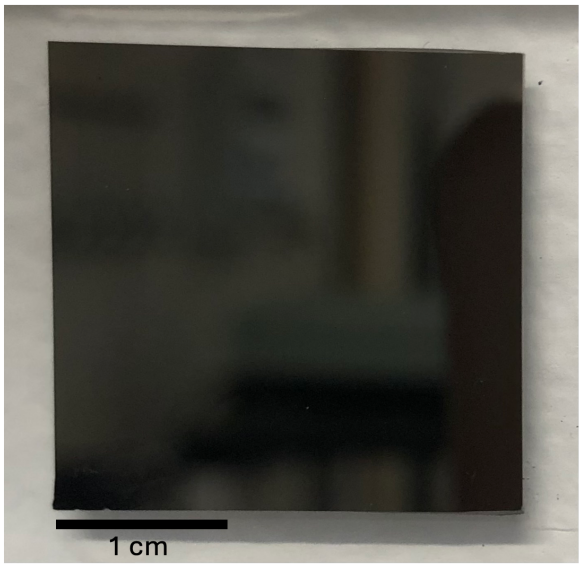

Figure 5.14: Photograph of Rh mirror with the B/W contaminant film.

The atomic composition and mass thickness of the B/W contaminant layer were retrieved through the EDDIE software starting from EDXS data, an example of which is shown in Figure 5.15. Three EDXS spectra were measured at the center of the sample, yielding a mass thickness of 98.85 µg/cm^2, corresponding to a density of 6.59 g/cm^3. These values are much higher than those of the pure B coating due to the presence of W, which has a much higher atomic mass. The atomic composition at the center is 79.67% B, 16.08% W, and 4.24% O.
Three additional EDXS spectra were measured at one of the edges of the sample, from which a mass thickness of 55.25 µg/cm^2 was calculated, corresponding to a density of 4.25 g/cm^3. This lower value compared to the center is attributed to a lower atomic percentage of tungsten (10.7%), together with 83.5% B and 5.8% O.

This gradient in the tungsten atomic concentration originates from the fundamental differences underlying the ablation mechanisms of boron and tungsten under ns-PLD [107]. Indeed, the ablation mechanism of tungsten is purely thermal, generating a highly directional plume oriented mainly along the target normal, with low angular divergence. On the other hand, boron is characterized by lower optical absorption and thermal conductivity; these conditions lead to phase explosion, generating a plume that expands rapidly in all directions, thus resulting in a much broader angular distribution (i.e., less directional

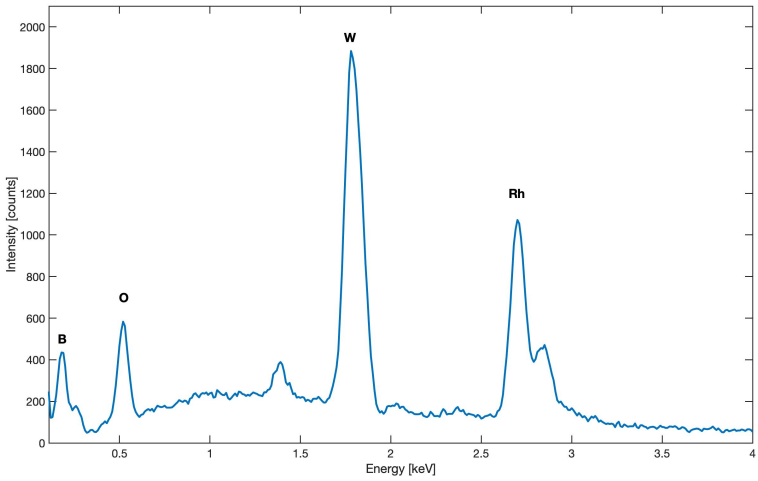

Figure 5.15: EDXS spectrum of the B/W coating on the Rh mirror.

along the axis).

The reflectivity degradation of the Rh mirror (green line) due to the presence of the B/W contaminant film (purple line) is shown in Figure 5.16. In particular, Figure 5.16(a) shows the total reflectance, revealing that the B/W coating reduces the Rh reflectance over the whole spectral range, with values between 30% and 50%. These values are associated with the strong absorption due to the presence of tungsten, which is consistent with the dark appearance of the sample in Figure 5.14. The presence of W also explains the flat reflectance curve over the examined spectral range, with the absence of interference fringes typical of dielectric thin films. The reason behind this behavior is the fact that the strong absorption reduces the optical skin depth of the incident light to a value smaller than the thickness of the coating; this prevents light from reaching the interface between the B/W coating and the Rh mirror and reflecting back to generate the interference pattern that characterized the boron coating.

However, even if lower than that of Rh, the reflectance remains almost entirely specular, as suggested by the low value of the diffuse component (Fig. 5.16(b)) over the whole spectral range. This is consistent with the compact and flat morphology of the produced film, with negligible surface roughness.

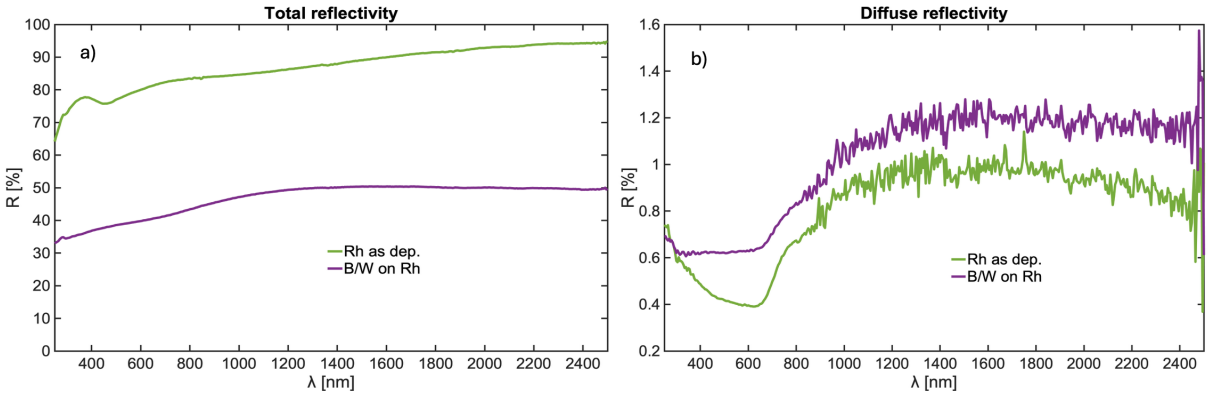

Figure 5.16: Total (a) and diffuse (b) reflectance of the B/W film (purple line) deposited on the Rh sample (green line).

To conclude this chapter, a summary of the mass thicknesses, densities and atomic compositions of the produced samples is provided in Table 5.1.

Table 5.1: Summary of mass thickness, density, and atomic composition of the produced contaminant films retrieved through the EDDIE software starting from EDXS data.

Sample	**Position**	**Mass Thickness** ($\mu g/cm^2$)	**Density** (g/cm^3)	**B** (at. %)	**W** (at. %)	**O** (at. %)
B on Rh	Center	34.97	1.75	85.75	–	14.25
B/W on Rh	Center	98.85	6.59	79.67	16.08	4.24
B/W on Rh	Edge	55.25	4.25	83.50	10.70	5.80

6 | Laser cleaning of contaminated mirror samples

The laser cleaning procedure of the produced samples consisted of four main consecutive steps:

1. **Laser damage threshold**: evaluation of the highest laser fluence that the mirrors can withstand through irradiation of pristine mirrors with different laser wavelengths and pulse energies, to set an upper limit for the selection of laser parameters for the following cleaning steps.
2. **Cleaning trials**: numerous smaller samples were cleaned with the goal of understanding the response of the produced coatings to various laser conditions, by varying parameters such as the incident wavelength, the energy per pulse (thus the fluence, since the laser spot size was kept fixed), the repetition rate, and the laser cleaning speed. The evaluation of the effectiveness of the cleaning procedure on those trial samples was carried out by both visual inspection and SEM evaluation.
3. **Mirror cleaning**: after the selection of the most interesting and efficient cleaning parameters, these were applied to larger samples with the main goal of achieving the best possible reflectivity recovery and evaluating the differences between cleaning with IR and green wavelengths in terms of reflectivity recovery.
4. **Cleaning effectiveness evaluation**: post-cleaning characterization of the samples via reflectance measurements to evaluate the effectiveness of the cleaning process, together with SEM evaluation of the samples to correlate optical properties with sample features such as contaminant residues and possible mirror damage.

As previously described in Section 4.1.2, the laser spot on the samples had a fixed elliptical shape with an area of 47.12 mm^2 (semi-major axis of 5 mm and semi-minor axis of 3 mm), due to the absence of a focusing lens in the laser path.

The motorized target stage was employed in this configuration to move the mirror following a path designed to ensure uniform irradiation to avoid inhomogeneous cleaning of the

mirror surface. This was achieved through vertical laser scans on the mirror, where the spacing between two consecutive laser spots is determined by the laser Repetition Rate (RR) and the mirror translation velocity (v). The relation between the number of pulses on a single point of the mirror (N_p) and the previously mentioned parameters, including the minor spot diameter (d) is:

$$N_\mathrm{p} = \frac{d}{v}\,\mathrm{RR} \tag{6.1}$$

The cleaning of the smaller samples (11×11 mm^2) and the damage trials on pristine samples of the same dimensions were carried out by performing a single scan across the surface, because the major axis of the elliptical spot was large enough to cover the width of the sample.

Conversely, for the cleaning of larger samples, multiple scans were necessary to achieve uniform and complete cleaning. This was essential for the subsequent reflectivity measurements to ensure reliable results. The scanning pattern employed to deliver the same number of laser pulses to each point of the sample was a snake pattern [83], in which multiple vertical scans were performed with a horizontal shift between consecutive passes, ensuring partial overlap, as illustrated in Figure 6.1.

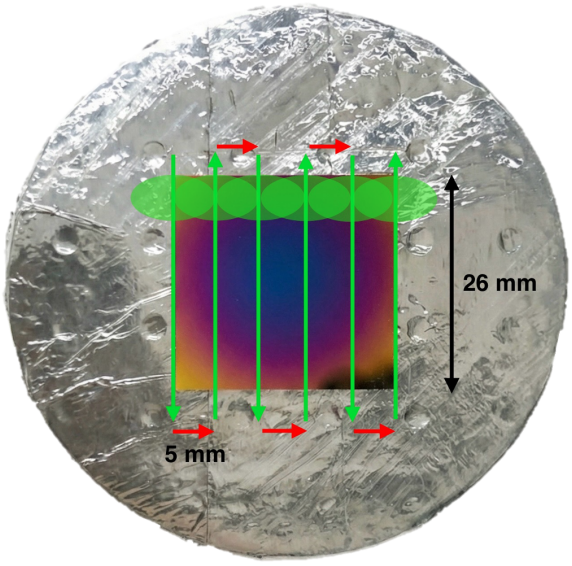

Figure 6.1: Photograph of the B-coated mirror mounted on the holder, illustrating the snake pattern designed for the cleaning procedure.

In Figure 6.1 the vertical direction corresponds to a single scan, where the number of pulses per point is governed by Eq. 6.1, while the horizontal shift between consecutive

scans was set to 5 mm. This value is equal to half of the major axis of the elliptical laser spot, ensuring that each point on the sample is covered by two laser scans performed in opposite vertical directions.

Regarding the background pressure, all cleaning activities were performed in vacuum to reproduce tokamak conditions, as future *in-situ* cleaning procedures in ITER or DEMO will also be carried out in vacuum. Furthermore, performing the cleaning procedure in air would lead to the redeposition of ablated species back onto the mirror. This occurs because the ambient atmospheric pressure spatially confines the expanding plasma plume, increasing collisions and causing the ablated material to scatter backward. Conversely, a vacuum environment allows for the free expansion of the plume away from the surface, ensuring the effective removal of the contaminants.

6.1. Laser damage threshold

The evaluation of the upper fluence limit that could be used for the cleaning strategy was performed via damage tests on uncontaminated Rh samples.

Different samples were irradiated using a laser scan at the green wavelength involving 20 pulses per point on the mirror. Each scan used a different energy, ranging from 300 mJ per pulse to 550 mJ per pulse, thus investigating fluences from about 600 mJ/cm^2 to almost 1100 mJ/cm^2.

All the irradiated samples showed no macroscopic differences upon visual inspection, but SEM analysis revealed mirror damage, mainly consisting of melted areas, starting at fluences of about 850 mJ/cm^2. Examples of damaged mirror areas after laser damage tests are presented in Figure 6.2. Different features can be recognized, including melted areas with dimensions on the order of tens of micrometers (Fig. 6.2(b)) that can modify the flat surface, creating both raised structures (Fig. 6.2(a)) and holes in the film (Fig. 6.2(d)), as well as cracks that follow the shape of the nanocrystalline grains (Fig. 6.2(c)). In Figure 6.2(d), the effect of laser interaction with a Rh droplet, which causes diffraction, is also evident.

For this reason, all subsequent cleaning procedures were performed at lower fluences. In particular, the majority of the cleaning trials were carried out using 20 pulses per point and a laser pulse energy of 350 mJ, corresponding to a fluence of approximately 750 mJ/cm^2. Damage tests on pristine mirrors using these parameters at both 1064 nm and 532 nm wavelengths showed no direct damage to the mirrors. However, the effect of the laser scan is visible in high-magnification SEM images of the nanometer-sized grains, as

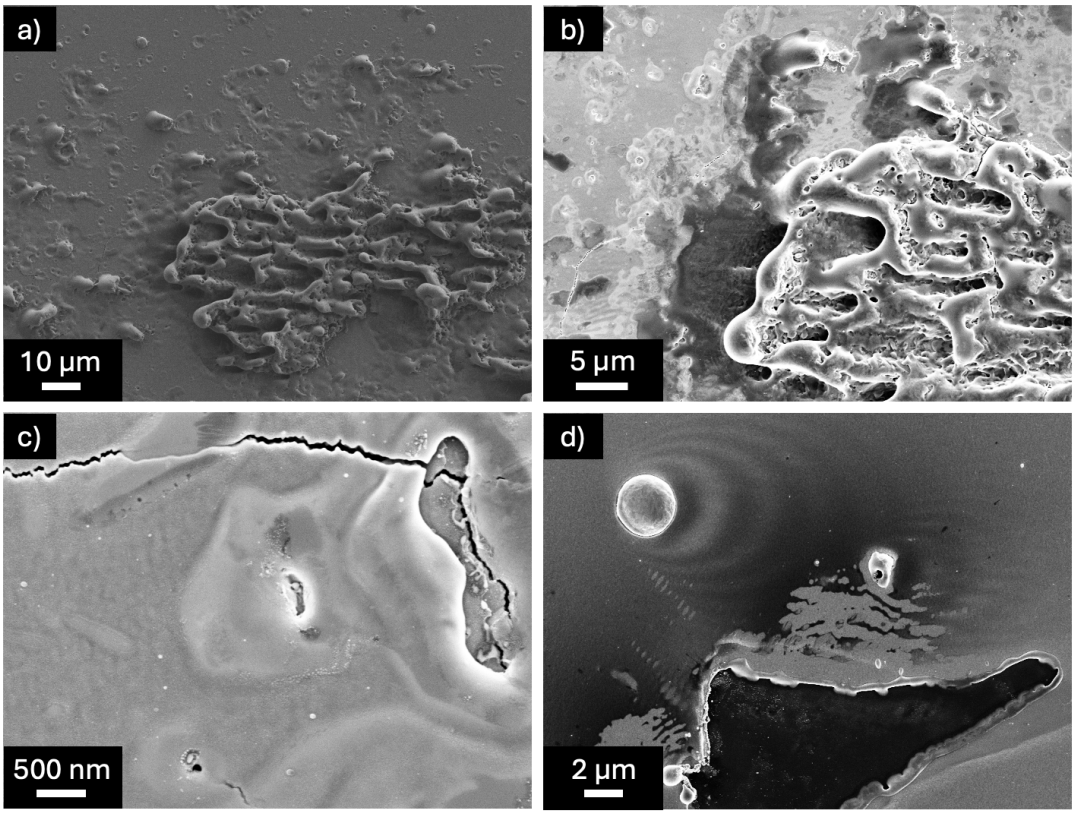

Figure 6.2: Damaged areas after laser tests: melted area imaged with (a) secondary electrons and (b) backscattered electrons; (c) detail of a crack; (d) melted area forming a hole and a nearby droplet that led to laser diffraction during cleaning.

shown in Figure 6.3 (b) and (c), since it leaves nanometric linear marks that were not visible on the non-irradiated samples (Fig. 6.3 (a)).

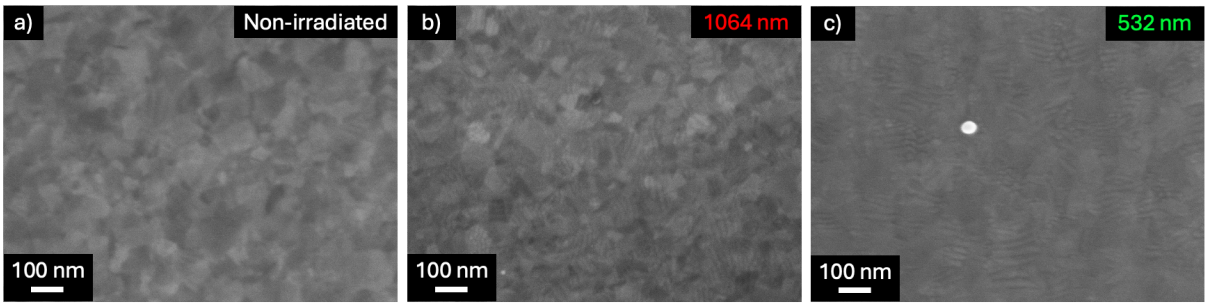

Figure 6.3: Non-irradiated (a) Rh sample. Effects of (b) IR and (c) green laser irradiation on the pristine mirror surface at the nanoscale.

6.2. Cleaning of B coatings

Numerous trial cleaning scans have been performed on smaller samples to identify the optimal cleaning parameters for the larger mirrors and to investigate the interaction mechanisms of the two laser wavelengths with the boron coatings.

Preliminary scans were performed with varying mirror translation velocities and laser repetition rates, leading to the identification of an optimal value of 20 laser shots per point (N_p). This value represents a compromise between two competing requirements. On one hand, a sufficiently high N_p is necessary to ensure high pulse overlap: since the laser beam profile, being an imperfect top-hat, exhibits lower energy at the periphery, insufficient overlap would leave areas irradiated solely by these weak boundaries. By ensuring closely spaced spots, the area affected by edge effects is minimized, guaranteeing a uniform cleaning scan. On the other hand, N_p must be limited because an excessive number of consecutive pulses on a single point is expected to lower the laser damage threshold of the substrate. This reduction would limit the maximum selectable pulse energy, potentially resulting in insufficient energy to effectively remove the contaminant layer. Thus, all experimental scans detailed in the following sections, carried out on both smaller and larger samples, were performed with $N_p = 20$.

The impact of the IR wavelength on the boron coating can be appreciated in Figure 6.4 (a) and (b). In particular, in Figure 6.4 (a), different effects are evident, such as a melted region (white region in the upper half of the picture) containing residues (small black spots), which are compact fragments of the B film that have not been ablated by the laser. However, there are also wide regions in which the coating has been successfully removed and the rhodium grains are visible (darker region in the lower half of the picture).
On the sample in Figure 6.4 (b), the IR scan was performed twice, in perpendicular directions. The overall cleaning outcome does not change significantly compared to a single pass, as compact boron film fragments are still visible. However, the structure of the underlying Rh mirror is almost identical to that of a pristine mirror, meaning that repeating the scan with a delay of a few minutes between the two passes does not have a negative impact in terms of mirror damage.

In contrast, the employment of the green wavelength efficiently removed the boron coating, since the rhodium film structure is completely visible in Figure 6.4 (c). The only residues are micrometer-sized and are present only near the Rh droplets, on the side opposite to the incident laser direction. A detail of this effect is shown in Figure 6.4 (d), where the film residue appears to be the droplet's shadow, meaning that the droplet covered that film area, preventing the laser from reaching it. These residues can be eliminated

using the snake scan pattern designed for larger mirrors, by performing two successive scans from opposite directions of incidence. Overall, the cleaning result with the green wavelength was positive, and the Rh mirror remained undamaged.

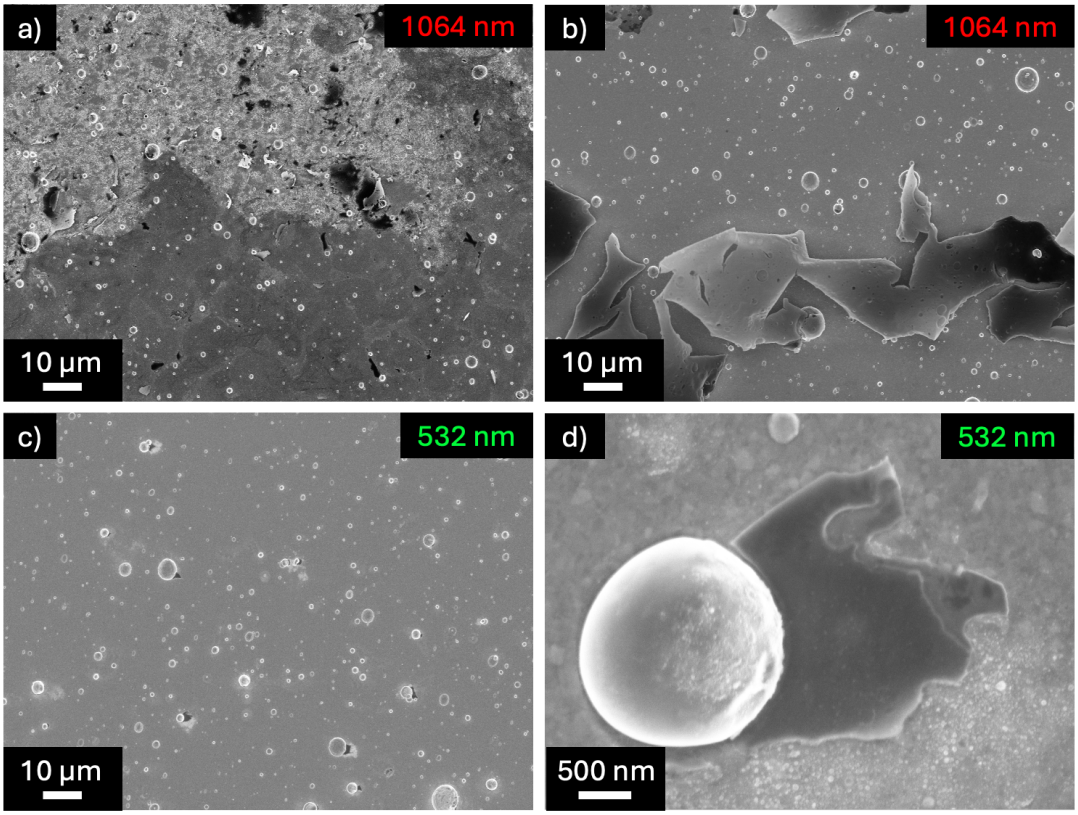

Figure 6.4: SEM images of different trial cleaning samples: (a) and (b) correspond to IR laser scans; (c) corresponds to a scan using the green wavelength; (d) shows a magnified detail of a Rh droplet and the B film residue.

Since the green wavelength successfully removed the coating, a further scan with $\lambda = 532$ nm was performed on the mirror in Figure 6.4 (b). The result was excellent, yielding a cleaned mirror nearly identical to that in Figure 6.4 (c), and confirming that the green wavelength is more effective than the IR wavelength in cleaning this kind of coating.

To evaluate the reflectivity recovery after both the IR and green laser cleaning procedures, two large-size samples were cleaned with multiple scans following the pattern described in Figure 6.1. This resulted in the cleaned mirrors shown in Figure 6.5 (c) and (d), which are presented alongside the pristine mirror (Fig. 6.5 (a)) and the coated mirror (Fig. 6.5 (b)) for comparison.

From a visual inspection, it appears that on the mirror cleaned with IR, there are stripes of opaque residues. These are more evident in the central region of the sample, where the

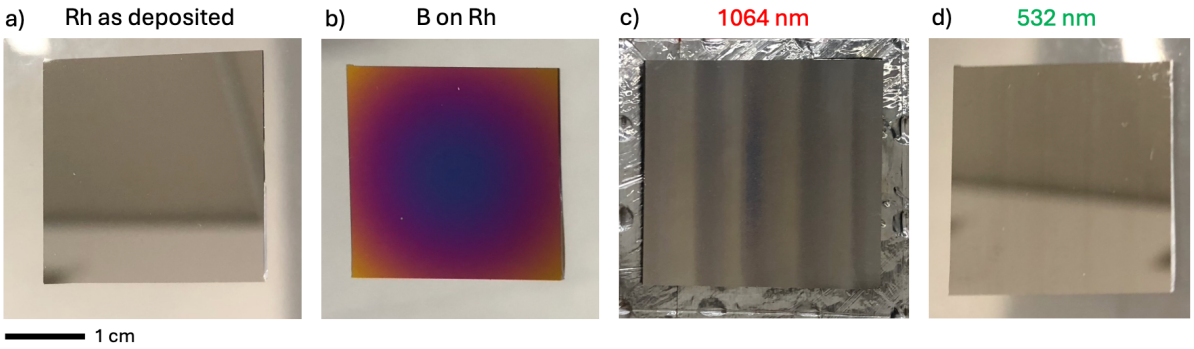

Figure 6.5: Photographs of the mirror samples: (a) as deposited; (b) coated with boron; (c) cleaned with the IR wavelength; and (d) cleaned with the green wavelength.

coating thickness was at its maximum, making it reasonable to assume that removal was more difficult compared to areas where the film was thinner. These residues alternate with stripes in which the reflective rhodium mirror can be seen.
On the mirror cleaned with the green wavelength, vertical stripes indicating the laser scan path are also visible. However, these are much fainter and significantly less visible compared to those on the IR-cleaned mirror, and they do not induce opacity. Overall, the mirror appears successfully cleaned.

Figure 6.6 shows SEM images at different magnifications of the sample mirrors presented in Figure 6.5. In particular, Figures 6.6 (a) and (b) correspond to the opaque regions of the IR-cleaned mirror (Fig. 6.5 (c)). These are characterized by areas where the boron film remained almost intact (the darker regions in the pictures). The presence of these compact film residues is the reason why the opaque stripes on the mirror still show some purple features to the naked eye. Moreover, wide areas with melted residues are visible (the brightest regions with droplets), along with numerous circular spots where the rhodium grains can be seen at the center, surrounded by the cracked B coating (Fig. 6.6 (b)).

Figures 6.6 (c) and (d) show the mirror cleaned with the green wavelength. All the residues are nanoscale melted droplets, and in most regions the underlying Rh grains are visible (Fig. 6.6 (d)). Specifically, Figure 6.6 (c) shows the distribution of the melted residues in a striped pattern. These stripes are compatible with the succession of laser pulses on the mirror, each separated from the previous and next pulse by a few hundreds of micrometers. Thus, this feature can be explained by the fact that the lower energy at the periphery of the laser spot, compared to the energy in the center, is insufficient to fully ablate the contaminant film, but it is high enough to deliver heat and melt the coating. This leads to the production of nanoscale droplets which are much more difficult

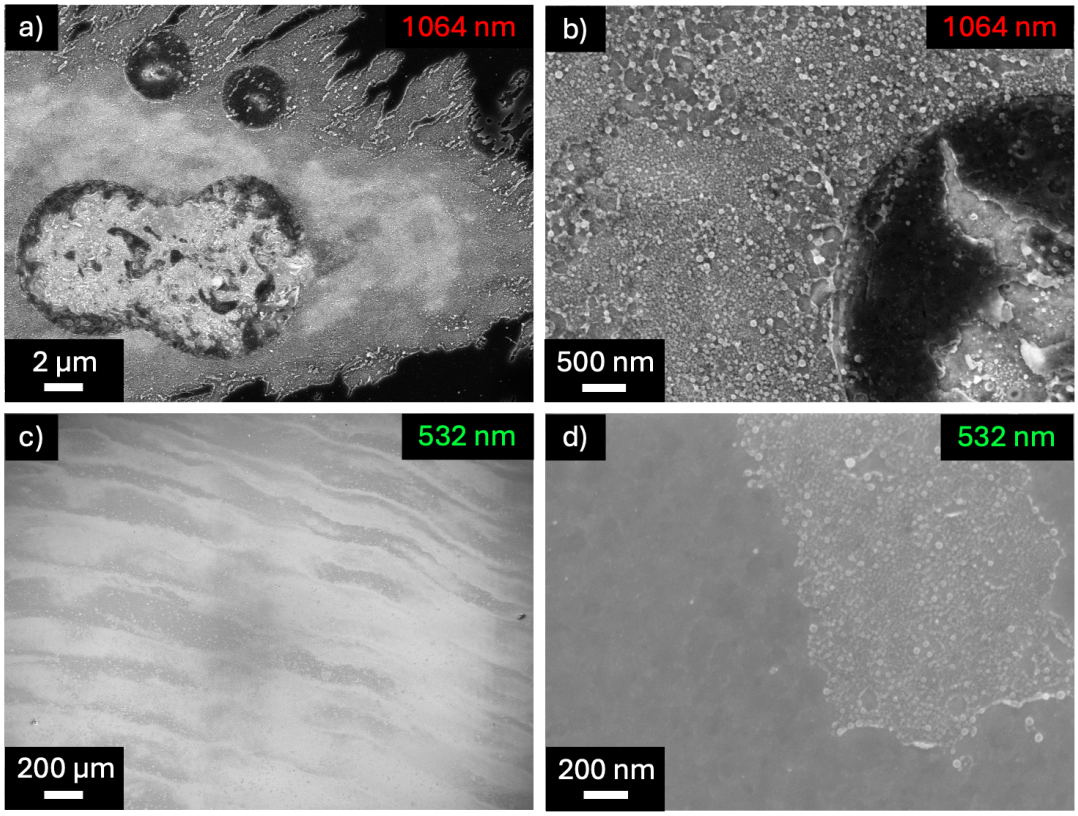

Figure 6.6: SEM images of the boron-coated mirror after cleaning. (a) and (b) show different magnifications of the IR-cleaned mirror; (c) and (d) show the mirror cleaned with the green wavelength.

to remove with subsequent pulses.
The reason why melted droplets were found in this case, while the trial cleaning resulted in a completely cleaned mirror (Fig. 6.4 (c)), can be attributed to the fact that the boron coating on the smaller trial mirrors was approximately 50–70 nm thinner than the coating on the larger mirror, due to the PLD plasma plume geometry. Indeed, it is reasonable to assume that the laser energy was insufficient to completely remove the thicker film; specifically, in the lower layers of the film, thermal diffusion likely only caused melting without complete removal, in contrast to what was observed in the trial cleaning.

6.2.1. Reflectance recovery

The reflectance of both mirrors cleaned with IR and green wavelengths (Fig. 6.5 (c) and (d) respectively) has been measured and presented in Figure 6.7 to evaluate the reflectance recovery compared to the pristine Rh mirror values. Specifically, the specular reflectance of the samples is shown in Figure 6.7 (a) and the diffuse reflectance is shown in Figure

6.7 (b); in both plots the Rh mirror "as deposited" is represented by the blue line, the contaminated mirror is described by the purple line (whose analysis of the reflectance profile has already been presented in Section 5.2.1), and the cleaned mirrors are represented by the red line for the IR cleaning and by the green line for the cleaning with the green wavelength.

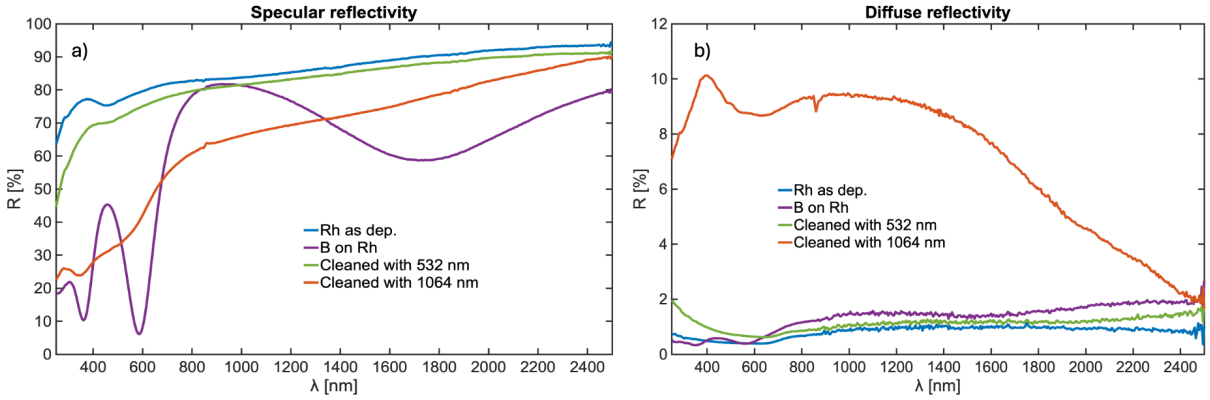

Figure 6.7: Specular (a) and diffuse (b) reflectance of the Rh mirror: as-deposited (blue line), coated with boron (purple line), and cleaned with the IR (red line) and green (green line) wavelengths.

The mirror cleaned with the IR wavelength shows an overall unsatisfactory recovery of specular reflectance. While recovery is better in the IR spectral range, reaching values from 60% to 80%, it remains approximately 10-20 percentage points lower than the Rh values, which stay consistently above 80% in this range. In the visible and UV regions, the specular reflectivity is poor, ranging between 20% and 55%, compared to pristine values higher than 60%. These low specular reflectance values are accompanied by a distinct increase in diffuse reflectance, which is much higher than the values of both the pristine and contaminated mirrors across the entire spectral range, reaching 8%-10% (whereas the as-deposited Rh mirror showed values around 1%). A key factor explaining this tenfold increase in diffuse reflectance can be attributed to the variety of residue types observed via SEM investigation on this sample (Fig. 6.6 (a) and (b)). Indeed, the coexistence of non-ablated film fragments and melted boron droplets over a wide area of the sample is responsible for a significant increase in roughness compared to both the pristine Rh mirror and the contaminated one, since in both latter cases the sample surface was almost completely flat.

The extrapolated value of mean surface roughness for this sample using Bennett's relation (Eq. 3.1) is approximately 35.77 nm, compared to approximately 2.74 nm for the pristine sample. All mean surface roughness values were calculated using the Total Integrated Scattering (TIS) method [108] presented in Appendix A. Moreover, the obtained surface

roughness was considered reliable only in the spectral regions where the exponential fit with Bennett's relation was good, indicating that in the selected spectral region surface roughness is the factor effectively determining light scattering, and consequently the optical properties of the sample. In this particular case, the exponential fit for the Rh pristine mirror worked well in the UV range, while for the cleaned sample the mean roughness was retrieved from the IR range.

In contrast, the mirror sample cleaned with $\lambda = 532$ nm shows good specular reflectance recovery (green line in Fig. 6.7 (a)) over the majority of the spectral range, even though in the UV range the reflectivity value remains further from the pristine value than in the visible and IR regions. This, together with the results obtained with the IR cleaning, suggests that UV reflectance is more difficult to restore compared to that in longer wavelength regions.
The diffuse reflectance (green line in Fig. 6.7 (b)) decreases compared to that of the coated mirror in the IR region, while it increases by a few percentage points in the UV-vis region. This increment in diffuse reflectance in the UV region is consistent with the lower specular reflectance recovery observed in the same range.
This can be explained by the fact that the melted residues left by the cleaning procedure (Fig. 6.6 (d)) are small enough not to induce a significant increase in surface roughness from the point of view of the optical performance in the longer wavelength region. However, the functional dependence of reflectance expressed by Bennett's relation suggests that a roughness increase has a stronger impact on reflectance (increasing the diffuse component and decreasing the specular one) in the shorter wavelength regions, thus explaining the greater difficulty in restoring specular reflectivity in the UV region as well as the slight increase in diffuse reflectance.
In this case, the surface roughness value was derived entirely from the UV region, which is the spectral region where the exponential fit was optimal, consistent with the fact that nanometer-sized residues effectively scatter short-wavelength light. The obtained surface roughness value is 3.93 nm, very close to the 2.74 nm of the pristine Rh mirror.

Overall, the specular reflectance of the cleaned mirror exceeds 50% over the entire spectral range, and exceeds 70% if only the visible and IR spectral regions are considered. The diffuse reflectance values also remain optimal across the whole spectrum, since they never exceed 2%. Thus, the melted residues have a small impact only on the diffuse reflectance in the UV range, meaning that their dimensions and spatial distribution do not dramatically affect the optical performance of the cleaned mirror.

The significant difference in the cleaning efficacy between the two wavelengths, considering the fact that the fluence on the mirror and the number of pulses on each point on the

sample were the same for both cleaning procedures, could be explained by the interference pattern of the boron coating (purple line in Figure 6.7). Indeed, the green wavelength ($\lambda = 532$ nm) is particularly close to an interference minimum of the pattern, since it corresponds to a total reflectivity value of about 25%, meaning that this wavelength is effectively absorbed by the coating film. On the other hand, the IR laser wavelength ($\lambda = 1064$ nm) approaches an interference maximum and corresponds to a total reflectivity value of 81%, thus leading to a much less effective absorption of the energy delivered by the laser to fully ablate the film.

6.3. Cleaning of B/W coatings

The cleaning scans on the mirrors contaminated with the B/W coatings presented in Section 5.2.2 were performed using the same cleaning parameters chosen for the B coating: a laser energy per pulse of 350 mJ, corresponding to a fluence of approximately 750 mJ/cm^2, and 20 pulses per sample point. The decision to maintain the same laser parameters was made to investigate the role of tungsten in the laser cleaning response of the boron coating; therefore, to ensure a valid comparison, all other conditions were kept unchanged from the previously described cleaning procedures for the B coating.

The trial cleaning was conducted using the green wavelength on one of the smaller samples, as it was expected to perform better than the IR one, resulting in a mirror that appeared clean upon visual inspection. However, SEM characterization (Figure 6.8) revealed a surface almost entirely covered by nanoscale residues resulting from the melting of the coating, indicating that the contaminated layer was not fully ablated. The layer of melted droplets (Fig. 6.8 (b)) is interspersed with regions where the film appears to have been ablated and the rhodium grains are visible.

Figure 6.8 (a) shows a detail of the interaction between the laser pulse and the droplets. The presence of a microscale obstacle, such as a droplet produced by the film deposition process, causes a diffraction phenomenon, since the dimensions of the droplets are of the same order of magnitude as the laser wavelength. The result of this diffraction is a wave-like pattern on the side of the droplet opposite to the direction of laser incidence. Specifically, starting from the left, one can observe half of the droplet acting as the source of diffraction, followed by a darker region representing an intact part of the B/W coating located in the geometric shadow where the laser could not reach. Beyond this shadow, an alternating pattern of lighter and darker curved stripes appears: the lighter stripes correspond to regions of lower laser intensity (diffraction minima) with a higher concentration of melted droplets, while the darker curves correspond to areas of higher

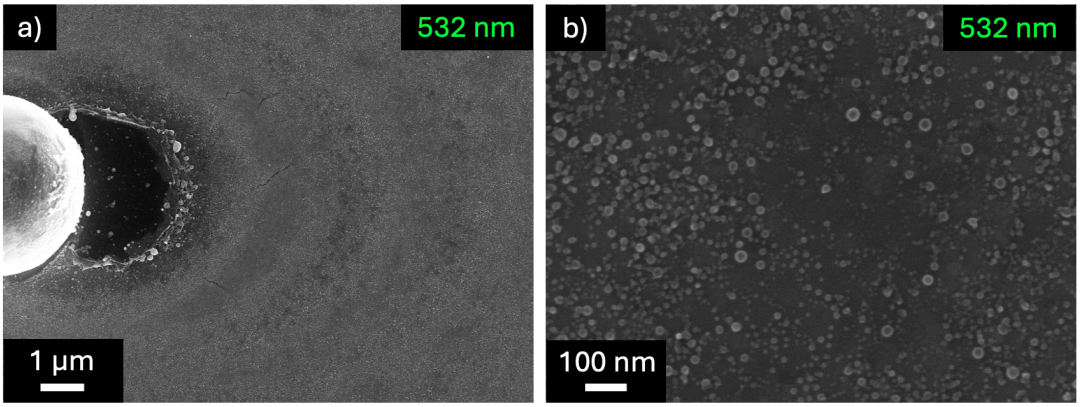

Figure 6.8: SEM images of a trial cleaning scan with $\lambda = 532$ nm: (a) diffraction pattern due to laser-droplet interaction, (b) detail of the layer of melted residues.

laser intensity (diffraction maxima) sufficient to fully ablate the film and, in some points, even cause cracking of the underlying rhodium mirror.

In this case as well, to evaluate reflectivity recovery as a function of the cleaning wavelength, it was necessary to clean two large-size mirrors using the superimposed scan pattern shown in Figure 6.1. Photographs of the mirrors cleaned with the IR and green wavelengths are presented in Figure 6.9 (c) and (d) respectively, while Figure 6.9 (a) and (b) show the pristine and contaminated mirrors for comparison.

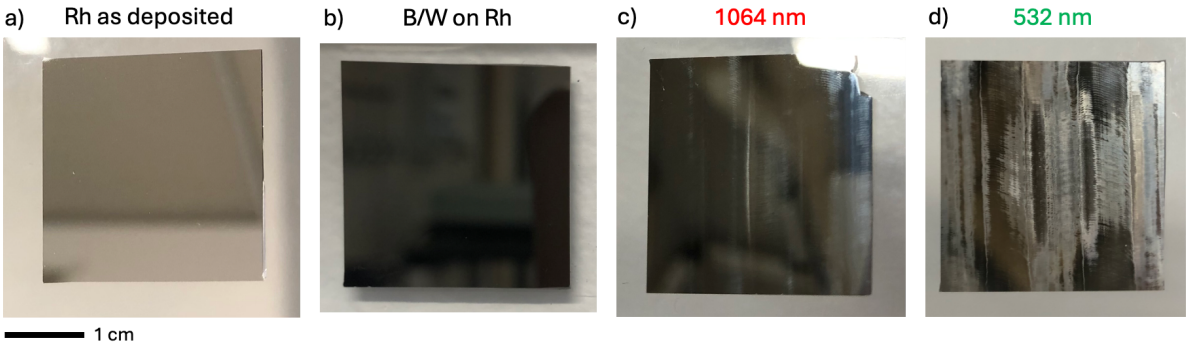

Figure 6.9: Photographs of the mirror samples: (a) as deposited; (b) coated with mixed B/W; (c) cleaned with the IR wavelength; and (d) cleaned with the green wavelength.

From a visual inspection, the mirror cleaned with the IR wavelength (Fig. 6.9 (c)) appears to be mostly cleaned, despite the presence of vertical lines that clearly represent the boundaries of the cleaning scans. The fact that these are visible, despite the region corresponding to the lateral boundary of a cleaning scan being also covered by the center of the laser spot in the subsequent scan, further indicates that the periphery of the laser spot induces morphology modifications on the coating that prevent complete ablation.

Furthermore, the shape of consecutive laser spots in a single scan is also visible to the naked eye for the same reason discussed above.

The mirror cleaned with the green wavelength (Fig. 6.9 (d)) clearly show a bad performance of the cleaning procedure, the laser scans are clearly visible both in the vertical direction and with the evidence of the boundaries of the single spots. Overall the optical performance is damaged and SEM characterization described in the following is aimed in understanding the reason.

In both mirrors, the central region proved to be the most difficult to clean, as evidenced by the presence of opaque areas. Specifically, a vertical line is evident in the IR-cleaned mirror, while the central region of the green-cleaned one is affected by opaque stripes. This result can be attributed to the fact that the film in the central region is thicker than in the peripheral parts of the sample, and the atomic percentage of tungsten is also higher, as presented in Table 5.1. Collectively, these conditions made the film in the central region more difficult to ablate compared to the other regions.

Figure 6.10 shows two SEM images of the mirror cleaned with the IR wavelength. Most of the sample area appears clean, as shown in Figure 6.10 (a), where rhodium grains are intact, although some melted residues are present. However, there are also regions reaching dimensions of tens of micrometers, as shown in Figure 6.10 (b), where the Rh mirror appears cracked and melted. This is an undesirable feature suggesting the need to employ a lower laser fluence to mitigate this damage, provided that such lower fluence would still be sufficient to ablate the film, given that residues are observed even at the current fluence levels.

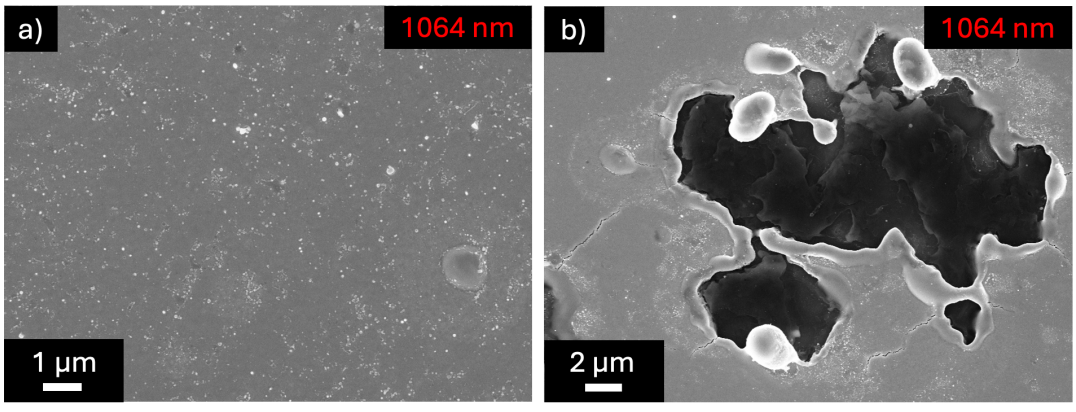

Figure 6.10: SEM images of the B/W coated mirror after cleaning with the IR wavelength: (a) cleaned area with some droplet residues from the melted film; (b) region where the Rh mirror has melted.

The results of the SEM post-cleaning analysis of the mirror cleaned with the green wavelength are shown in Figure 6.11. The images were acquired from different regions of the sample and illustrate the various features and modifications induced by the laser-coating interaction.

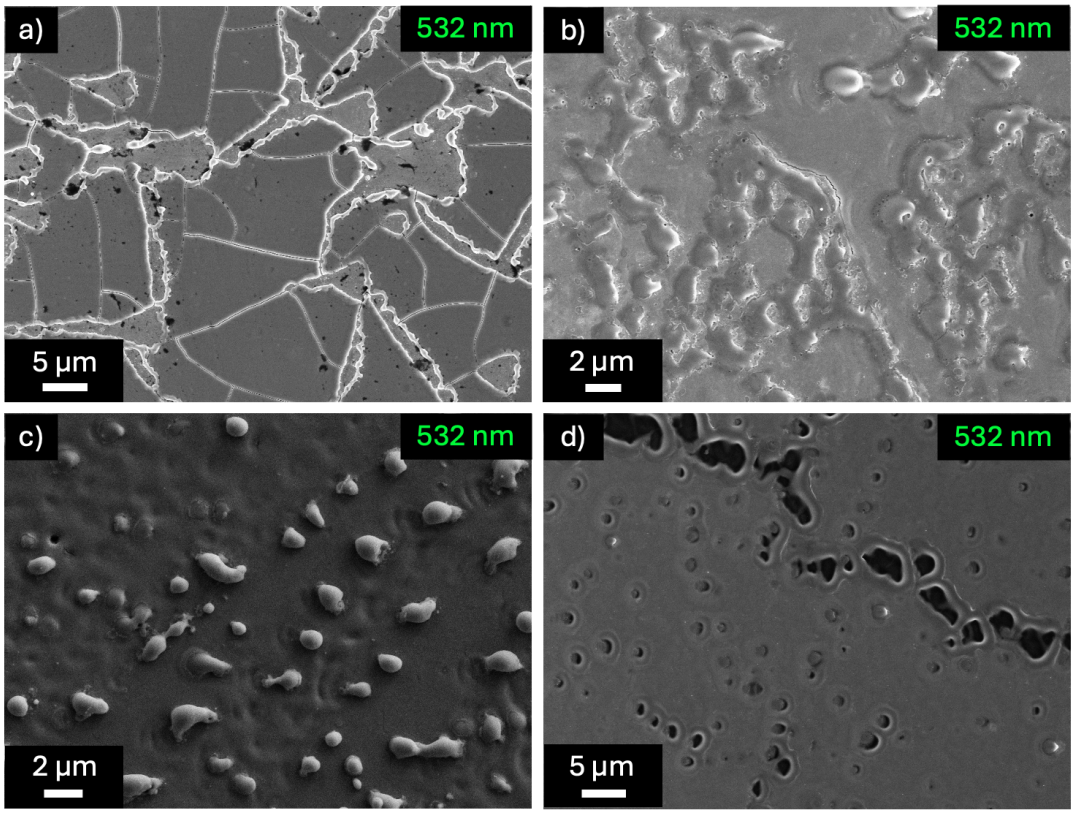

Figure 6.11: SEM images of the B/W coated mirror after cleaning with the green wavelength: (a) cracked coating fragments; (b) larger melted residues; (c) smaller melted residues imaged with secondary electrons, highlighting the increased roughness; (d) melted underlying rhodium mirror.

In the central region of the sample, the opaque stripes consist of large micrometer-sized fragments of film, shown in Figure 6.11 (a), which appear to be merely cracked rather than ablated. Moving away from the center, wide areas in which the B/W coating appears melted are visible (Fig. 6.11 (b)); the melted residues become smaller and more sparse in the peripheral areas (Fig. 6.11 (c)), yet remain large enough to significantly increase roughness compared to the pristine mirror.
The regions in which no film residues are found are still characterized by micrometer-sized regions where the Rh mirror has melted, as shown in Figure 6.11 (d). The aligned morphology of the holes left by the melted rhodium suggests that the origin of this damage is the incidence of multiple laser shots on the same point. Indeed, if the interaction of the

sample with a single shot induces elongated cracks in the mirror, which usually follow the shape of the nanocrystalline Rh grains (Fig. 6.2 (c)), subsequent shots can deliver the necessary heat to induce melting starting from the previously produced cracks, resulting in the melted morphology shown in Figure 6.11 (d).

Once again, the superior performance of laser cleaning with the green wavelength on the trial mirror (Fig. 6.8), compared to the result obtained on the larger mirror (Fig. 6.11), can be attributed to the reduced thickness of the contaminant film on the smaller mirror (approximately 50 nm) compared to the center of the larger one.

Thus, from the analysis of the mirror conditions after cleaning, information regarding the interaction between the laser and the contaminants can be inferred.
The presence of tungsten strongly modifies the absorption of laser energy by the coating. In particular, the mixed B/W film proves to be more difficult to ablate compared to the coating containing only boron. Furthermore, the different atomic concentrations of tungsten have an impact on light absorption: a lower tungsten atomic concentration leads to the melting of the coating and the persistence of residual droplets, together with heat diffusion that transfers heat to the underlying mirror, causing its melting. Conversely, the higher atomic percentage of tungsten in the central region of the sample causes laser-induced thermal stresses to prevail over thermal ablation.
Another important result is the fact that the interaction at the interface between the coating and the underlying mirror lowers the laser damage threshold of the mirror itself, since the mirror irradiated under the same conditions did not exhibit cracks or melted regions similar to those in Figure 6.10 (b) and Figure 6.11 (d). Such a reduction in the laser ablation threshold has previously been observed in other laser cleaning tests, although on beryllium-containing coatings rather than boron [109].

6.3.1. Reflectance recovery

Figure 6.12 presents a comparison of the measured reflectances of the B/W contaminated mirrors (Fig. 6.9 (b)), the mirrors subsequently cleaned with IR and green wavelengths (Fig. 6.9 (c) and (d), respectively), and the pristine Rh mirror (Fig. 6.9 (a)). In both plots, the pristine Rh mirror is represented by the blue line and the contaminated mirror by the purple line, while the red and green lines correspond to the reflectance of the mirrors cleaned with the IR and green wavelengths, respectively. Specifically, the specular reflectance, for which complete recovery is desirable, is shown in Figure 6.12 (a), while the diffuse component, is presented in Figure 6.12 (b).

The IR-cleaned mirror showed a moderate reflectivity recovery in the IR spectral region,

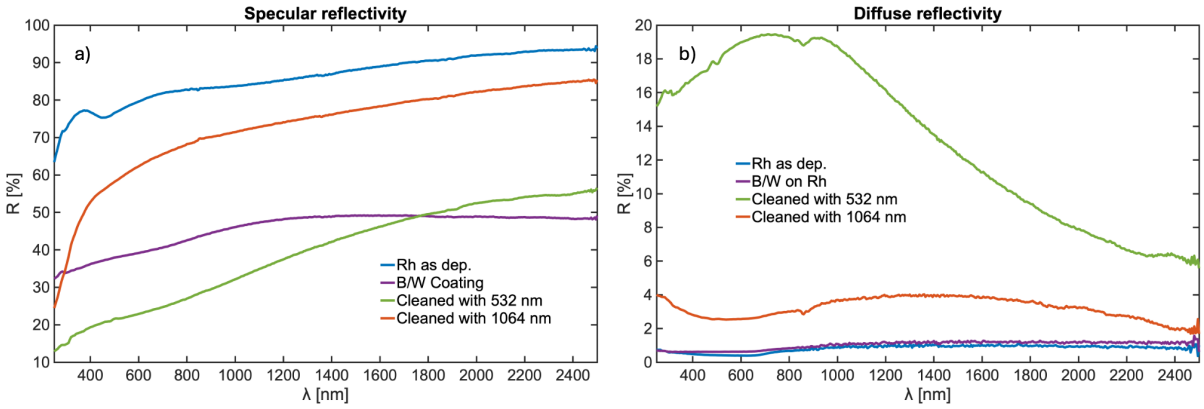

Figure 6.12: Specular (a) and diffuse (b) reflectance of the Rh mirror: as-deposited (blue line), coated with mixed boron and tungsten (purple line), and cleaned with the IR (red line) and green (green line) wavelengths.

reaching reflectance values between 70% and 85%, which remain consistently about 10 percentage points lower than those of the pristine Rh sample. In contrast, the reflectance values in the visible and UV ranges remain lower, between 65% and 25%. This confirms (as already noted during the analysis of reflectance spectra of the boron-coated and subsequently cleaned mirrors) that reflectivity recovery in the shorter wavelength range is more difficult due to the presence of nanometer-sized melted residues. These residues induce surface roughness that scatters short-wavelength incident light in random directions.
This is consistent with the diffuse reflectivity plot, in which the red line indicates a diffuse reflectance of about 3–4% across the entire spectral range, compared to a value of around 1% for both the pristine and contaminated mirrors.
Calculated from the diffuse reflectance value in the UV range, a mean surface roughness of about 7.83 nm was obtained, which is more than twice the Rh mirror value of 2.74 nm. The fact that the exponential fit using the Total Integrated Scattering (TIS) model was accurate in the UV region is consistent with the hypothesis that, in this spectral region, surface roughness is indeed the dominant cause of light scattering.

On the other hand, the mirror cleaned with the green wavelength showed a specular reflectance (green line in Figure 6.12 (a)) which is even lower than that of the contaminated mirror (purple line) over almost the whole spectral range, meaning that the mirror's optical properties were damaged rather than restored after the cleaning procedure. Consistently, the diffuse reflectance (green line in Figure 6.12 (b)) is much higher, reaching values up to 19%, which is an increment of almost 20 times the pristine mirror value.
The exponential fit of the diffuse reflectance in the IR spectral region yielded a mean surface roughness of almost 54.8 nm, which is a significantly larger value compared to the

few nanometers of both the "as deposited" Rh mirror and the contaminated one.

The reflectance properties of this sample can be attributed to the wide variety of residues present. Specifically, the melted residues (Fig. 6.11 (b) and (c)), the intact film fragments (Fig. 6.11 (a)), and the melted rhodium areas (Fig. 6.11 (d)) all possess dimensions on the order of micrometers. Consequently, these features significantly increase the surface roughness and induce effective scattering even at longer incident wavelengths.

The lack of a significantly superior performance of the green wavelength compared to the IR one for this type of coating can be attributed to the fact that the presence of even a small amount of tungsten drastically altered the optical properties, giving the film a metallic behavior rather than a dielectric one. Consequently, the interference pattern, which in the pure boron coating enhanced the absorption at $\lambda = 532$ nm and inhibited the absorption at $\lambda = 1064$ nm, was completely suppressed.

In the case of the B/W coating, the more effective performance of the IR wavelength can be attributed to the significantly lower total reflectance (approximately 48%) compared to the boron coating, which exhibited a total reflectance of nearly 81% at $\lambda = 1064$ nm.

Conversely, the poor performance of the green wavelength should not be attributed to a difference in the total reflectance of the two coatings at $\lambda = 532$ nm, even though it is slightly higher for the B/W coating (39%) compared to the B coating (25%). This conclusion is supported by the fact that absorption at this wavelength was effective on the trial sample (Fig. 6.8), where the contaminant layer was removed much more effectively than on the larger sample (Fig. 6.11), and no melted Rh mirror areas were found. Therefore, it is more plausible to attribute the unsuccessful cleaning to the excessive thickness of the film to be ablated and to an excessively high tungsten atomic percentage.

7 | Conclusions and future developments

During the operation of tokamak machines, presented in Chapter 1, Plasma-Wall Interaction (PWI) induces the erosion of materials constituting the First Wall (FW) and the subsequent migration and redeposition of eroded species in places different from the original ones, as discussed in Chapter 2. The impact of material redeposition is particularly detrimental to First Mirrors (FMs), which are crucial components of optical diagnostics; their optical properties (mainly the high specular reflectivity) are affected by redeposited contaminants composed of FW material species. Thus, the development of an efficient cleaning procedure that effectively removes the contaminant layer from the first mirrors is desirable to avoid the frequent and expensive replacement of those components.

In recent years, the ITER Organization revised the choice of First Wall materials, transitioning from a First Wall composed of beryllium and tungsten to a full-tungsten First Wall, with boronization as a wall conditioning technique. This recent decision required an update of the studies conducted over the last two decades on the cleaning of First Mirror samples and real mirrors retrieved after tokamak exposure from contaminants based on carbon and beryllium, presented in Chapter 3. Thus, it is essential to investigate the performance of cleaning procedures on mirrors contaminated with layers that are more representative of the atomic composition of the future First Wall.

This work aimed at the laboratory-scale production of samples of nanocrystalline rhodium, which is one of the most studied mirror materials for fusion applications, and the subsequent deposition of tokamak-relevant contaminants on the mirror samples. Both the production of mirror samples and the contamination with boron and mixed boron-tungsten deposits were carried out via the nanosecond Pulsed Laser Deposition (PLD) technique described in Chapter 4. The characterization of the samples, presented in Chapter 5, was performed through SEM and EDXS analysis, complemented with spectrophotometric measurements to evaluate the reflectance of the samples.

The same PLD setup was employed for the laser cleaning of the contaminated mirrors, as

the second main objective of this thesis was to test the efficacy of laser cleaning by evaluating the differences between the employment of an IR wavelength ($\lambda = 1064$ nm) and a green wavelength ($\lambda = 532$ nm) on both types of contaminants. The comparison, reported in Chapter 6, was carried out in terms of reflectance recovery and laser-induced damage, correlating the optical properties of the cleaned mirrors with their surface morphology after cleaning.

7.1. Overview of the main results

The ns-PLD technique revealed its efficacy in the production of both highly oriented nanocrystalline rhodium mirrors and compact boron contaminant layers, as well as novel mixed boron-tungsten compact contaminants. However, it proved to be unsuitable for producing porous boron coatings.

The analysis of the produced samples revealed the dielectric behavior of the boron coating, expressed via a clear interference pattern in the reflectance. On the other hand, the presence of tungsten, even in reduced atomic percentage (10-16%) compared to boron, drastically changed the optical behaviour of the coating, leading to a coating which is metallic, without an interference pattern, and more absorbing than the rhodium mirror.

Then, both the B and the B/W coated mirrors have been cleaned with superimposed laser scans performed with the same cleaning parameters, leading to a fluence per pulse on the sample of approximately 750 mJ/cm^2. On both the samples, both the IR and the green laser wavelengths have been exploited and the cleaning effectiveness was compared.

In general, for both the contaminant coatings, the cleaning performance was shown to be better on trial cleaning samples than on larger samples, which were characterized by a higher contaminant layer thickness, suggesting that the cleaning procedure should be performed before the redeposit thickness exceeds a thickness of about 100 nm to ensure the best cleaning performance.
A key finding common to all the performed cleanings is that the initial laser-coating interaction determines the overall cleaning performance: if the energy of the first laser pulse is insufficient to fully ablate the film, the resulting melted residues become significantly harder to remove with subsequent shots. This behavior could be attributed to a laser-induced phase change: the melting and subsequent resolidification process transforms the initially deposited layer into a structure possessing a significantly higher ablation threshold.

Regarding the boron coating, the green wavelength proved to be much more effective in

the cleaning, leaving on the sample only some nanometric droplets, while the IR cleaning left residues on large areas, consisting of both melted residues and pieces of non-ablated film which significantly increase the diffuse reflectance. A possible explanation for the superior performance of the green wavelength compared to the IR one on this coating is the fact that the former ($\lambda = 532$ nm) corresponded to a reflectance minimum ($R_{\text{tot}} \approx 25\%$) of the boron coating interference pattern, maximizing absorption. On the contrary, $\lambda = 1064$ nm corresponds to an interference maximum ($R_{\text{tot}} \approx 81\%$) which minimizes light absorption.
From the point of view of reflectance recovery, the cleaning with the green wavelength induced a good reflectance recovery (almost 90%) over the vis-NIR spectral range. The UV reflectivity recovery proved to be more difficult because, despite the visually clean appearance of the sample, the nanometric residual droplets enhance the superficial roughness sufficiently to effectively scatter short-wavelength light.

The mixed boron-tungsten coatings proved to be much more difficult to ablate without melting and heat transfer to the underlying mirror, since the metallic behavior of the coating strongly modified its light absorption properties.

From the comparison between the two wavelengths in this case, it is more difficult to determine which one gave the better cleaning performance. The green wavelength gave good results during the trial cleaning, even though nanometric melted residues were still found, but the cleaning on the larger sample gave a very unsatisfactory result due to non-ablated film parts, melted film parts, and melting of the mirror. This could be attributed to the excessive thickness of the coating and to a tungsten percentage too high to allow for good ablation.
The IR wavelength gave better results both compared to the green wavelength on the larger B/W coated sample and compared to the result of the IR cleaning on the boron coating. Still, the cleaning result is imperfect and shows melted residues mostly in the central region of the sample, where the film was thicker.
Overall, a completely satisfactory cleaning procedure has not been found in the case of the mixed boron-tungsten coating, and the responsibility is to be attributed to the presence of tungsten.

Another general result is the fact that the presence of a contaminant layer reduces the ablation threshold evaluated on the pristine mirror. The presence of tungsten further enhances this situation, thus limiting the fluence selectable for cleaning. The interaction between the laser and the contaminant layer can melt the rhodium mirror even if the contaminant layer is not fully removed.

7.2. Concluding remarks and future perspectives

In conclusion, it is worth noting that with a single PLD setup, it has been possible to carry out a complete work comprising the production of mirror samples, contamination with two different types of contaminants, and the laser cleaning of those samples. In addition, SEM, EDXS results, and also spectrophotometric measurements gave important and coherent information on the samples during all the steps of this work.

In particular, this laboratory-scale work proposed the use of a well-known technique such as laser cleaning to evaluate its performance on coatings containing a material like boron, whose response to laser cleaning has never been studied in the framework of fusion diagnostics First Mirror studies.

Future developments starting from the results of this study suggest the need to improve the cleaning procedure, especially from an efficacy point of view with the goal of maximizing the reflectance recovery.
Regarding boron coatings, the investigation of different thicknesses of the layer would be useful to better understand the absorption properties of the coating as a function of the interference peak positions. Furthermore, the investigation of the cleaning efficacy on thinner layers, specifically below 100 nm, could give better results for the complete recovery of the reflectance also in the UV range.
The study of the mixed boron coatings requires the selection of a lower laser fluence, in order to avoid exceeding the reduced laser damage threshold induced by the coating-mirror interaction. This would also imply the study of B/W coatings thinner than those produced in this study, since it is highly unlikely that current coating thicknesses can be effectively cleaned using a laser fluence lower than the one that already proved insufficient. Even in this case, film thicknesses below 100 nm could be of interest to investigate. Given the metallic nature of the tungsten-containing coating, the employment of a UV laser wavelength could also lead to better cleaning results, since UV wavelengths are in general better absorbed by metallic coatings.

Moreover, the investigation of coating morphologies different from the compact ones could be carried out by employing the fs-PLD setup rather than the ns-PLD one. In this way, the direct emission of nanoparticles could facilitate achieving the desired porous morphology.

Finally, it is necessary to analyze the effect of repetitive cleaning cycles on the mirrors; indeed, the mirrors must be able to withstand not only a cleaning procedure, but numerous cycles of contamination and cleaning.

Bibliography

[1] International Energy Agency (IEA). Year-on-year growth rate in global electricity demand, 1991–2025, 2024. URL https://www.iea.org/data-and-statistics/charts/year-on-year-growth-rate-in-global-electricity-demand-1991-2025. Licence: CC BY 4.0.

[2] H Ritchie, M Roser, and P Rosado. Electricity production by source, 2024. URL https://ourworldindata.org/grapher/electricity-prod-source-stacked. Data adapted from Ember and Energy Institute (2025).

[3] International Energy Agency. Global energy review 2025, 2025.

[4] IPCC Wmo. Climate change: the 1990 and 1992 ipcc assessments, ipcc first assessment report overview and policymaker summaries and 1992 ippc supplement, 1992.

[5] United Nations. Causes and effects of climate change. *United Nations*, 2024.

[6] Gautam Gowrisankaran, Stanley S Reynolds, and Mario Samano. Intermittency and the value of renewable energy. *Journal of Political Economy*, 124(4):1187–1234, 2016.

[7] Héctor Quiroga-Barriga, Fabricio Nápoles-Rivera, César Ramírez-Márquez, and José María Ponce-Ortega. Nuclear energy as a strategic resource: A historical and technological review. *Processes*, 13(8):2654, 2025.

[8] Truman P Kohman. Proposed new word: nuclide. *American Journal of Physics*, 15 (4):356–357, 1947.

[9] Ettore Fiorini. Nuclear energy and anthropocene. *Rendiconti Lincei*, 25, 03 2014. doi: 10.1007/s12210-013-0247-z.

[10] EE Salpeter. Nuclear reactions in the stars. i. proton-proton chain. *Physical review*, 88(3):547, 1952.

[11] Juris Meija, Tyler B Coplen, Michael Berglund, Willi A Brand, Paul De Bièvre, Manfred Gröning, Norman E Holden, Johanna Irrgeher, Robert D Loss, Thomas Walczyk, et al. Isotopic compositions of the elements 2013 (iupac technical report). *Pure and Applied Chemistry*, 88(3):293–306, 2016.

[12] L. Coraggio, A. Covello, A. Gargano, N. Itaco, T. T. S. Kuo, and R. Machleidt. Nuclear structure calculations and modern nucleon-nucleon potentials. *Physical Review C*, 71(1), January 2005. ISSN 1089-490X. doi: 10.1103/physrevc.71.014307. URL `http://dx.doi.org/10.1103/PhysRevC.71.014307`.

[13] David Moiraf. *The use of Plasma Mirror for Relativistic Electron Generation Relevant to Fast Ignition in Inertial Confinement Fusion*. PhD thesis, 07 2020.

[14] Jef Ongena. Fusion: A true challenge for an enormous reward. In *EPJ Web of Conferences*, volume 98, page 05004. EDP Sciences, 2015.

[15] Silvano Tosti and Alfonso Pozio. Membrane processes for the nuclear fusion fuel cycle. *Membranes*, 8:96, 10 2018. doi: 10.3390/membranes8040096.

[16] SI Braginskii. Transport processes in a plasma. *Reviews of plasma physics*, 1:205, 1965.

[17] MJ Singh. Status of heating and current drive systems planned for iter. *IEEE Transactions on Plasma Science*, 44(9):1514–1524, 2016.

[18] J Abdallah, REH Clark, and N Putvinskaya. Calculations of energy losses due to atomic processes in tokamaks with applications to the international thermonuclear experimental reactor divertor. *Physics of Plasmas*, 2(6):2328–2336, 1995.

[19] Samuel E Wurzel and Scott C Hsu. Progress toward fusion energy breakeven and gain as measured against the lawson criterion. *Physics of Plasmas*, 29(6), 2022.

[20] John D Lawson. Some criteria for a power producing thermonuclear reactor. *Proceedings of the physical society. Section B*, 70(1):6, 1957.

[21] Stefano Atzeni and Jürgen Meyer-ter Vehn. *The Physics of Inertial Fusion: Beam-Plasma Interaction, Hydrodynamics, Hot Dense Matter*. Number 125. Oxford University Press, 2004.

[22] Lawrence Livermore National Laboratory. Achieving fusion ignition. National Ignition Facility & Photon Science website. URL `https://lasers.llnl.gov/science/achieving-fusion-ignition`. Accessed: 2026-01-10.

[23] Weston M Stacey. *Fusion: An introduction to the physics and technology of magnetic confinement fusion*. John Wiley & Sons, 2010.

[24] Samuel E Wurzel and Scott C Hsu. Continuing progress toward fusion energy breakeven and gain as measured against the lawson criteria. *Physics of Plasmas*, 32 (11), 2025.

[25] John R Cary and Alain J Brizard. Hamiltonian theory of guiding-center motion. *Reviews of modern physics*, 81(2):693–738, 2009.

[26] Eugenio Schuster. What is nuclear fusion? Plasma Control Laboratory, Lehigh University, 2022. URL `https://www6.lehigh.edu/~eus204/lab/PCL_fusion.php`. Accessed: 2026-01-10.

[27] AV Burdakov, AA Ivanov, and EP Kruglyakov. Modern magnetic mirrors and their fusion prospects. *Plasma Physics and Controlled Fusion*, 52(12):124026, 2010.

[28] Energy Encyclopedia. Magnetic mirror. `https://www.energyencyclopedia.com/en/glossary/magnetic-mirror`, . Accessed: 2026-01-11.

[29] Energy Encyclopedia. Magnetic field lines. `https://www.energyencyclopedia.com/en/free-downloads/images/magnetic-field-lines-186`, . Accessed: 2026-01-11.

[30] AD Sakharov and IE Tamm. Theory of magnetic thermonuclear reactor. *Physics of plasma and problem of controlled thermonuclear reactions*, 1:20–30, 1958.

[31] L Jr Spitzer. A proposed stellarator. Technical report, Princeton Univ., N.J. Forrestal Research Center, 07 1951.

[32] ITER Organization. Magnets. `https://www.iter.org/machine/magnets`, . Accessed: 2026-01-15.

[33] Lyman Spitzer Jr and Richard Härm. Transport phenomena in a completely ionized gas. *Physical Review*, 89(5):977, 1953.

[34] Peter C Stangeby. *The plasma boundary of magnetic fusion devices*. CRC Press, 2000.

[35] Jozef Ongena, Robert Koch, Robert Wolf, and Hartmut Zohm. Magnetic-confinement fusion. *Nature Physics*, 12(5):398–410, 2016.

[36] ITER Organization. Statement of the ITER organization. Statement at the 69th Regular Session of the IAEA General Conference (GC69), September 2025.

[37] Pietro Barabaschi, Arnaud Fossen, Alberto Loarte, Alain Becoulet, Laban Coblentz, and ITER Contributors. Iter progresses into new baseline. *Fusion Engineering and Design*, 215:114990, 2025.

[38] Alberto Loarte, RA Pitts, T Wauters, I Nunes, P de Vries, SH Kim, F Köchl, A Polevoi, M Lehnen, J Artola, et al. The new iter baseline, research plan and open r&d issues. *Plasma Physics and Controlled Fusion*, 67(6):065023, 2025.

[39] Kai Henrik Nordlund et al. European research roadmap to the realisation of fusion energy. 2018.

[40] Richard A Pitts, Xavier Bonnin, Frédéric Escourbiac, Heinke Frerichs, JP Gunn, Takeshi Hirai, AS Kukushkin, Elizaveta Kaveeva, MA Miller, David Moulton, et al. Physics basis for the first iter tungsten divertor. *Nuclear Materials and Energy*, 20: 100696, 2019.

[41] M Merola, W Dänner, M Pick, and The EU ITER Participating Team. Eu r&d on divertor components. *Fusion engineering and design*, 75:325–331, 2005.

[42] Russell H Jones, Howard L Heinisch, and KA McCarthy. Low activation materials. *Journal of nuclear materials*, 271:518–525, 1999.

[43] J Roth, A Kirschner, W Bohmeyer, S Brezinsek, A Cambe, E Casarotto, R Doerner, E Gauthier, G Federici, S Higashijima, et al. Flux dependence of carbon erosion and implication for iter. *Journal of nuclear materials*, 337:970–974, 2005.

[44] Yasunori Yamamura and Hiro Tawara. Energy dependence of ion-induced sputtering yields from monatomic solids at normal incidence. *Atomic data and nuclear data tables*, 62(2):149–253, 1996.

[45] H Lux, R Kemp, DJ Ward, and M Sertoli. Impurity radiation in demo systems modelling. *Fusion Engineering and Design*, 101:42–51, 2015.

[46] J Romazanov, D Borodin, A Kirschner, S Brezinsek, S Silburn, A Huber, V Huber, H Bufferand, M Firdaouss, D Brömmel, et al. First ero2. 0 modeling of be erosion and non-local transport in jet iter-like wall. *Physica scripta*, 2017(T170):014018, 2017.

[47] D Matveev, Christoph Baumann, Juri Romazanov, Sebastijan Brezinsek, S Ratynskaia, Ladislas Vignitchouk, Panagiotis Tolias, K Paschalidis, David Tskhakaya, Michael Komm, et al. An integral approach to plasma-wall interaction modelling for eu-demo. *Nuclear Fusion*, 64(10):106043, 2024.

[48] G Vieider, M Merola, JP Bonal, P Chappuis, D Duglué, R Duwe, F Escourbiac, M Febvre, L Giancarli, M Grattarola, et al. European development of the iter divertor target. *Fusion engineering and design*, 46(2-4):221–228, 1999.

[49] Richard A Pitts, S Carpentier, F Escourbiac, T Hirai, V Komarov, S Lisgo, AS Kukushkin, A Loarte, M Merola, A Sashala Naik, et al. A full tungsten divertor for iter: Physics issues and design status. *Journal of Nuclear Materials*, 438: S48–S56, 2013.

[50] Fusion for Energy (F4E). Iter divertor cassette bodies pass crucial leak tests, October 2025. URL `https://fusionforenergy.europa.eu/news/iter-cassette-bodies-hot-helium-leak-tests/`. Published October 14, 2025. Accessed January 21, 2026.

[51] GF Matthews, M Beurskens, S Brezinsek, M Groth, E Joffrin, A Loving, M Kear, ML Mayoral, R Neu, P Prior, et al. Jet iter-like wall—overview and experimental programme. *Physica Scripta*, 2011(T145):014001, 2011.

[52] Joelle Mailloux, N Abid, K Abraham, Paulo Abreu, O Adabonyan, P Adrich, V Afanasev, M Afzal, T Ahlgren, Leena Aho-Mantila, et al. Overview of jet results for optimising iter operation. *Nuclear Fusion*, 62(4):042026, 2022.

[53] Jérôme Paméla, Guy F Matthews, Volker Philipps, Richard Kamendje, JET-EFDA Contributors, et al. An iter-like wall for jet. *Journal of nuclear materials*, 363:1–11, 2007.

[54] RA Pitts, A Loarte, T Wauters, M Dubrov, Y Gribov, F Köchl, A Pshenov, Y Zhang, J Artola, X Bonnin, et al. Plasma-wall interaction impact of the iter re-baseline. *Nuclear Materials and Energy*, 42:101854, 2025.

[55] ITER Organization. Blanket. ITER Organization website, The Machine, . URL `https://www.iter.org/machine/blanket`. Accessed 2026-01-23.

[56] Jörg Winter. Wall conditioning in fusion devices and its influence on plasma performance. *Plasma Physics and Controlled Fusion*, 38(9):1503, 1996.

[57] T Wauters, GJM Hagelaar, and RA Pitts. Modeling input to the iter glow discharge boronization system design. *Nuclear Materials and Energy*, 42:101891, 2025.

[58] K Schmid and T Wauters. Full w iter: assessment of expected w erosion and implications of boronization on fuel retention. *Nuclear Materials and Energy*, 41: 101789, 2024.

[59] Diagnostics. ITER Organization website. URL `https://www.iter.org/machine/supporting-systems/diagnostics`. Accessed: 2026-01-25.

[60] Krista Dulon. One step back from the heat. ITER Organization website, May 2012. URL `https://www.iter.org/node/20687/one-step-back-heat`. Accessed: 2026-01-25.

[61] M. Walsh, P. Andrew, and R. Barnsley, et al. Iter diagnostic challenges. In *2011 IEEE/NPSS 24th Symposium on Fusion Engineering*, pages 1–8, 2011. doi: 10.1109/SOFE.2011.6052210.

[62] Philippe Mertens, Romain Boman, Sven Dickheuer, Yury Krasikov, Andreas Krimmer, Dieter Leichtle, Kim Liegeois, Christian Linsmeier, Andrey Litnovsky, Oleksander Marchuk, et al. On the use of rhodium mirrors for optical diagnostics in iter. *Fusion engineering and design*, 146:2514–2518, 2019.

[63] Artem M Dmitriev, Youpeng Wang, Tomás C Sousa, Laurent Marot, Lucas Moser, and Ernst Meyer. Platinum as a first mirror material for fusion applications: a comparison with rhodium. *Nuclear Fusion*, 65(3):036012, 2025.

[64] Harold Earl Bennett and JO119764 Porteus. Relation between surface roughness and specular reflectance at normal incidence. *Journal of the optical society of America*, 51(2):123–129, 1961.

[65] Kunal Soni, Lucas Moser, Roland Steiner, Daniel Mathys, Frederic Le Guern, Juan Piqueras, Laurent Marot, and Ernst Meyer. Plasma cleaning of steam ingressed iter first mirrors. *Nuclear Materials and Energy*, 21:100702, 2019.

[66] A Litnovsky, VS Voitsenya, R Reichle, M Walsh, A Razdobarin, A Dmitriev, N Babinov, L Marot, L Moser, R Yan, et al. Diagnostic mirrors for iter: research in the frame of international tokamak physics activity. *Nuclear Fusion*, 59(6):066029, 2019.

[67] E León-Gutierrez, R Lopez Heredero, C Rodriguez, MC Torquemada, R García-López, JM Fernandez Marin, CL Barber Daza, C Pastor, M Medrano, R Vila, et al. Optical characterization of a full scale rhodium coated first mirror for iter wide angle viewing system (wavs) diagnostic. *Fusion Engineering and Design*, 222: 115463, 2026.

[68] M Rubel, G De Temmerman, Per Sundelin, JP Coad, A Widdowson, D Hole, F Le Guern, M Stamp, J Vince, JET-EFDA Contributors, et al. An overview of a comprehensive first mirror test for iter at jet. *Journal of Nuclear Materials*, 390:1066–1069, 2009.

[69] Marek Rubel, Darya Ivanova, JP Coad, G De Temmerman, J Likonen, L Marot, A Schmidt, A Widdowson, JET-EFDA contributors, et al. Overview of the second stage in the comprehensive mirrors test in jet. *Physica Scripta*, 2011(T145):014070, 2011.

[70] Alvaro Garcia-Carrasco, Per Petersson, Marek Rubel, A Widdowson, E Fortuna-Zalesna, S Jachmich, M Brix, L Marot, and JET Contributors. Plasma impact on diagnostic mirrors in jet. *Nuclear Materials and Energy*, 12:506–512, 2017.

[71] Sunwoo Moon, Per Petersson, Marek Rubel, E Fortuna-Zalesna, A Widdowson, S Jachmich, A Litnovsky, E Alves, and JET Contributors. First mirror test in jet for iter: Complete overview after three ilw campaigns. *Nuclear Materials and Energy*, 19:59–66, 2019.

[72] Marek Rubel, Sunwoo Moon, Per Petersson, A Widdowson, RA Pitts, S Aleiferis, Elżbieta Fortuna-Zaleśna, G De Temmerman, and R Reichle. First mirror erosion–deposition studies in jet using an iter-like mirror test assembly. *Nuclear Fusion*, 61 (4):046022, 2021.

[73] Laura Dittrich, Per Petersson, Hafssa Laabadi, Eduardo Pitthan, Marek Rubel, A Widdowson, Agnieszka Krawczyńska, Karol Szlązak, et al. Impact of ion irradiation and film deposition on optical and fuel retention properties of mo polycrystalline and single crystal mirrors. *Nuclear Materials and Energy*, 37:101548, 2023.

[74] L Moser, L Marot, R Steiner, R Reichle, F Leipold, C Vorpahl, F Le Guern, U Walach, S Alberti, I Furno, et al. Plasma cleaning of iter first mirrors. *Physica Scripta*, 2017(T170):014047, 2017.

[75] L Moser, L Marot, R Steiner, M Newman, A Widdowson, Darya Ivanova, Jari Likonen, Per Petersson, G Pintsuk, Marek Rubel, et al. Plasma cleaning of beryllium coated mirrors. *Physica Scripta*, 2016(T167):014069, 2016.

[76] Alessandro Maffini, L Moser, L Marot, R Steiner, David Dellasega, A Uccello, E Meyer, and Matteo Passoni. In situ cleaning of diagnostic first mirrors: an experimental comparison between plasma and laser cleaning in iter-relevant conditions. *Nuclear Fusion*, 57(4):046014, 2017.

[77] Zhihu Zhou, Weipeng Sun, Jiajun Wu, Hongwei Chen, Fei Zhang, and Shuangxi Wang. The fundamental mechanisms of laser cleaning technology and its typical applications in industry. *Processes*, 11(5):1445, 2023.

[78] Costas Fotakis, Demetrios Anglos, Vassilis Zafiropulos, Savas Georgiou, and Vivi

Tornari. *Lasers in the preservation of cultural heritage: principles and applications*. CRC Press, 2006.

[79] Sergey I Kudryashov, Susan D Allen, and Shishir D Shukla. Experimental and theoretical studies of laser cleaning mechanisms for submicrometer particulates on si surfaces. *Particulate science and technology*, 24(3):281–299, 2006.

[80] Anne-Maria Reinecke, Margret Acker, Steffen Taut, Marion Herrmann, Wolfgang Lippmann, and Antonio Hurtado. Laser beam decontamination of metallic surfaces with a pulsed (150 w) nd: Yag laser. *Nuclear Engineering and Technology*, 55(11): 4159–4166, 2023.

[81] Guodong Zhu, Zhenhai Xu, Yang Jin, Xi Chen, Lijun Yang, Jie Xu, Debin Shan, Yanbin Chen, and Bin Guo. Mechanism and application of laser cleaning: A review. *Optics and Lasers in Engineering*, 157:107130, 2022.

[82] A Widdowson, JP Coad, G De Temmerman, D Farcage, D Hole, Darya Ivanova, A Leontyev, M Rubel, A Semerok, A Schmidt, et al. Removal of beryllium-containing films deposited in jet from mirror surfaces by laser cleaning. *Journal of Nuclear Materials*, 415(1):S1199–S1202, 2011.

[83] Alessandro Maffini, A Uccello, David Dellasega, Valeria Russo, Stefano Perissinotto, and Matteo Passoni. Laser cleaning of diagnostic mirrors from tokamak-like carbon contaminants. *Journal of Nuclear Materials*, 463:944–947, 2015.

[84] Alessandro Maffini, A Uccello, David Dellasega, and Matteo Passoni. Laser cleaning of diagnostic mirrors from tungsten–oxygen tokamak-like contaminants. *Nuclear Fusion*, 56(8):086008, 2016.

[85] Adawiya J Haider, Taif Alawsi, Mohammed J Haider, Bakr Ahmed Taha, and Haydar Abdulameer Marhoon. A comprehensive review on pulsed laser deposition technique to effective nanostructure production: Trends and challenges. *Optical and Quantum Electronics*, 54(8):488, 2022.

[86] Angela De Bonis and Roberto Teghil. Ultra-short pulsed laser deposition of oxides, borides and carbides of transition elements. *Coatings*, 10(5):501, 2020.

[87] T Ohnishi, H Koinuma, and M Lippmaa. Pulsed laser deposition of oxide thin films. *Applied surface science*, 252(7):2466–2471, 2006.

[88] Andrey V Gusarov and Igor Smurov. Thermal model of nanosecond pulsed laser ablation: Analysis of energy and mass transfer. *Journal of applied physics*, 97(1), 2005.

[89] Davide Orecchia, Alessandro Maffini, Margherita Zavelani-Rossi, and Matteo Passoni. Versatile synthesis of nanofoams through femtosecond pulsed laser deposition. *Small Structures*, 5(6):2300560, 2024.

[90] Rajiv K Singh. Spatial thickness variations in laser-deposited thin films. *Materials Science and Engineering: B*, 45(1-3):180–185, 1997.

[91] Weilie Zhou, Robert Apkarian, Zhong Lin Wang, and David Joy. Fundamentals of scanning electron microscopy (sem). In *Scanning microscopy for nanotechnology: techniques and applications*, pages 1–40. Springer, 2006.

[92] Nanoscience Instruments. Scanning electron microscopy. Nanoscience Instruments website. URL `https://www.nanoscience.com/techniques/scanning-electron-microscopy/`.

[93] Daisuke Shindo and Tetsuo Oikawa. Energy dispersive x-ray spectroscopy. In *Analytical electron microscopy for materials science*, pages 81–102. Springer, 2002.

[94] Andrea Pazzaglia, Alessandro Maffini, David Dellasega, Alessio Lamperti, and Matteo Passoni. Reference-free evaluation of thin films mass thickness and composition through energy dispersive x-ray spectroscopy. *Materials Characterization*, 153:92–102, 2019.

[95] Max Born and Emil Wolf. *Principles of optics: electromagnetic theory of propagation, interference and diffraction of light*. Elsevier, 2013.

[96] PerkinElmer Inc. High-performance lambda spectrometers: Hardware guide, December 2007.

[97] EAG Laboratories. Ultraviolet/visible/near infrared spectroscopy (uv/vis/nir). `https://www.eag.com/techniques/spectroscopy/uv-vis-spectroscopy/`. Accessed: 2026-02-05.

[98] Matteo Passoni, David Dellasega, G Grosso, C Conti, MC Ubaldi, and CARLO ENRICO Bottani. Nanostructured rhodium films produced by pulsed laser deposition for nuclear fusion applications. *Journal of nuclear materials*, 404(1):1–5, 2010.

[99] Andrea Uccello, David Dellasega, S Perissinotto, NORA Lecis, and Matteo Passoni. Nanostructured rhodium films for advanced mirrors produced by pulsed laser deposition. *Journal of nuclear materials*, 432(1-3):261–265, 2013.

[100] Andrea Uccello, Alessandro Maffini, David Dellasega, and Matteo Passoni. Laser

cleaning of pulsed laser deposited rhodium films for fusion diagnostic mirrors. *Fusion Engineering and Design*, 88(6-8):1347–1351, 2013.

[101] D. W. Lynch and W. R. Hunter. Rhodium (Rh). In Edward D. Palik, editor, *Handbook of Optical Constants of Solids*, volume 1, pages 341–349. Academic Press, San Diego, 1985.

[102] David Dellasega, Valeria Russo, Andrea Pezzoli, Claudia Conti, Nora Lecis, Edoardo Besozzi, Marco Beghi, Carlo E Bottani, and Matteo Passoni. Boron films produced by high energy pulsed laser deposition. *Materials & Design*, 134:35–43, 2017.

[103] D Mazzucconi, D Vavassori, D Dellasega, FM Airaghi, S Agosteo, M Passoni, A Pola, and D Bortot. Proton boron fusion reaction: A novel experimental strategy for cross section investigation. *Radiation Physics and Chemistry*, 204:110727, 2023.

[104] Alessandro Maffini, Davide Orecchia, Andrea Pazzaglia, Margherita Zavelani-Rossi, and Matteo Passoni. Pulsed laser deposition of carbon nanofoam. *Applied Surface Science*, 599:153859, 2022.

[105] Xiangdong Ma, WN Unertl, and A Erdemir. The boron oxide–boric acid system: Nanoscale mechanical and wear properties. *Journal of materials research*, 14(8): 3455–3466, 1999.

[106] Holger von Wenckstern, Max Kneiß, Anna Hassa, Philipp Storm, Daniel Splith, and Marius Grundmann. A review of the segmented-target approach to combinatorial material synthesis by pulsed-laser deposition. *physica status solidi (b)*, 257(7): 1900626, 2020.

[107] Tomasz Moscicki. Differences in nanosecond laser ablation and deposition of tungsten, boron, and wb2/b composite due to optical properties. *International Journal of Optics*, 2016(1):5438721, 2016.

[108] Jean M Bennett. Comparison of techniques for measuring the roughness of optical surfaces. *Optical Engineering*, 24(3):380–387, 1985.

[109] M Wisse, L Marot, A Widdowson, Marek Rubel, Darya Ivanova, Per Petersson, RP Doerner, MJ Baldwin, Jari Likonen, E Alves, et al. Laser-assisted cleaning of beryllium-containing mirror samples from jet and pisces-b. *Fusion engineering and design*, 89(2):122–130, 2014.

A | Appendix A: Calculation of Surface Roughness

This appendix details the method implemented for obtaining the mean surface roughness of the samples produced and cleaned in this thesis and presented in Chapters 5 and 6, starting from the reflectance measurements retrieved via spectrophotometry.

The morphological quality of the films was evaluated optically by analyzing the scattered light in the form of diffuse reflectance. The quantitative parameter extracted is the root mean square roughness (R_{rms}) calculated using the Bennett model and employing the Total Integrated Scattering (TIS) method.

The Total Integrated Scattering (TIS) factor is defined as the ratio between the diffuse reflectance (R_{diff}) and the total reflectance (R_{tot}) measured by the spectrophotometer:

$$\mathrm{TIS} = \frac{R_{\mathrm{diff}}}{R_{\mathrm{tot}}} \tag{A.1}$$

According to the Bennett's relation [64], the specular reflectance (R_{spec}) decays exponentially with increasing roughness:

$$R_{\mathrm{spec}} = R_0 \exp\left[-\left(\frac{4\pi R_{\mathrm{rms}}}{\lambda}\right)^2\right] \tag{A.2}$$

where R_0 is the reflectivity of the same material with an ideally smooth surface. Moreover, normal incidence of light is assumed, which is consistent with the measurement conditions.

In this experimental analysis, R_0 is approximated by the total reflectance (R_{tot}) measured using the integrating sphere. This approximation is justified by the fact that surface roughness is assumed to redistribute the reflected light from the specular direction to random scattered directions (diffuse component), without modifying the intrinsic absorption coefficient of the material. Under this assumption, the total reflectance measured by the

integrating sphere provides the most accurate experimental estimate of R_0:

$$R_0 \approx R_{\text{spec}} + R_{\text{diff}} = R_{\text{tot}} \tag{A.3}$$

Assuming that the roughness is much smaller than the wavelength ($R_{\text{rms}} \ll \lambda$), a first-order Taylor expansion ($e^{-x} \approx 1 - x$) can be applied to the Bennett's formula:

$$\frac{R_{\text{spec}}}{R_{\text{tot}}} = \frac{R_{\text{tot}} - R_{\text{diff}}}{R_{\text{tot}}} = 1 - \text{TIS} = 1 - \left(\frac{4\pi R_{\text{rms}}}{\lambda}\right)^2 \tag{A.4}$$

Thus, the analytical formula used for the calculation of the surface roughness is:

$$\text{TIS} = \left(\frac{4\pi R_{\text{rms}}}{\lambda}\right)^2 \Longrightarrow R_{\text{rms}} = \frac{\lambda}{4\pi}\sqrt{\frac{R_{\text{diff}}}{R_{\text{tot}}}} \tag{A.5}$$

The obtained surface roughness values were considered reliable only if the result was approximately constant over a spectral region. Indeed, the spectral region yielding a constant roughness value is the one where the fit with the exponential function described by Bennett's formula is optimal, indicating that in that region, surface roughness is the factor effectively determining light scattering.

List of Figures

List of Tables

Ringraziamenti

Desidero ringraziare tutto il NanoLab per avermi accolta tra i suoi nomadi, sono stati mesi intensi e molto ricchi, che conserverò con affetto.

Ringrazio in particolar modo Davide Orecchia, che mi ha seguita in questi mesi di laboratorio e i cui insegnamenti e suggerimenti sono stati di fondamentale importanza per la realizzazione di questo lavoro. Ringrazio inoltre il mio relatore Alessandro Maffini, per l'immancabile supporto che mi ha fornito in questi mesi, e per avermi insegnato molto. *Il demone dell'ottimizzazione non sempre porta a cose belle*, me ne ricorderò.